




EX LIBRIS
UNIVERSITATIS
ALBERTÆNSIS



Digitized by the Internet Archive
in 2025 with funding from
University of Alberta Library

<https://archive.org/details/0162007815812>

Do not use this thesis as an example of format.

University of Alberta

Library Release Form

Name of Author: James Harry John Buchholz

Title of Thesis: The Vortex Ring Structure Created by a Bursting Bubble

Degree: Master of Science

Year this Degree Granted: 1997

Permission is hereby granted to the University of Alberta to reproduce single copies of this thesis and to lend or sell such copies for private, scholarly, or scientific research purposes only.

The author reserves all other publication and other rights in association with the copyright in the thesis, and except as hereinbefore provided, neither the thesis nor any substantial portion thereof may be printed or otherwise reproduced in any material form whatever without the author's prior written permission.

University of Alberta

The Vortex Ring Structure Created by a Bursting Bubble

by



James Harry John Buchholz

A thesis submitted to the Faculty of Graduate Studies and Research in
partial fulfillment of the requirements for the degree of Master of Science.

Department of Mechanical Engineering

Edmonton, Alberta

Fall 1997

University of Alberta

Faculty of Graduate Studies and Research

The undersigned certify that they have read, and recommend to the Faculty of Graduate Studies and Research for acceptance, a thesis entitled The Vortex Ring Structure Created by a Bursting Bubble submitted by James Harry John Buchholz in partial fulfillment of the requirements for the degree of Master of Science .

ABSTRACT

For the first time, the structure of the vortex ring created by a bursting bubble has been photographically studied. A skeleton vortex model of the evolving structure has been constructed. Two upward-moving vortex rings with collinear axes are formed shortly after bubble rupture. The two rings leapfrog and then form a structure consisting of a vortex ring which sheds *lobes* of fluid which are sometimes similar in appearance to hairpin vortex loops. A two-dimensional point vortex computational model was created which produced images with close resemblance to the physical structure. The kinematics of the bubble film were also studied. To enable this investigation, a novel apparatus was constructed. The floating bubble is centred on a pool of liquid atop a vertical cylinder using a technique discovered here. A method was devised for measuring the pressure inside the bubble, and this pressure along with the bubble radius of curvature have been used to determine bubble surface tension.

ACKNOWLEDGEMENTS

My sincere thanks are extended to my advisor Dr. L.W. Sigurdson for his patience and much appreciated effort in the many hours spent teaching me and guiding me through the difficulties of this work, and for providing me with the opportunity to explore this phenomenon, and present it.

I am also very grateful to Mr. Bill Peck for sharing his knowledge on vorticity generation and kinematics among numerous other subjects, and for his valuable help and advice in beginning this study. Bill also developed the \LaTeX format files for this thesis.

Mr. Bernie Faulkner and Mr. Terry Nord are thanked for their valiant, and ultimately victorious battle with the electronics. My thanks also goes to Mr. Andrew Coward for his work in designing and constructing a brilliantly simple controller for the piston pump. The rest of the crew in the machine shop and technicians' shop, and the department office are also thanked for their excellent work.

Faculty and students in the department have also assisted me in their areas of expertise. Dr. Donqing Li and Mr. Chun Yang are thanked for their advice on surface tension, and the use of and assistance with Dr. Li's apparatus. I am also appreciative of the guidance of Dr. Kevin Stapleton and Ms. Helena Orszanska in the subjects of aerosols and surfactants, respectively.

Thanks also to my defence committee, Dr. A.W. Lipsett, Dr. N. Rajaratnam, and Dr. R. Toogood, for their clever insight, and helpful critique.

I am grateful to my family for encouraging me, helping me, and putting up with me during the difficult times during my study. I also thank all those who encouraged me, particularly toward the end.

Financial support from the Natural Sciences and Engineering Research Council and the University of Alberta is also very much appreciated.

CONTENTS

1	Introduction	1
1.1	Motivation	1
1.2	Objectives	3
1.3	Previous Work	5
1.4	Thesis Outline	6
2	Experimental Apparatus and Procedures	12
2.1	Introduction	12
2.2	Apparatus	13
2.2.1	Development	14
2.2.2	Current Apparatus	17
2.3	Results	33
2.4	Conclusions	33
3	Results and Discussion	38
3.1	Introduction	38
3.2	Apparatus	39
3.3	Experimental Results and Discussion	39
3.3.1	The Bubble	39
3.3.2	The Vortex Structure	58
3.3.3	Passive Bursting	93
3.4	The Computational Model	94
3.5	Computed Results and Discussion	98
3.5.1	Evolution of the Uniform Circulation Model	98
3.5.2	Evolution of the Varying Circulation Model	106
3.5.3	Discussion of Computed Results	107
3.6	Conclusions	109

4	Conclusions and Recommendations	114
4.1	Conclusions	114
4.2	Recommendations for Future Work	115
A	Dr. Ashurst's Code	118
A.1	The Initial Geometric Conditions	119
A.2	Vortex Core Model and Induced Velocity	119
A.3	The Numerical Scheme	120
B	Canadian Congress of Applied Mechanics	122
C	International Symposium on Flow Visualization	125
D	American Physical Society	132
E	Physics of Fluids: Gallery of Fluid Motion	134

LIST OF FIGURES

1.1	A falling drop and a rising bubble	4
2.1	The Original Teflon Cylinder	15
2.2	Plan View of the Preliminary Experiment	15
2.3	The Modified Teflon Cylinder	19
2.4	The Piston Pump	19
2.5	The Electronics	22
2.6	Aerosol and Liquid Transport System	25
2.7	Photographic Data	34
3.1	Spherical Region of Bubble	41
3.2	The Large Bubble Bursting	44
3.2	The Large Bubble Bursting (cont.)	45
3.3	The Small Bubble Bursting	46
3.3	The Small Bubble Bursting (cont.)	47
3.4	Averages of Left and Right Side Film Rim Displacements	50
3.5	Early Averaged Film Rim Displacements	52
3.6	Film Retraction Plots Superimposed	53
3.7	Separation of Left and Right Film Rim Displacements	55
3.8	Double Exposure Photographs of the Bursting Bubble (600 μs to 800 μs)	56
3.9	The Evolution of the Vortex Structure Emerging from the Large Bubble	60
3.9	The Evolution of the Vortex Structure Emerging from the Large Bubble (cont.)	61
3.9	The Evolution of the Vortex Structure Emerging from the Large Bubble (cont.)	62
3.9	The Evolution of the Vortex Structure Emerging from the Large Bubble (cont.)	63

3.10 The Evolution of the Vortex Structure Emerging from the Small Bubble	64
3.10 The Evolution of the Vortex Structure Emerging from the Small Bubble (cont.)	65
3.10 The Evolution of the Vortex Structure Emerging from the Small Bubble (cont.)	66
3.10 The Evolution of the Vortex Structure Emerging from the Small Bubble (cont.)	67
3.11 Vortex Evolution Model (early development)	68
3.11 Vortex Evolution Model (early development cont.)	69
3.12 Possible Lobe Generation Model (case 1, vortex A forms lobes)	70
3.12 Possible Lobe Generation Model (case 1, vortex A forms lobes, cont.)	71
3.13 Possible Lobe Generation Model (case 2, vortex B forms lobes)	72
3.13 Possible Lobe Generation Model (case 2, vortex B forms lobes, cont.)	73
3.14 Vortex ring leading edge displacement.	84
3.15 Triple Exposure Photographs of the Vortex Ring (large bubble)	86
3.16 Preliminary Photographic Data with Smoke Tracer.	89
3.16 Preliminary Photographic Data with Smoke Tracer (cont.). . .	90
3.17 Initial Conditions of the Computational Model.	96
3.18 Legend for Figures 3.19 and 3.20.	99
3.19 Computed Results with Point Vortices of Uniform Circulation	100
3.19 Computed Results with Point Vortices of Uniform Circulation (cont.)	101
3.20 Computed Results with Point Vortices of Varying Circulation	102
3.20 Computed Results with Point Vortices of Varying Circulation (cont.)	103

LIST OF TABLES

2.1	Bubble Shrinkage Caused by Pressure Measurement	28
2.2	Calculated Surface Tensions	33
3.1	Bubble Properties	42
3.2	Linearized Film Retraction Velocities and Intercepts	50
3.3	Linearized Film Retraction Velocities and Intercepts (early retraction)	51
3.4	Film Retraction Velocities Derived from Double Exposure Photographs (large bubbles)	57
3.5	Film Retraction Velocities Derived from Double Exposure Photographs (small bubbles)	57
3.6	Vortex Ring Leading Edge Velocities Derived from Triple Exposure Photographs (large bubbles)	85
3.7	Vortex Ring Leading Edge Velocities Derived from Triple Exposure Photographs (small bubbles)	87

NOMENCLATURE

LATIN SYMBOLS

h	film thickness
ΔP_b	bubble gauge pressure
R	bubble radius of curvature
R_c	initial radius of curvature of computational vortex sheet
Re_D	vortex ring Reynolds num- ber based on core diameter
t	time after initiation of spark
dt	time step in computational model
T	ambient temperature
U_a	aerosol leading edge veloc- ity
U_f	film rim velocity

GREEK SYMBOLS

δ	initial separation of point vortices in computational model
----------------	---

Δ	film rim displacement
γ	surface tension at film air/water interface
Γ	vortex circulation
ρ	film mass density
σ	film surface tension (sum of both interfaces)

CHAPTER 1

INTRODUCTION

1.1 Motivation

In many turbulent flows, it is now known that there is some identifiable, or coherent vortical structure present. This has led many researchers to look at these flows, not with time-averaged measurements, but through visualization of the flow at consecutive instants of the fluid motion. A turbulent flow can be idealized as a system of vortices which convect and deform according to the laws of vortex dynamics. The development of these vortex models of turbulent flows allows certain problems to be solved in a more physical manner than previous turbulence models permitted. A review of some computational vortex models is presented in (9). Saffman (19) emphasizes this marriage of turbulence and vortex dynamics:

It can be claimed that the problems of turbulence and transition are problems of the mechanics of vorticity, which is the fundamental dynamical quantity and constitutes the “sinews and muscles

of fluid motion.” One of the best definitions of turbulence is that it is a field of random or chaotic vorticity.

Among those flows in which coherent structure has been identified is the classic plane turbulent mixing layer, in which Brown and Roshko (2) discovered that the growth mechanism is actually through the existence and pairing of coherent vortices. Ashurst and Meiburg (1) have since developed a three-dimensional computational vortex model of this phenomenon. Sigurdson (23) has applied acoustic forcing to the separation bubble formed on a cylinder aligned axially with the flow direction, and achieved a reduction in the drag coefficient. Coles (5) has compiled a paper outlining other coherent structures which he regards as valuable for studying and modelling turbulence. These include the turbulent puff in a pipe, the turbulent spot in a laminar boundary layer, the turbulent vortex ring, which was the subject of another paper (8), and other flows.

The present work has been directly motivated by research conducted by Peck and Sigurdson (15) on vortex rings formed by drops of dyed water which impact the free surface of a pool of water at a specific Weber and Froude Number. It has been noted by Sigurdson (21) that the three-dimensional vortex structure generated bears a striking resemblance to the mushroom cloud formed by an above-ground nuclear test. Their work involved modelling the evolution of the drop-formed structure, and the mechanism and equations of vorticity generation at the air-water interface in this experiment.

Figure 1.1 shows a schematic of a falling drop impinging on the surface of a pool of water on the left side, and a rising bubble penetrating the surface on the right side. Comparison of these two events would suggest that they are very similar in that their geometries closely resemble each other. On the other hand, on crossing the boundary between the drop and the surrounding air, one would measure the opposite density gradient as that which exists when crossing the interface from the gaseous bubble into the surrounding liquid. This similarity and difference has caused us to raise the question of whether a vortex ring is formed in the air above a bursting bubble as it is beneath the liquid surface in the case of an impacting drop. If so, how do the structures compare? Is the mechanism of vorticity generation the same in the two cases? Any vorticity generation equations must explain the results.

A survey of the literature and our preliminary experiments showed that a vortex ring is formed by a bursting bubble. The literature suggested that no previous photographs of the vortex ring had been taken. The current study was conducted to examine in detail the evolution, properties, and creation of this structure.

1.2 Objectives

The objectives of this study are threefold. Firstly, the vortex dynamics specifically of a bursting bubble are of fundamental interest. MacIntyre (10) states that bursting ocean bubbles form the primary agent of mass transfer from sea to air. The vortex ring created is one of the media by which these particles

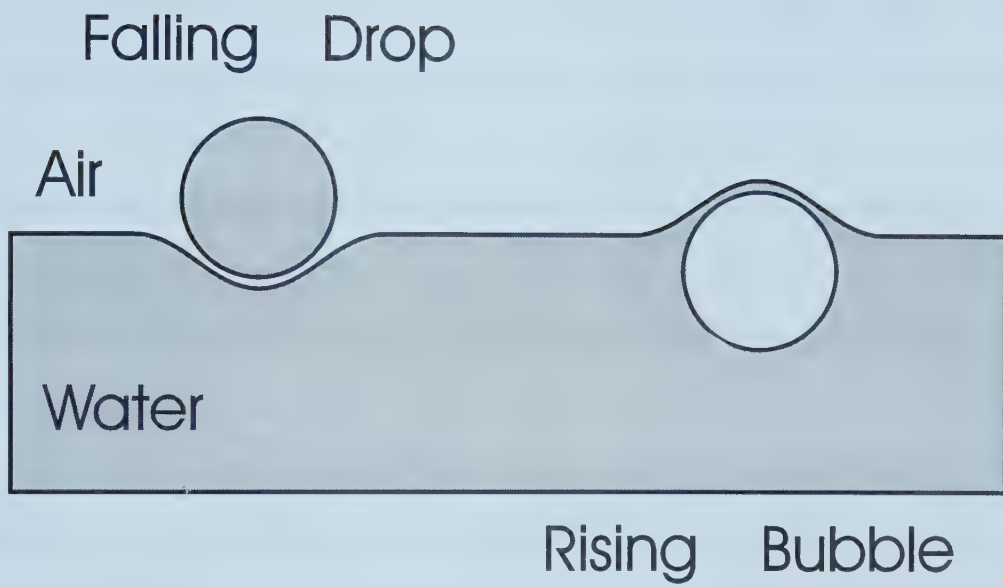


Figure 1.1: A Falling Drop and a Rising Bubble

are carried into the atmosphere. It is also suggested that in boiling processes conducted under certain conditions, such as in micro-gravity, vortex rings emerging from the bursting bubbles would form the primary mode of heat transfer from the liquid since buoyant thermals would not be created.

Secondly, the mechanism of vorticity generation is of interest. Any insight into how the vorticity is created by the bursting bubble may be used to broaden the understanding already developed (16) through investigation of the impacting drop and other ongoing world-wide projects.

Finally, and most importantly, this research will broaden the current understanding of coherent structure in turbulence. It is apparent, from considering the structures formed by the drop, the bomb, and the bubble, that similarities in structure may exist between flows of vastly different scale and buoyancy effects.

1.3 Previous Work

Vortex rings, bubbles, and liquid films have been the subject of numerous studies. Others have previously noted that a vortex ring is generated by a bursting bubble. Rogers (18) first published sketches of the vortex rings in 1858, and Campbell Swinton and Beale (24) witnessed vortex rings produced by smoke-filled bubbles in oil. Day (7) inferred the existence of a vortex ring by the pattern formed by drops shed from the bursting bubble. However, the structure and evolution of the vortex ring have never been studied and modelled before.

Countless publications have been published on the subject of vortex rings formed in various ways. For example, it has even been suggested that atoms may be modelled as vortex rings (26). Maxworthy has reported observations of his experimental studies of vortex rings in the 1970's ((10), (11), (12)). In addition, vortex rings formed by impacting water drops (15), and water drops just coalescing with a fluid (20) have been reported, to name a few.

A bursting bubble may be considered a special (spherical) case of a retracting film. Retracting liquid films have also been quite rigorously studied in the literature, and are of interest in this experiment because the retracting bubble film is expected to play an important role in the generation of vorticity in the current experiment. Ranz (17) experimentally measured the retraction velocity and estimated the thickness of a planar bursting film. Taylor (25) developed a theory which predicted whether a hole in a film would result in rupture or if it would close, based on the size of the hole and thickness of the film. McEntee and Mysels (13) have conducted extensive experiments on the structure and velocity of bursting films, and Mysels and Stikeleather (14) have compared spark-burst and passively-burst films, reporting no significant differences in their behaviours. Culick (6) has developed a model to calculate the velocity with which the edge of a horizontal film retracts.

1.4 Thesis Outline

This thesis is written in paper format, with a bibliography at the end of each chapter. Chapter 1 contains an introduction to the problem being studied

along with a brief review of the literature. Chapter 2 is mainly concerned with the development and current state of the apparatus. A novel method of positioning the bubble will be presented, as well as procedures developed for measuring bubble pressure and surface tension. Figures 2.1 and 2.2 have appeared in (3).

Chapter 3 discusses the results obtained. Section 3.3.1 presents properties of the bubble, and the kinematics of the retracting bubble film. Section 3.3.2 discusses the vortex structure created by the bursting bubble, beginning with a model describing the evolution of the structure. Some kinematic properties of the vortex rings are also reported. In sections 3.4 and 3.5, a simple two-dimensional computational vortex model is used to simulate the event, and some suggestions are made concerning questions which remain about the experimental vortex model. Finally, Section 3.6 summarizes the conclusions of Chapter 3. Figures 3.16(a) and 3.16(c) have appeared in (22). Figure 3.16(d) has appeared in (4), and Figures 3.16(e) and 3.16(f) have appeared in (3).

Chapter 4 summarizes and synthesizes the work of this thesis and presents conclusions and recommendations for further work.

There are also five Appendices, A to E. Appendix A describes the computational model of Section 3.4 in greater detail. Appendices B to E contain previous publications resulting from some of our earlier work.

Bibliography

- [1] W. T. Ashurst and Eckart Meiburg. Three-dimensional shear layers via vortex dynamics. *J. Fluid Mech.*, 189:87–116, 1988.
- [2] Garry L. Brown and Anatol Roshko. On density effects and large structure in turbulent mixing layers. *J. Fluid Mech.*, 64:775–816, 1974.
- [3] James Buchholz, Lorenz Sigurdson, and Bill Peck. An apparatus to study vortex rings emerging from bursting air bubbles. In J. Crowder, editor, *Proceedings of the Seventh International Symposium on Flow Visualization.*, pages 146–151, New York, 1995. Begell House Inc.
- [4] James Buchholz, Lorenz Sigurdson, and Bill Peck. Bursting soap bubble. In Gallery of Fluid Motion, Helen Reed, editor. *Phys. Fluids*, 7(9):s3, September 1995.
- [5] Donald Coles. Prospects for useful research on coherent structure in turbulent shear flow. *Proc. Indian Acad. Sci.*, 4:111–127, 1981.
- [6] F. E. C. Culick. Comments on a ruptured soap film. *J. Appl. Phys.*, 31(6):1128–1129, 1960.
- [7] J. A. Day. Production of droplets and salt nuclei by the bursting of air-bubble films. 90:72–78, 1964.
- [8] A. Glezer and D. Coles. An experimental of a turbulent vortex ring. *J. Fluid Mech.*, 211:243–283, 1990.

- [9] A. Leonard. Vortex models for flow simulation. *J. Comput. Phys.*, 37(3), 1980.
- [10] T. Maxworthy. The structure and stability of vortex rings. *J. Fluid Mech.*, 51(part 1):15–32, 1972.
- [11] T. Maxworthy. Turbulent vortex rings. *J. Fluid Mech.*, 64(part 2):227–239, 1974.
- [12] T. Maxworthy. Some experimental studies of vortex rings. *J. Fluid Mech.*, 81:465–495, 1977.
- [13] Winnie R. McEntee and Karol J. Mysels. The bursting of soap films. 1. an experimental study. *J. Phys. Chem.*, 73(9):3018–3028, September 1969.
- [14] Karol J. Mysels and Jimmy A. Stikeleather. The bursting of soap films III. spontaneous and induced bursting. *J. Colloid Interface Sci.*, 35(1):159–162, January 1971.
- [15] Bill Peck and Lorenz Sigurdson. The three-dimensional vortex structure of an impacting water drop. *Phys. Fluids*, 6(2):564–576, February 1994.
- [16] Bill Peck and Lorenz Sigurdson. The creation of vorticity at fluid interfaces. In *Proceedings of the American Physical Society*. American Physical Society, 1996.

- [17] W. E. Ranz. Some experiments on the dynamics of liquid films. *J. Appl. Phys.*, 30(12):1950–1955, December 1959.
- [18] W.B. Rogers. On the formation of rotating rings by air and liquids under certain conditions of discharge. *Am. J. Sci. Arts. Sec. Ser.* , 26:246–258, 1858.
- [19] P. G. Saffman. Vortex interactions and coherent structures in turbulence. In *Proc. Symp. on Transition and Turbulence*, pages 149–166. Academic Press, 1980.
- [20] P. N. Shankar and Manoj Kumar. Vortex rings generated by drops just coalescing with a pool. *Phys. Fluids*, 7(4):737–746, April 1995.
- [21] Lorenz Sigurdson. Atom bomb/water drop. In Gallery of Fluid Motion, Helen Reed, editor. *Phys. Fluids A*, 3:2034, September 1987.
- [22] Lorenz W. Sigurdson, James H. Buchholz, and Bill J. Peck. The vortex rings created by bursting air bubbles and impacting water drops. In *Canadian Congress of Applied Mechanics*, 1995.
- [23] L.W. Sigurdson. The structure and control of a turbulent reattaching flow. *J. Fluid Mech.*, 298:139–165, 1995.
- [24] A. A. Campbell Swinton and Evelyn Beale. The bursting of bubbles. *Nature*, 98:469, 1917.

- [25] G. I. Taylor. On making holes in a sheet of fluid. *J. Fluid Mech.*, 58(4):625–639, 1973.
- [26] William Thomson. On vortex atoms. *Phil. Mag.*, 34:15–24, 1867.

CHAPTER 2

EXPERIMENTAL APPARATUS AND PROCEDURES

An Apparatus to Study the Vortex Structure Generated by a Bursting Bubble¹

2.1 Introduction

An apparatus has been developed to study, for the first time, vortex rings which are created by bursting bubbles. Since the only mentions of such vortex rings were either reporting casual observations (3), (8), or of a very preliminary nature (7), there was little direct assistance available in the literature for the construction of the apparatus. Fortunately the photographic equipment and techniques used by Peck et al. (6) are available and have been adapted for the present work.

The apparatus developed allows accurately timed photographs to be taken of the bursting bubble during its retraction, and of the motion of the gas

¹A version of this chapter will be submitted to Measurement Science and Technology for publication with this title.

ejected from the bubble. From these results, the vortex structure of the ejected gas may be modelled, and it is possible to begin learning about how the vorticity is generated.

Section 2.2.1 describes the preliminary apparatus and a critical discovery in positioning the bubble for photography. Section 2.2.2 describes the current state of the apparatus in detail. In particular and of note, Section 2.2.2.5 outlines the apparatus and procedures used to transport the aerosol flow visualization medium into the bubble while maintaining acceptable visibility. Section 2.2.2.6 discusses bubble pressure measurement, and Section 2.2.2.8 describes an original technique to measure the bubble surface tension. Some sample photographic data is presented in Section 2.3. Finally, conclusions are stated in Section 2.4.

2.2 Apparatus

This being the first attempt to study in detail, the phenomenon of the vortex structure created by a bursting bubble, several problems were encountered during apparatus development that have not been discussed previously in the literature. These are challenges such as positioning a floating bubble repeatably, injecting a flow visualization medium into a bubble, measuring the pressure inside a soap bubble, and determining the film surface tension while in position. Therefore, the apparatus was constructed through much experimentation, and consultation of theories from a variety of fields of study. It was determined that the apparatus must perform the following functions:

1. The bubble must be produced and positioned, during bursting, in the focus of a stationary camera.
2. A tracer must be injected into the bubble to enable visualization of the ejected gas.
3. The bubble must be burst on command so that photographs may be taken at a known time after bursting. If passive bursting occurs, the event must be either continuously recorded or the initiation of bursting must be detected.
4. Once film retraction is initiated a timing sequence must begin, enabling photographs to be taken at known times after the film has begun to retract. Of particular interest are the shape and velocity of the retracting film and the structure, velocity and size of the vorticity ejected from the bubble.

2.2.1 Development

In order to obtain preliminary data of the phenomenon, and test the repeatability of the experiment, the first stage of the apparatus was developed. The bubbles were supported on the face of a circular cylinder made of Teflon (25.4 mm in diameter), with its axis positioned vertically. The Teflon cylinder is shown in Figure 2.1. Bubble solution was made from distilled water, SunlightTM dishwashing liquid, glycerine, and fluorescein dye. Although SunlightTM, in particular, was used, it is surmised that other dishwashing

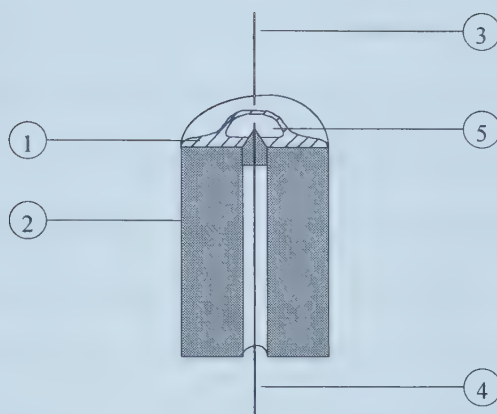


Figure 2.1: The Original Teflon Cylinder. (1) bubble solution, (2) Teflon cylinder, (3) & (4) electrodes, (5) bubble.

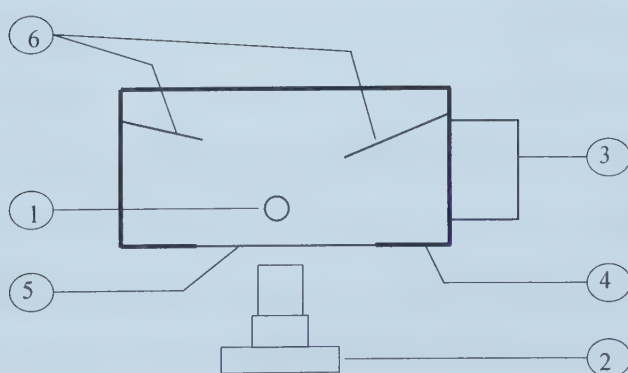


Figure 2.2: Plan View of Apparatus. (1) Teflon cylinder, (2) camera, (3) strobe, (4) test chamber, (5) window, (6) light deflectors.

liquids would have a similar effect. A set of electrodes were used to burst the bubble; one emerging along the vertical axis at the top surface of the cylinder and protected by a Teflon insulator; and one suspended from above, aligned with the bottom electrode. To generate a bubble on the surface of the cylinder, bubble solution was placed on the top surface of the cylinder, using an eyedropper, until a convex liquid surface was formed, covering the entire top surface. A syringe was then used to inject cigarette smoke (the tracer) just below the liquid surface, thus forming a bubble with a radius of curvature approximately 6-9 mm. When the bubble is formed on this surface, it was found to consistently position itself in the centre of the liquid pool - an event which is essential for repeatable positioning and symmetry of the bubble. This was a serendipitous and critical discovery. The Teflon cylinder was supported inside a plywood box to prevent ambient air currents from distorting the vortex structure emerging from the burst bubble. Photographs were taken using a Nikon F3 35 mm camera, and were illuminated by a General Radio Type 1540 Strobolume. A plan view of the experiment is given in Figure 2.2. A series of electronic timing devices were used to trigger the Strobolume at desired times after the spark burst the bubble so that the various stages of the vortex development could be photographed. More detailed information about this apparatus may be found in (1) (attached as Appendix C).

2.2.2 Current Apparatus

The preliminary version of the apparatus did not allow sufficient experimental control or measurement of bubble size and film properties, such as surface tension. The timing electronics were also cumbersome and unreliable due to interference caused by the high voltage spark electronics. Therefore considerable modification was required. The syringe was replaced by a stepper-motor-driven piston pump to accurately size bubbles, and modifications were made to the Teflon cylinder in order to accomodate bubble production using the pump. In addition, it is expected that cigarette smoke behaves as a surfactant on the bubble film, and that its temperature may have been greater than room temperature, further affecting bubble surface tension, and perhaps causing the ejected gas to be buoyant. Consequently, the smoke was replaced with an aerosol, which was made from bubble solution so that its effect on the film would be minimal. All components of the apparatus that come in contact with the bubble solution are made from either glass, Teflon or stainless steel, in order to withstand somewhat rigorous cleaning procedures. The experiment was also partially automated through the use of an *experiment controller* to sequence the operation of the lights, camera, and spark. The components and procedures of the current apparatus are discussed below.

2.2.2.1 The Teflon Cylinder

The bubble is generated, filled with aerosol, and positioned on top of the Teflon cylinder. Furthermore, the gauge pressure inside the bubble may be measured while positioned on the Teflon cylinder. Figure 2.3 shows a cutaway of the modified Teflon cylinder. Four structures are now present on the top surface: an electrode (present in the preliminary version), a Teflon cup 4.8 mm in diameter containing a 0.34 mm orifice for bubble inflation, a pressure port constructed of 1.6 mm O.D. Teflon tubing, and a 3.2 mm hole allowing the application of bubble solution to the surface of the cylinder. The orifice and bubble solution hole are each connected to passages through the cylinders exiting at the side of the cylinder, where Teflon tubing is attached. When producing a bubble, a drop of solution is placed in the Teflon cup, and aerosol is injected through the orifice to form the bubble. This process will be further discussed in Section 2.2.2.6. The Teflon cup has been adapted from the apparatus used by Haas (4).

2.2.2.2 The Test Chamber

The test chamber performs several functions. In the preliminary stage, its main, and perhaps still most important, function was to shelter the experiment from ambient air currents which were known to distort the structure ejected from the bubble. However, in the current experiment, the test chamber is also required to shield the sensitive timing electronics from radiation generated by the high voltage spark inside the chamber (increasing the relia-

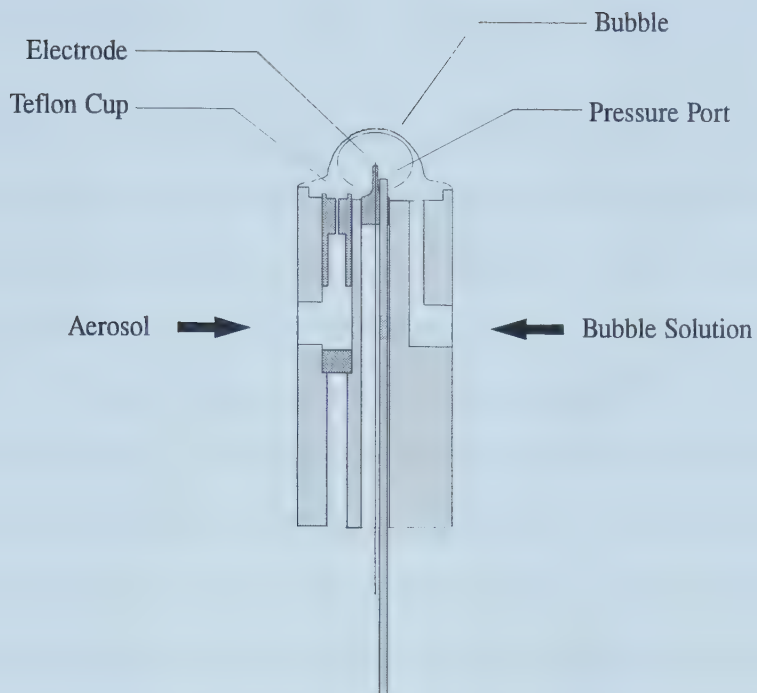


Figure 2.3: The Modified Teflon Cylinder

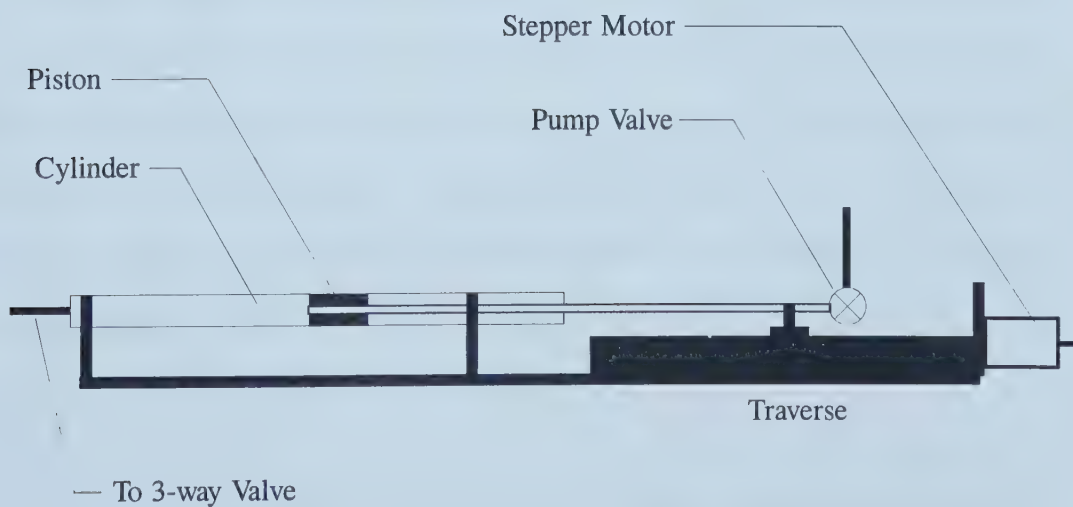


Figure 2.4: The Piston Pump

bility of the photographic equipment), and to physically support much of the experimental equipment. In the current test chamber, the plan-view layout is still very similar to that of Figure 2.2, and Figure 2.5 on page 22 shows the apparatus components contained within the test chamber. The chamber is a rectangular box of width 46 cm, depth 51 cm, and height 76 cm. It is constructed of 16 gauge steel, painted black to minimize strobe reflection inside, and grounded. The front of the test chamber contains a 10 cm hole, with an adjacent external tube 10 cm in diameter and 5 cm in length. The camera is positioned so that the lens is inside this tube and focused on the Teflon cylinder (which is inside the chamber, 4 cm from the wall). On each side of the test chamber, provisions are made for the external mounting of strobe lamps. An access door is located on the back wall. A 15 Watt fluorescent light is mounted inside the chamber, near the top, which is turned off when the camera shutter is opened. Light deflectors made from black poster board are placed inside the chamber to prevent the strobe(s) from illuminating the back wall, thus improving contrast in the photograph between the bubble or aerosol, and the background. Temperature inside the chamber is measured, near the Teflon cylinder, using a Hewlett Packard model 2180A RTD digital thermometer.

2.2.2.3 The Pump

The bubble is generated while simultaneously injecting aerosol using a stepper-motor-driven piston pump. The pump is mounted on a traverse and consists

of a 7.52 mm I.D. stainless steel cylinder with a Teflon piston. Fluid is pumped into a 1.75 mm I.D. stainless steel tube which is connected to the pump by a snug-fitting Teflon plug. Another 1.75 mm I.D. stainless steel tube penetrates through the length of the piston; the other end of the tube being secured to a single-axis traverse and connected to a Teflon valve. This tube thereby serves the purpose of connecting the piston and traverse, and functions as a vent by which the pump and piping may be primed with flow visualization medium. The stepper motor is controlled through the parallel port of a P.C. via an interface box. A diagram of the pump is presented in Figure 2.4.

2.2.2.4 The Spark Generating System

The spark generating system is composed of a device which we will refer to as the *spark generator*, an automobile ignition coil, and two electrodes. The system also interacts with two other components of the apparatus: the experiment controller and the timer trigger. A schematic of the experiment electronics, including the spark generating system, is given in Figure 2.5. The spark generator stores energy for the spark in a capacitor, and discharges it to the ignition coil on command. When the experiment is conducted, this event is triggered by a signal from the experiment controller. The result is a spark formed in the gap between the top electrode (attached to the ignition coil) and the bottom electrode (mounted in the Teflon cylinder). The spark generating system was initially at fault for constantly triggering the photo-

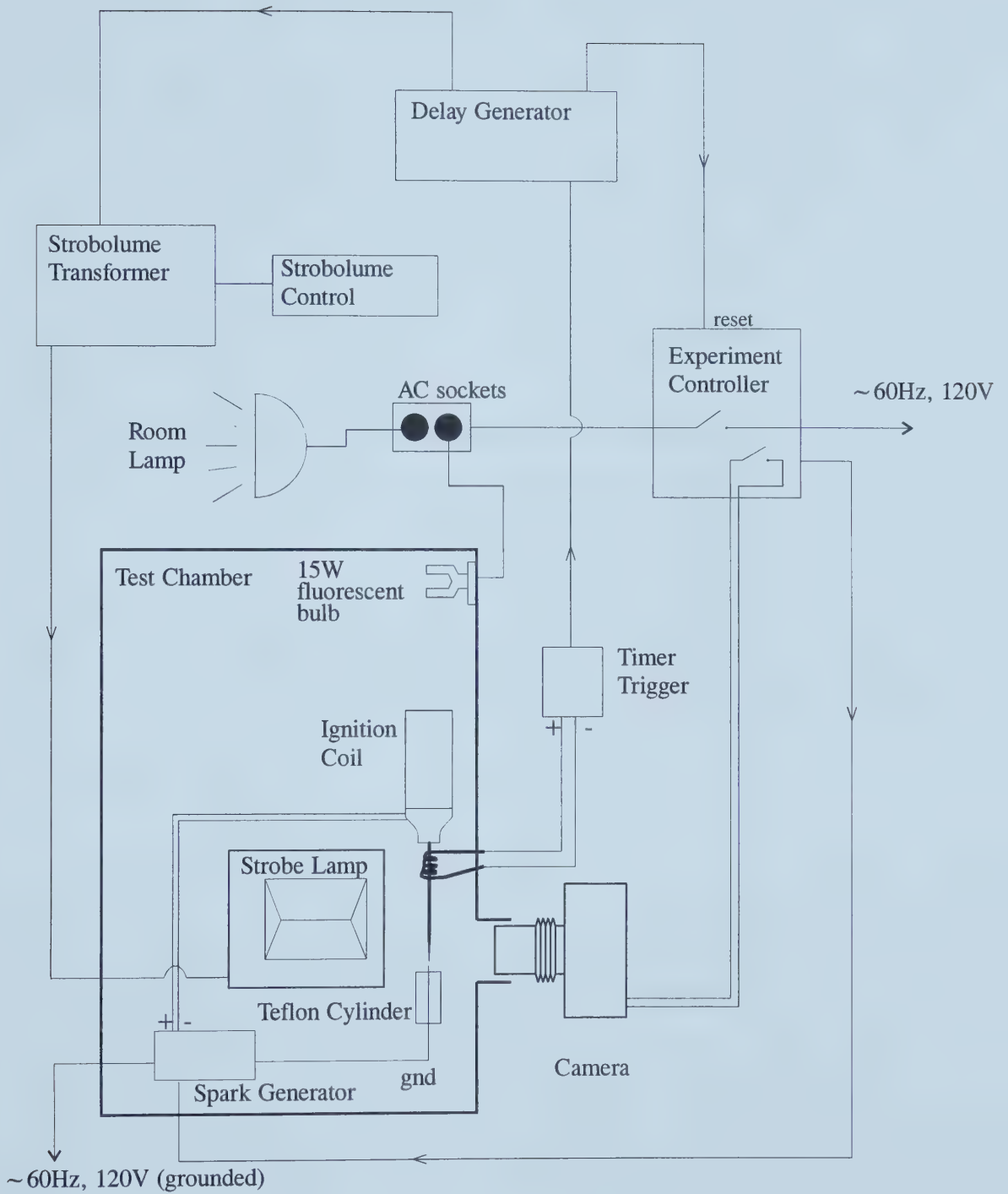


Figure 2.5: The Electronics

graphic timing electronics prematurely, and causing the experiment controller to randomly activate the camera, lights, and the spark generator itself. This problem was eventually solved with the help of Mr. Terry Nord and Mr. Bernie Faulkner by isolating the spark generator in three ways. First, as mentioned, it was contained in the grounded steel test chamber. Secondly, the spark generator's line cord was plugged into an isolating transformer in order to prevent significant noise from entering the building electrical system, and thus be transported to other components of the apparatus. Thirdly, an opto-isolator was used to prevent the spark generator from directly returning any noise to the experiment controller through the signal cable. The timer trigger detects the spark through an inductive coil of wire which is wrapped around the top electrode, and subsequently triggers the delay generator which times strobe flashes.

2.2.2.5 Aerosol Generation and Transport

The aerosol is generated using an UP-DRAFT II^R NEB-U-MIST^R nebulizer, manufactured by Hudson RCI. Compressed air is supplied by a DeVilbiss model 5650C Pulmo-Aide compressor. The aerosol consists of the same solution used to form the bubble film, which has the following components:

1. 375mL distilled water,
2. 0.5mL SunlightTM hand dishwashing liquid,
3. 7.5mL glycerin,

4. 300mg fluorescein.

The visibility of this aerosol is inferior to the previously used smoke, however, it is sufficient to study the motion and structure of the vorticity with adequate lighting and correct camera settings. The first three ingredients are sufficient for the bubble solution; however, fluorescein has been added to enhance the visibility of the aerosol. The glycerine and dishwashing liquid also significantly increase the aerosol visibility over that of pure water.

A schematic of the aerosol transport system is shown in Figure 2.6. Aerosol is introduced into the system via a 6.35 mm I.D. Tygon tube which connects the nebulizer to the side of a vertical cylindrical Teflon aerosol chamber (the primary aerosol chamber), through a toggle valve. The aerosol chamber is connected to the pump by a 1.75 mm I.D. stainless steel tube attached at the top of the chamber. Aerosol is transported to the Teflon cylinder through another 1.75 mm I.D. stainless steel tube connected to the bottom of the aerosol chamber. The purpose of this chamber is to facilitate the transport of aerosol to the bubble. The chamber is important. Without it, the aerosol in the bubble is too translucent to obtain photographs of the vortex structure, presumably due to the low number density of the particles. A 3-way valve is also located between the aerosol chamber and pump, which creates a branch connecting the bubble pressure port and pressure transducer. This valve connects the pump to either the aerosol chamber or the pressure port on the Teflon cylinder.

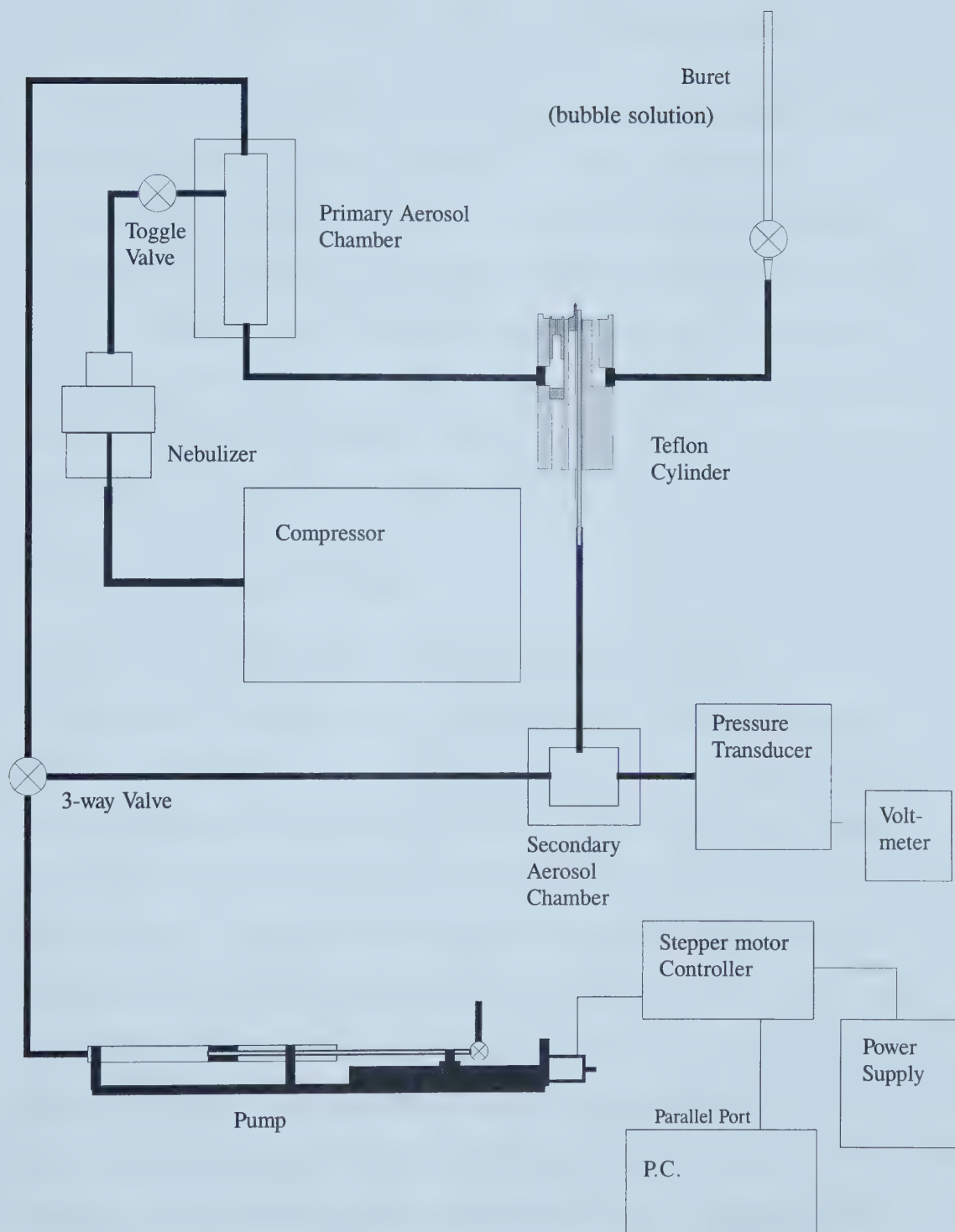


Figure 2.6: Aerosol and Liquid Transport System

Prior to formation of the bubble, the pump, aerosol chamber, and all tubing connected to the Teflon cup must be primed with aerosol. This is accomplished by opening the toggle valve on the primary aerosol chamber, and the valve on the piston pump; while positioning the 3-way valve such that it connects the primary aerosol chamber to the pump. The compressor is then turned on for about 5 seconds, which causes aerosol to flow through the system. During the priming procedure, aerosol exits the system through the piston pump valve, and the Teflon cup orifice.

2.2.2.6 Generation of the Bubble

It is desirable to measure the pressure of each bubble so that it may be used to determine the surface tension of the bubble film. The details of the calculation of the surface tension from pressure are discussed in Section 2.2.2.8. However, measuring the pressure in the bubble involves some additional procedures which result in the dilution of the aerosol finally existent in the bubble. Therefore, it is currently not possible to measure bubble pressure, then photograph the vortex structure generated by that bubble. As a result, two bubble generation procedures have been developed. One procedure involves measuring the pressure in the bubble, using a Setra Systems Inc. Model 264 pressure transducer, and photographing the bubble itself (procedure 1). The other procedure omits bubble pressure measurement and a photograph of the emerging vortex structure is obtained (procedure 2). Two sets of data are then obtained: one containing bubble photographs and pressures, and one

containing photographs of the vortex structure. The underlying assumption is that measuring the pressure will not significantly effect the size or any other property of the bubble.

Two sizes of bubbles have been studied with the current Teflon cylinder. The range of sizes is limited by the largest bubble which will float on the liquid surface without becoming noticeably distorted by the limited base width, and the smallest bubble which will still manage to centre itself over the electrode and pressure port. The volumes of the large and small bubbles are $2.0 \times 10^{-6} m^3$ and $1.2 \times 10^{-6} m^3$, respectively.

Procedure 1 is much more complicated than procedure 2. Procedure 1 begins with priming the system as described in Section 2.2.2.5. Then, the pressure port and secondary aerosol chamber are primed with aerosol by appropriately adjusting the 3-way valve and pumping $3.4 \times 10^{-6} m^3$ of aerosol through the pressure port, using the piston pump. The 3-way valve is switched again, and the bubble is formed by pumping $1.9 \times 10^{-6} m^3$ of aerosol through the Teflon cup after manually applying a drop of bubble solution to the top of the Teflon cup with an eyedropper. Bubble solution is subsequently applied to the surface of the Teflon cylinder, regulated with the stopcock of a buret, until the bubble floats and centres itself on the cylinder. The 3-way valve is again switched, connecting the pressure port, and $4.5 \times 10^{-7} m^3$ is pumped in order to clear the port of liquid which will otherwise influence the measured pressure. Finally, a volume of aerosol is drawn back in through the pressure port, reducing the bubble to the desired size. At this point, the pressure at

Table 2.1: Bubble Shrinkage Caused by Pressure Measurement

Day	Avg. Radius of Curvature w/o Pressure Measurement (mm)	Avg. Radius of Curvature with Pressure Measurement (mm)	% Reduction
A	8.55	8.44	1.29
B	8.60	8.27	3.84
C	8.49	8.31	2.12

the pressure transducer and the pressure inside the bubble are equal.

Procedure 2 involves only priming the piping system as described in Section 2.2.2.5, blowing the bubble to the desired volume in one stage, then applying bubble solution to the cylinder until the bubble is centred.

Table 2.1 shows the average radii of curvature measured, of small bubbles produced on 3 different days. It is evident from this data that measuring bubble pressure has the effect of reducing the size of the bubble. This shrinkage also occurs with the large bubbles, but is not as significant. The proposed explanation for this observation is that when the bubble pressure is measured, the bubble volume is exposed to a significant, depressurized volume in the secondary aerosol chamber: additional tubing, and the pressure transducer. This causes some flow out of the bubble until the pressures are equalized. For the large bubbles, this effect is less because they have a larger volume, and the pressure is slightly lower.

2.2.2.7 Photography and Timing

Three types of images were obtained: single exposure 35 mm photographs, multiple exposure 35 mm photographs, and a limited amount of VHS video. Because timing was not required when capturing the video images, this discussion will apply mainly to 35 mm photography.

Photographs are taken using a Nikon F3 camera with a 55 mm Micro Nikkor lens, and a B+W UV haze filter to protect the lens from drops shed by the bursting bubble. A Nikon PB-6 bellows was also used for most of the photographs. With the lens set to an F-stop of 2.8, the depth of field is approximately 2 or 3mm, and the camera is positioned so that the centre of the Teflon cylinder is in focus. Photography is done by turning off the room lights, opening the camera shutter, then bursting the bubble and discharging a strobe at specified times afterward to record images. The first three tasks are performed by the experiment controller, which also closes the shutter and turns on the lights after completion of the experiment. Most of the images are recorded on Kodak Ektachrome Elite II 400 ASA slide film. However, one roll of Ektachrome P1600 slide film was used to obtain multiple exposure photographs under reduced lighting, and at later times ($\geq 100ms$) when the aerosol has become too dilute to record at 400ASA. The P1600 film was pushed to 1600 ASA, however this caused the film to be overexposed, so it is predicted that the standard process (800 ASA) will give the optimum exposure.

The timing electronics are shown in Figure 2.5. When the spark is de-

tected by the timer trigger, a signal is sent to the input of the delay generator. The delay generator was designed and built in-house by Mr. Bernie Faulkner. It is controlled by a 1MHz oscillator, and is capable of timing ten output signals with a resolution of $1\mu s$ through either individual parallel outputs, or a serial output. The delay generator triggers either a General Radio model 1540 Strobolume, or a model 1531 Strobotac, which then flashes and records an image on film.

The strobolume emits a higher intensity burst than the Strobotac, and must be used at the high intensity setting in order to adequately illuminate the aerosol with 400 ASA film. At this intensity, the strobolume discharge is adequately brief to freeze the motion of the aerosol. The recharge time at high intensity is approximately 85 ms, which is too long a delay for useful multiple exposures of the vortex structure. In such a case, medium intensity has been used with the P1600 film. At medium intensity, the recharge time is approximately 13 ms. To photograph the retracting film, the high intensity Strobolume flash is too long to freeze the motion of the film rim. Therefore medium intensity or a strobotac must be used. Multiple exposure photographs of the retracting film occur at time intervals much less than the recharge time of the strobes, so a single strobe must be used for each exposure.

2.2.2.8 Experimental Control and Bubble Surface Tension Measurement

Ambient conditions such as temperature and humidity are not controlled to any greater extent than that provided by the building air-conditioning systems. Therefore experimental parameters such as bubble surface tension, and the densities and viscosities of the bubble solution and air are, to some extent, beyond our control. Yet, it is considered important that the bubble solutions be of similar composition and have a minimum of impurity to control bubble properties to the extent that it is possible. To minimize impurities, a simple cleaning procedure is used. All components of the apparatus and glassware which contact the bubble solution are first washed with tap water, and soap if necessary. Everything is rinsed with distilled water, then with acetone, before thoroughly flushing again with distilled water. The items are then allowed to dry in an environment sheltered from airborne dust particles, etc. If further control is required in future variants of this apparatus, an environment-controlled test cell will be used such as in (6), and more rigorous cleaning procedures will be required.

It is expected that bubble surface tension has a significant effect on properties of the vortex structure, since it affects both film retraction speed (2) and bubble pressure. Due to the limited control of ambient properties with this apparatus, it is desirable to determine the surface tension for as many bubbles as possible. The surface tension of an interface is related to the pressure difference across the interface, and the principal radii of curvature of the interface by Laplace's *other* equation (not to be confused with $\nabla^2\phi = 0$,

where ϕ is a scalar):

$$\Delta P = \gamma \left(\frac{1}{R_1} + \frac{1}{R_2} \right), \quad (2.1)$$

where ΔP is the pressure difference across the interface, γ is the surface tension of the interface, and R_1 and R_2 are the principal radii of curvature. If a bubble film is considered to have two interfaces (one on each side of the film), and constant curvature, and the weight of the film is neglected, Laplace's equation reduces to:

$$\Delta P_b = \frac{4\gamma}{R}. \quad (2.2)$$

Here, ΔP_b is the bubble gauge pressure, γ is the surface tension of one interface, and R is the bubble radius of curvature.

By measuring the bubble curvature and pressure, the surface tension can be found for an individual bubble. To our knowledge, this is the first measurement of surface tension using this technique. However, as it was mentioned in Section 2.2.2.6, the pressure cannot be measured on the same bubble which produces a visible vortex structure. Table 2.2 contains some surface tensions calculated from measurements taken on 4 different days, along with the sample standard deviation, average temperature, and sample size for each day.

Table 2.2: Calculated Surface Tensions

Day	Sample Size	γ (dynes/cm)	γ sample standard deviation (dynes/cm)	average temperature °C
1	6	28.4	0.22	21.0
2	6	28.5	0.27	20.8
3	5	28.6	0.13	21.7
4	7	28.6	0.16	21.4

2.3 Results

Figure 2.7 contains sample single-exposure 35 mm photographs recording film retraction and the evolution of the vortex structure. In Figure 2.7(b) Kelvin Helmholtz vortices are visible on the sides of the aerosol. These eventually organize themselves into two vertically-aligned vortex rings which leapfrog and finally form the vortex ring and lobes shown in Figure 2.7(c). This final form is similar to the structure formed by an impacting water drop, presented in (5). The photographs taken with this apparatus are, to our knowledge, the first detailed photographs ever taken of the vortex ring emerging from a bursting bubble. Detailed results of this process are contained in Chapter 3.

2.4 Conclusions

An apparatus to study vortex rings generated by bursting bubbles has been discussed. A Teflon cylinder has been devised to position the bubble and facilitate its generation and injection with aerosol. A simple, although somewhat intrusive, procedure was developed for measuring the gauge pressure inside the bubble, in order that the surface tension may be calculated. A



(a) film retraction (1 ms)



(b) vortex structure in development (7 ms)



(c) the vortex ring (100 ms)

Figure 2.7: Photographic Data

system was developed to generate aerosol, and transport it into the bubble in such a way that it is still easily visible when the vortex structure is photographed after bursting. Single and multiple exposures have been obtained to study the structure and motion of the retracting bubble film, and the ejected vortex structure.

Bibliography

- [1] James Buchholz, Lorenz Sigurdson, and Bill Peck. An apparatus to study vortex rings emerging from bursting air bubbles. In J. Crowder, editor, *Proceedings of the Seventh International Symposium on Flow Visualization*, pages 146–151, New York, 1995. Begell House Inc.
- [2] F. E. C. Culick. Comments on a ruptured soap film. *J. Appl. Phys.*, 31(6):1128–1129, 1960.
- [3] J. A. Day. Production of droplets and salt nuclei by the bursting of air-bubble films. 90:72–78, 1964.
- [4] Jean francois Luc Haas. *Interaction of Weak Shock Waves and Discrete Gas Inhomogeneities*. PhD Thesis, Caltech, 1984.
- [5] Bill Peck and Lorenz Sigurdson. The three-dimensional vortex structure of an impacting water drop. *Phys. Fluids*, 6(2):564–576, February 1994.
- [6] Bill Peck, Lorenz Sigurdson, Bernard Faulkner, and Ian Buttar. An apparatus to study drop-formed vortex rings. *Measurement Science and Technology*, 6:1538–1545, 1995.
- [7] W.B. Rogers. On the formation of rotating rings by air and liquids under certain conditions of discharge. *Am. J. Sci. Arts. Sec. Ser.* , 26:246–258, 1858.

- [8] A. A. Campbell Swinton and Evelyn Beale. The bursting of bubbles.
Nature, 98:469, 1917.

CHAPTER 3

THE EXPERIMENT, COMPUTATIONAL MODEL, RESULTS, AND DISCUSSION

The Kinematics of the Vortex Structure Generated by a Bursting Bubble¹

3.1 Introduction

This chapter presents and discusses the results of this study. Section 3.3 discusses the experimental results. In Section 3.3.1, bubble properties and the kinematics of film retraction are investigated. Section 3.3.2 discusses the vortex structure, beginning with a vortex model of its evolution in section 3.3.2.1, then particular properties of the structure are presented in Section 3.3.2.3. After the recent investigation is discussed, some preliminary results are then presented in Section 3.3.2.4 where a cigarette smoke visualization

¹A version of this chapter will be submitted to the Physics of Fluids for publication with this title.

medium was used, and some differences between these and the current data are pointed out. In Section 3.3.3, experiments on passively bursting bubbles are reported. In Sections 3.4 and 3.5, a two-dimensional point vortex model of the phenomenon is introduced, and results are reported. Finally, conclusions are summarized in Section 3.6.

3.2 Apparatus

The experimental apparatus is described in Chapter 2.

3.3 Experimental Results and Discussion

3.3.1 The Bubble

3.3.1.1 Bubble Properties Before Bursting

In this study, two sizes of bubbles were used. These sizes were the largest bubble which would float on the liquid surface without becoming noticeably distorted, and the smallest bubble that would still centre itself over the electrode and pressure port extending from the Teflon cylinder. From now on, we will refer to these two bubble sizes as *large* and *small*. The large bubbles were created by a $2.0 \times 10^{-6} m^3$ displacement of the piston pump, and the small bubbles were created by a $1.2 \times 10^{-6} m^3$ displacement of the piston pump. For the current investigation, the bubbles are assumed to contain approximately these volumes.

The radii of curvature of the bubbles were determined by projecting the

photographs of the bubbles onto a piece of paper, using a slide projector, then tracing the projected image. The Teflon cylinder diameter was used to scale the projected bubble radius. It is estimated that the radii of curvature have been obtained to an accuracy of 0.01 mm. When superimposing a 'best-fit' circle, using a compass, over the traced bubble, it was found that any deviation of the trace from this circle was within this error. It is therefore concluded that the shape of the bubble follows a sphere for a region *sufficiently removed* from the base where the curvature rapidly changes. This sufficiently removed region is defined as that enclosed by the angles with vertices on the centre of curvature of the bubble, and extending 70° to the right and left, from the vertical, as shown in Figure 3.1.

Table 3.1 displays the radius of curvature, gauge pressure, surface tension, and ambient temperature for a sample of bubbles made on various days. Bubbles a to d are large, and bubbles e to h are small. The radii of curvature have been measured in the manner described in the preceding paragraph, and the gauge pressure has been obtained using the method of Section 2.2.2.6. Using these two measurements, and Laplace's Equation 2.2, the surface tension was derived. The ambient temperature is also reported for each bubble. By scanning the last two columns of Table 3.1, no obvious correlation between temperature and surface tension is found, indicating that there are other factors significantly influencing the surface tension. Conversely, there is reasonable consistency in the film surface tension, as the total variation of the representative values of Table 3.1 are within 2%. Bubble pressures and

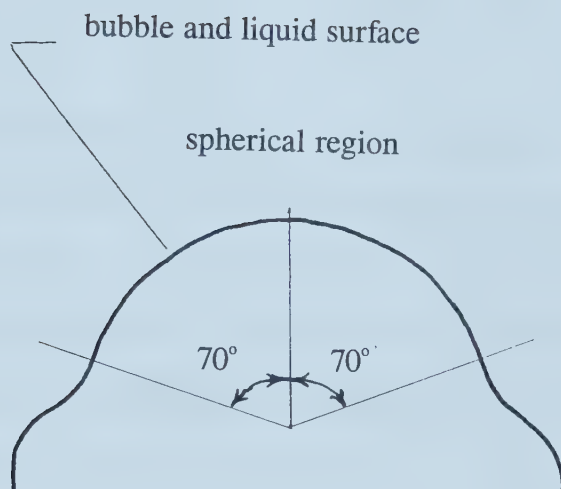


Figure 3.1: Spherical Region of Bubble

Table 3.1: Bubble Properties

Bubble	Radius of Curvature, R (mm)	Gauge Pressure, ΔP_b (Pa)	Surface Tension, γ ($dynes/cm$)	Ambient Temperature, T ($^{\circ}C$)
a	9.63	11.9	28.6	21.2
b	9.33	12.2	28.5	20.6
c	9.58	11.9	28.5	21.0
d	9.46	12.0	28.4	21.3
e	8.47	13.3	28.2	20.6
f	8.45	13.5	28.5	21.1
g	8.23	13.6	28.0	21.5
h	8.48	13.4	28.4	21.7

radii of curvature have a slightly larger variation. At the present time, these measurements are not yet being scaled with properties of the emerging vortex rings. However, in the future, if it is found that more consistent results are required, the apparatus will have to be modified to accomodate the greater precision. As predicted by Equation 2.2, the gauge pressures of the small bubbles are greater than those of the large bubbles.

3.3.1.2 Film Retraction

When the bubble bursts, the stored potential energies in the film, and in the compressed bubble air are transformed into kinetic and thermal energy in the air and in motion of the retracting film. This transformation forms the initial conditions of the vorticity, and an understanding of this phenomenon is therefore important to gaining insight on the mechanisms of vorticity generation at an air/water interface, and to modelling the generated vorticity.

The mechanism of vorticity generation in this experiment is still not well understood. However, some information about the vorticity generation can be gained by studying the kinematics of the film as it retracts.

Figures 3.2 and 3.3 contain photographic sequences depicting the film throughout its retraction into the pool at its base. Upon generation of the spark, the film begins to retract radially outward from the region at which it was pierced. As the film retracts, the edge of the film thickens, forming a *rim*. McEntee and Mysels (3) noted an additional slight thickening of the film in the region adjacent to the rim, which they called the *aureole*. This aureole has not been observed on the bursting bubble using our photographic technique. Eventually, the rim begins to shed drops in its wake. Many of these drops form a circumferential extension resembling a *crown* perpendicular to the surface of the film, such as those shown in Figures 3.2(f) through 3.2(h) and 3.3(f) through 3.3(h). It is inferred that this crown is formed by drops shed at earlier times, whose trajectories have carried them beyond the bubble boundaries. The trajectories of the drops are assumed to be determined by the direction of travel of the rim at the time of their release, and by a centrifugal force applied as the rim follows the spherical film. It has been observed that the rim is not axisymmetric about the spark, but that its edge is jagged. This was also noted by McEntee and Mysels (3), and was attributed to *sputtering* of metal or oxide from the electrodes as the spark is discharged, resulting in multiple initial holes in the film. However, since this *jaggedness* of the rim is likely associated with drop generation which has



(a) the large bubble



(b) $t = 10 \mu\text{s}$

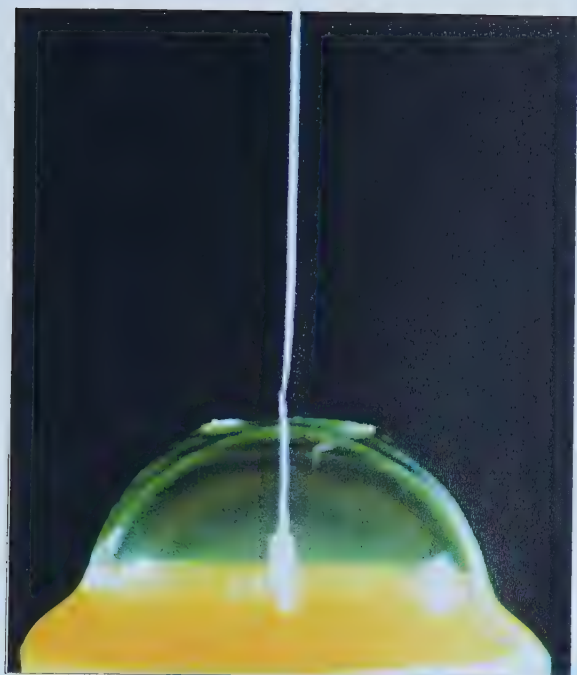


(c) $t = 50 \mu\text{s}$

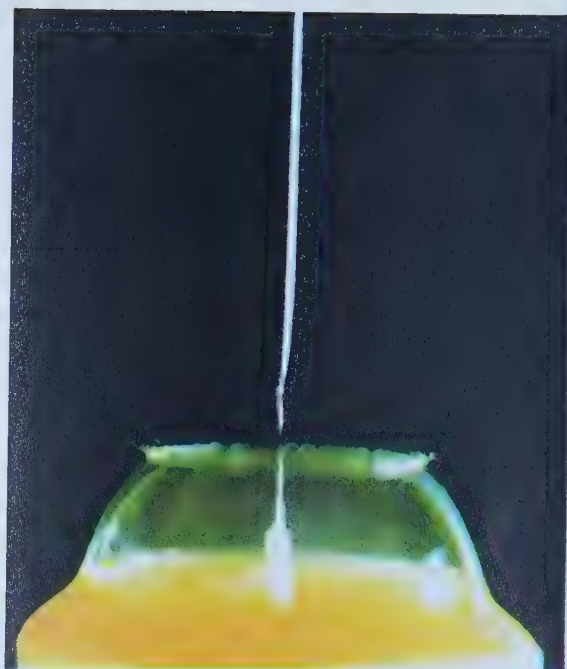


(d) $t = 150 \mu\text{s}$

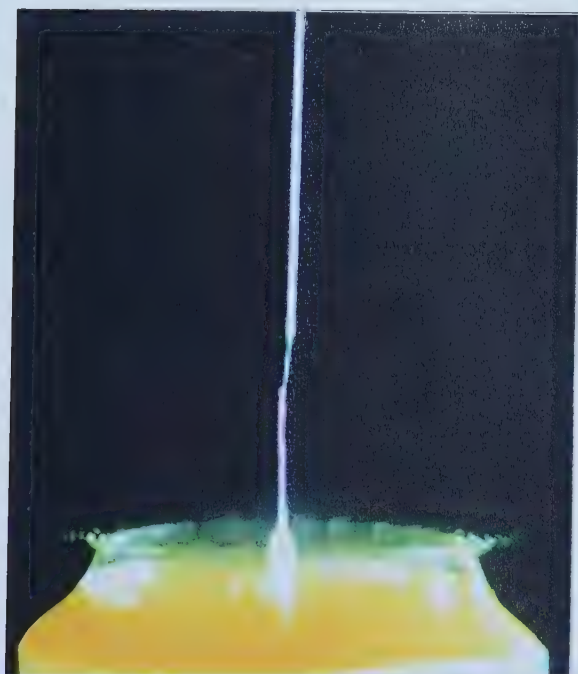
Figure 3.2: The Large Bubble Bursting



(e) $t = 250 \mu\text{s}$



(f) $t = 750 \mu\text{s}$



(g) $t = 1250 \mu\text{s}$



(h) $t = 1750 \mu\text{s}$

Figure 3.2: The Large Bubble Bursting (cont.)



(a) the small bubble



(b) $t = 10 \mu\text{s}$



(c) $t = 50 \mu\text{s}$



(d) $t = 150 \mu\text{s}$

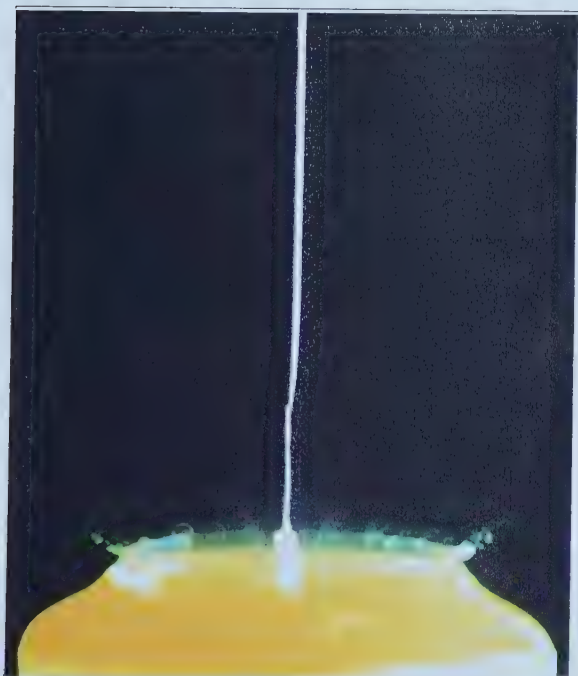
Figure 3.3: The Small Bubble Bursting



(e) $t = 250 \mu\text{s}$



(f) $t = 750 \mu\text{s}$



(g) $t = 1250 \mu\text{s}$



(h) $t = 1750 \mu\text{s}$

Figure 3.3: The Small Bubble Bursting (cont.)

been found, for example, by Day (2) to occur in naturally bursting bubbles, it is surmised that the jaggedness may be at least partly a result of a natural instability in the rim. Finally at approximately 1.5 ms, the film rim retracts into the bulk fluid at the base of the bubble. This event may be interpolated by comparing the last two photos of Figures 3.2 and 3.3. In Figures 3.2(h) and 3.3(h) the rim has already retracted into the pool, leaving the crown of shed drops, and a ring-shaped ridge of bulk fluid on the liquid surface.

Culick (1) used an energy balance to calculate the constant rim velocity of a retracting horizontal soap film, assuming uniform thickness h , and uniform fluid properties, and ignoring the effects of gravity and aerodynamic drag. His derived equation for the velocity is:

$$U_f = \left(\frac{2\sigma}{h\rho}\right)^{\frac{1}{2}}, \quad (3.1)$$

where U_f is the constant velocity of the rim travelling radially from the point of puncture, σ is the surface tension of the film (the combined effect of the top and bottom interfaces; $\sigma = 2\gamma$ by the assumption of Equation 2.2), h is the film thickness, and ρ is the film density. It is interesting to note that this equation is independent of fluid viscosity. The bursting bubble differs from this idealized film in that it is spherical. Therefore, the film rim does not travel in a plane, but along the surface of a sphere. Gravity also becomes significant to the retraction speed as the bubble film has a vertical component, and therefore draining may occur causing the film thickness and

properties to change - therefore the parameter of time is also significant. In their experimental study of plane bursting films, McEntee and Mysels (3) reported good agreement with Equation 3.1 for films of thickness greater than 1000 Angstroms.

From side photographs of retracting bubble films, displacements of the leading edge of the film rim were measured at various times after spark initiation. These displacements were measured along the bubble perimeter extrapolated from the geometry of the remaining portion of film. It was assumed that retraction initiated at the intersection of the bubble perimeter and the sides of the spark, at the time that the delay generator was triggered. This assumption may be somewhat questionable by the *sputtering* theory of McEntee and Mysels (3). For each photograph, two measurements were taken; the rim displacement on the left side of the spark, and that on the right side. Each photograph then represents a cross-section of the bubble. Figure 3.4 plots the averaged $((\text{left} + \text{right})/2)$ displacements of the rim from three sets of bubbles, at various times between $250 \mu s$ and $1500 \mu s$ after the initiation of the spark. Linear regression was used to fit lines to these data sets, in order to determine the slopes and intercepts. The results of the regression are given in Table 3.2. It is evident that the film rim does not travel at constant speed from the initial point of puncture as there exists a non-zero displacement intercept. This suggests that either the rim is travelling more quickly at earlier times, or that the spark initially annihilates a region of the film significantly larger than its own cross-sectional dimension.

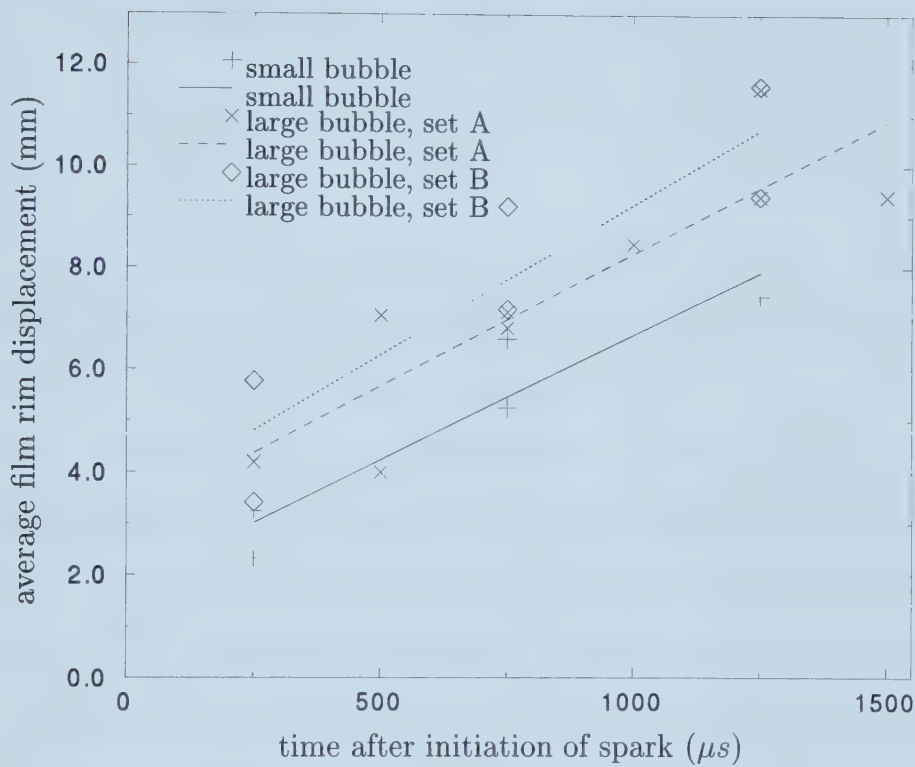


Figure 3.4: Averages of left and right side film rim displacements. The small bubble data, and set B of the large bubble were obtained on the same day. Each data point is taken from an individual bubble. The velocities (slopes) of the rims are approximately the same; however, the large bubble rims have advanced further than those of the small bubbles.

Table 3.2: Linearized Film Retraction Velocities and Intercepts

Data Set	Film Velocity (slope) (m/s)	Intercept ($t = 0$) (mm)
small	4.88	1.80
large, set A	5.21	3.07
large, set B	5.91	3.33

Table 3.3: Linearized Film Retraction Velocities and Intercepts (early retraction)

Data Set	Film Velocity (slope) (m/s)	Intercept ($t = 0$) (mm)
small	10.9	0.50
large	13.1	1.24

To gain insight on the kinematics of the film rim at earlier times, photographs such as those in Figures 3.2(b) through 3.2(d) and 3.3(b) through 3.3(d) were taken. The left/right averaged displacements of these films are plotted in Figure 3.5, and the fitted velocities and intercepts, in Table 3.3. By comparing Tables 3.2 and 3.3, it can be concluded that the rim velocities within the first $150 \mu\text{s}$ are approximately twice those of the remainder of film retraction. To visualize this, the two plots have been superimposed in Figure 3.6. A comparison of Tables 3.2 and 3.3 also reveals that the displacement intercepts are significantly reduced by considering the early film retraction, but are still significant. This non-zero intercept indicates either yet greater rim velocities at earlier times, or a larger initial hole than that assumed - possibly explained by electrode sputtering.

Another interesting conclusion can be made by observing Figures 3.4 and 3.5. The average displacements of the large bubble rims (as indicated by the superimposed lines) are significantly greater than those of the small bubbles at any time. This is also reflected in the greater displacement intercepts of the large bubbles in Tables 3.2 and 3.3. It is suspected that this is the integrated result of a higher film retraction velocity for the large bubbles,

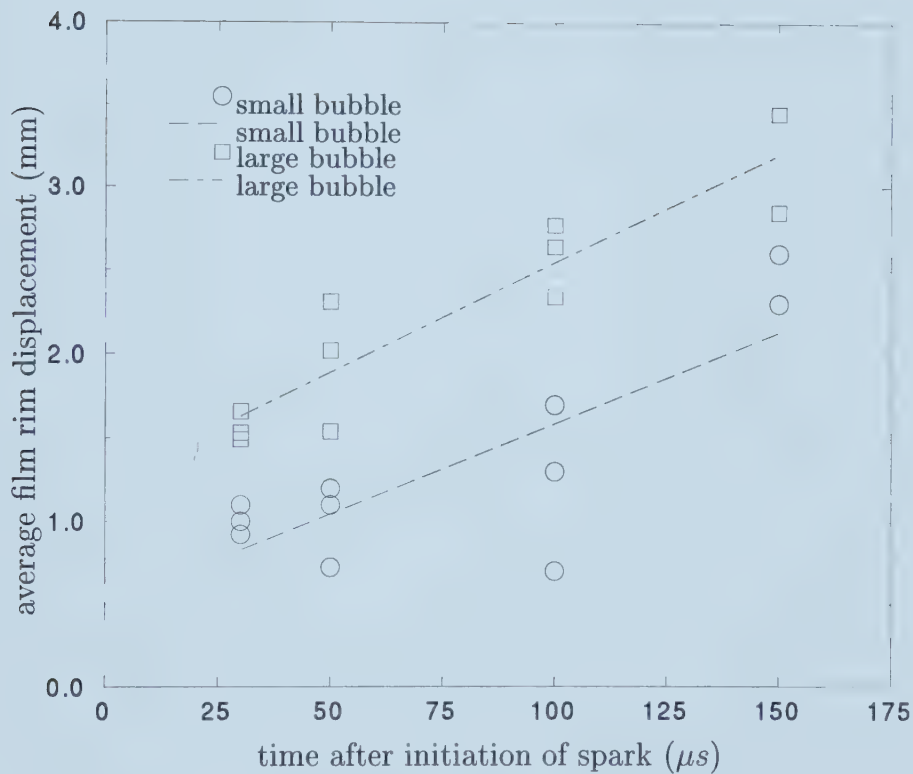


Figure 3.5: Early averaged film rim displacements. These are displacement data measured at earlier times than in Figure 3.4. The linearized velocities here are greater than at the later times (10.9 m/s for the small bubbles, and 13.1 m/s for the large bubbles). Both sets of data were taken on the same day, but a different day than any of the data of Figure 3.4.

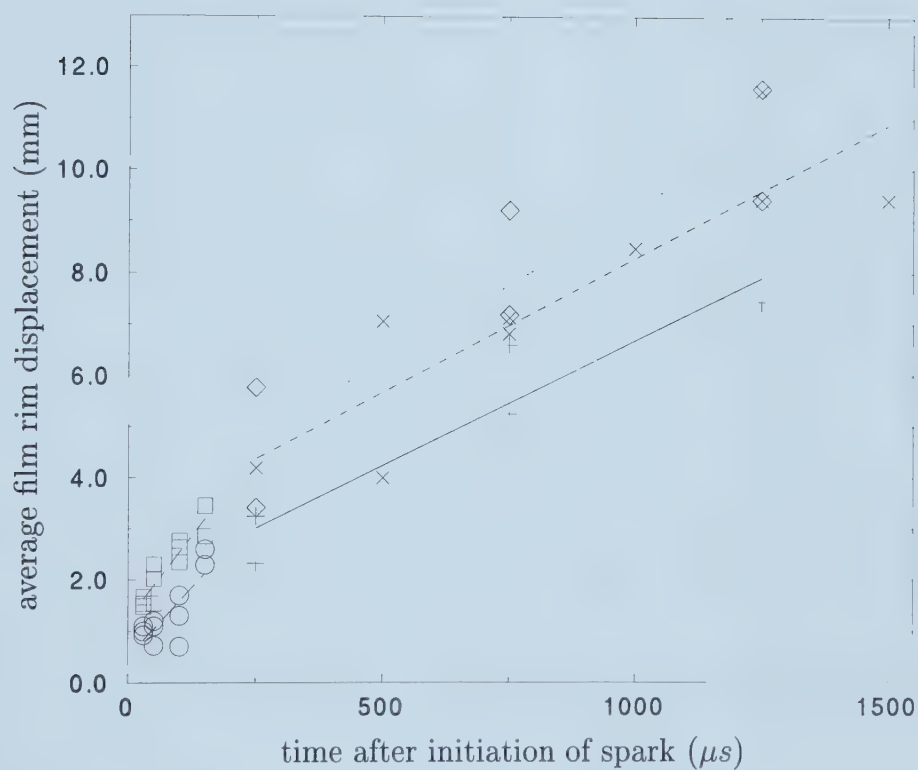


Figure 3.6: Superposition of Figures 3.4 (film retraction) and 3.5 (early film retraction). Legend is found in Figures 3.4 and 3.5.

since the large bubble retraction velocities are consistently reported higher in Tables 3.2 and 3.3.

It has been mentioned that the film rim is not radially symmetric about the point of puncture, but contains jagged edges. In our experiments, it has also been found that the rim displacements are skewed, with the right side displacement being consistently greater than the left, as shown in Figure 3.7. This asymmetry has enabled us to gain an additional piece of information about the early rim velocity. It is thought that this skewedness results from the bubble being initially pierced, by the spark, at a point deviating from the centre, or top, of the bubble. This in itself is not to be interpreted as a reason for the asymmetry as the right and left displacements are measured from the spark, not from the top of the bubble. However, if a velocity gradient exists such that the rim travels more quickly at higher latitudes on the bubble, owing perhaps to a gradient of film thickness in the opposite direction, then piercing the bubble to the left of centre will result in a greater initial rim velocity to the right than to the left, thus explaining the skewed displacements.

Double exposure photographs were used to approximate the rim velocity by measuring its distance of travel during the delay between the two exposures. Sample double exposure photographs of the large and small bubble are shown in Figure 3.8. Tables 3.4 and 3.5 display the times of the exposures (t_n), the left and right displacements between exposures (Δ_L and Δ_R), the averaged (left and right) displacement ($\bar{\Delta}$), and the averaged rim

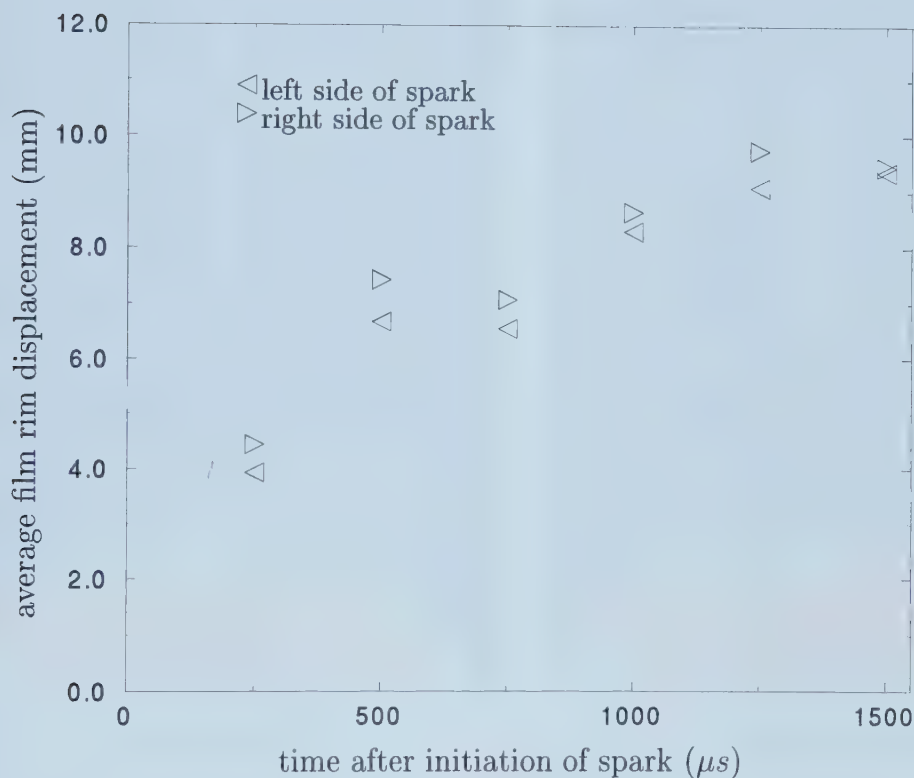


Figure 3.7: Separation of left and right film rim displacements. Some of the points from set A of the large bubble retraction photos are plotted unaveraged. Only one data point at each time is plotted so that the right and left displacements may be compared for each case. In the plot, the right displacement is larger for all photos, and this is also true of all points in this data set. In all the data taken, there are only a couple of exceptions.



(a) large bubble



(b) small bubble

Figure 3.8: Double Exposure Photographs of the Bursting Bubble ($600\ \mu\text{s}$ and $800\ \mu\text{s}$)

Table 3.4: Film Retraction Velocities Derived from Double Exposure Photographs (large bubbles)

Bubble	t_1 (μs)	t_2 (μs)	Δ_L (mm)	Δ_R (mm)	$\bar{\Delta}$ (mm)	\bar{U}_f (m/s)
1	200	400	1.77	1.85	1.81	9.05
2	200	400	1.77	1.85	1.81	9.05
3	600	800	1.35	1.35	1.35	6.75
4	600	800	1.30	1.20	1.25	6.25

Table 3.5: Film Retraction Velocities Derived from Double Exposure Photographs (small bubbles)

Bubble	t_1 (μs)	t_2 (μs)	Δ_L (mm)	Δ_R (mm)	$\bar{\Delta}$ (mm)	\bar{U}_f (m/s)
5	200	400	1.29	1.37	1.33	6.65
6	200	400	1.36	1.21	1.29	6.45
7	600	800	1.43	1.35	1.39	6.95
8	600	800	1.27	1.12	1.20	6.00

velocity based on $\overline{\Delta}$. Two intervals have been studied for both bubble sizes; 200 μs to 400 μs , and 600 μs to 800 μs . In Table 3.4, it is evident that the rim is retracting at a higher velocity in the earlier interval than it is in the later interval. For the small bubbles (Table 3.5), such a distinction cannot be made as the two intervals have similar velocities. In comparing the last column of both tables, it is evident that during the first interval (200 μs to 400 μs), the rims of the large bubbles are moving faster than those of the small bubbles; however, at later times, the rim velocities are similar between the two bubbles.

3.3.2 The Vortex Structure

3.3.2.1 Evolution

The evolution of the vortex structure is represented photographically in Figure 3.9 for the large bubbles, and in Figure 3.10 for the small bubbles. These photographs are the results of individual experiments, not a sequence of images of a single event. They are therefore only representative samples of the structure at each instant, and other samples at similar times usually have differences in size, vertical displacement, and symmetry. These variations will be discussed later. Figure 3.11 contains our interpretation of the vortex kinematics present in the initial stages of the photographic sequence, which is topologically similar for both bubble sizes. These diagrams contain sketches of the two-dimensional aerosol profiles (from the photos of Figure 3.9) with the estimated locations of the cross-sections of the vortex cores superimposed.

The actual sizes and shapes of the cores are speculated and may be quite different than represented. Possible representations of the vortex topology at later times are given in Figures 3.12 and 3.13.

At 3 ms after the initiation of film retraction and approximately 1.5 ms after the film rim retracts into the pool, the aerosol is still approximately hemispherical in shape. Figures 3.9(a) and 3.10(a) contain photographs of the structures from the large and small bubbles, respectively. The presence of vorticity is indicated by the apparent vortex-like distortions of the aerosol interface. An idealization of the aerosol profile is given in Figure 3.11(a). At the top of each of the clouds in the two figures, is a void of aerosol, or dark region, resulting from the incursion of clear air from above. This perhaps indicates the presence of a complex arrangement of vorticity which is entraining the air. However, it will be shown in Section 3.5 that such an observation may be possible without this complex arrangement of vorticity. It is expected that one or more vortex sheets exist on the surface of the cloud since it is hypothesized that the vorticity has been primarily generated at the air/film interface. However, the mechanism of vorticity generation at an air/water interface is not well understood in general, and therefore little is known about the structure of the vorticity just after film retraction. This experiment presents the first data on this phenomenon. As mentioned earlier, this investigation was partly motivated by the desire to understand more about how the vorticity is created in the general case. Speculation about the initial vorticity distribution will be discussed in Section 3.4.



(a) $t = 3 \text{ ms}$



(b) $t = 7 \text{ ms}$



(c) $t = 11 \text{ ms}$



(d) $t = 15 \text{ ms}$

Figure 3.9: Evolution of the Vortex Structure Emerging from the Large Bubble



(e) $t = 20$ ms



(f) $t = 35$ ms



(g) $t = 35$ ms



(h) $t = 45$ ms

Figure 3.9: Evolution of the Vortex Structure Emerging from the Large Bubble (cont.)

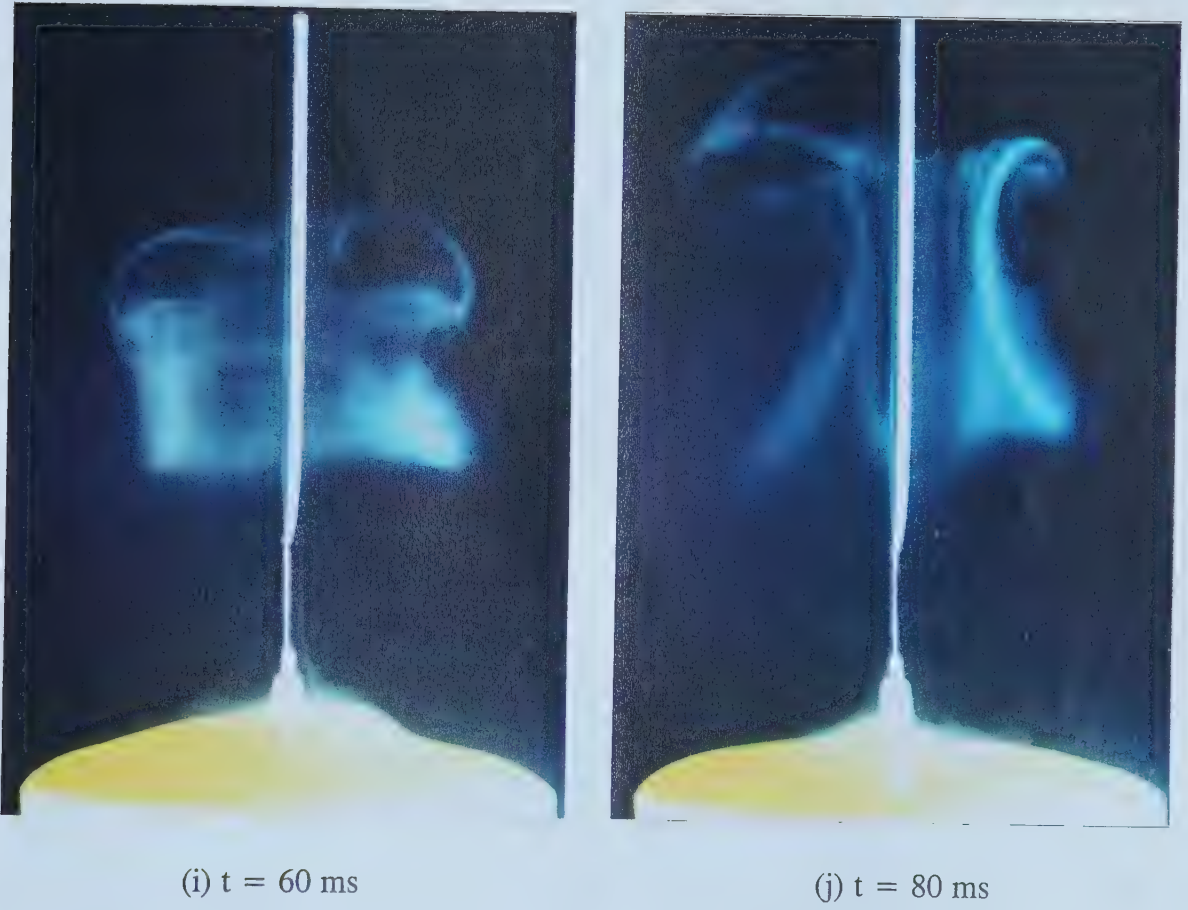


Figure 3.9: Evolution of the Vortex Structure Emerging from the Large Bubble (cont.)



(k) $t = 100$ ms

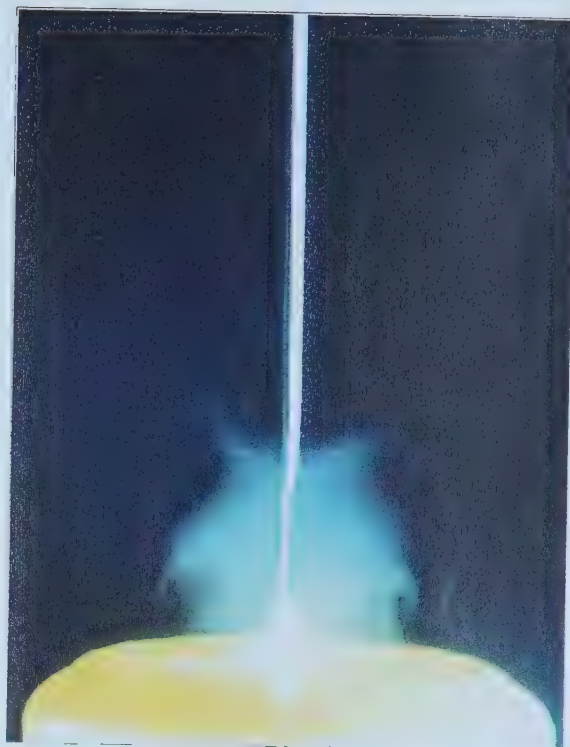


(l) $t = 150$ ms

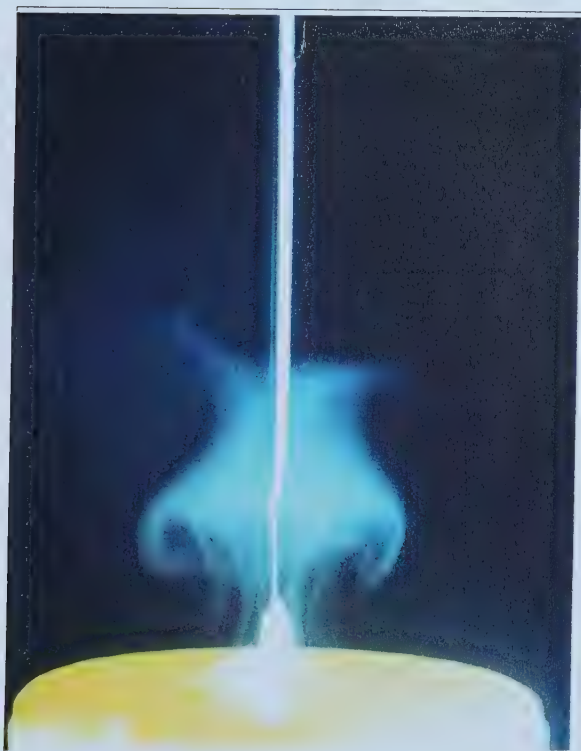
Figure 3.9: Evolution of the Vortex Structure Emerging from the Large Bubble (cont.)



(a) $t = 3 \text{ ms}$



(b) $t = 7 \text{ ms}$



(c) $t = 15 \text{ ms}$



(d) $t = 20 \text{ ms}$

Figure 3.10: Evolution of the Vortex Structure Emerging from the Small Bubble



(e) $t = 20$ ms



(f) $t = 30$ ms

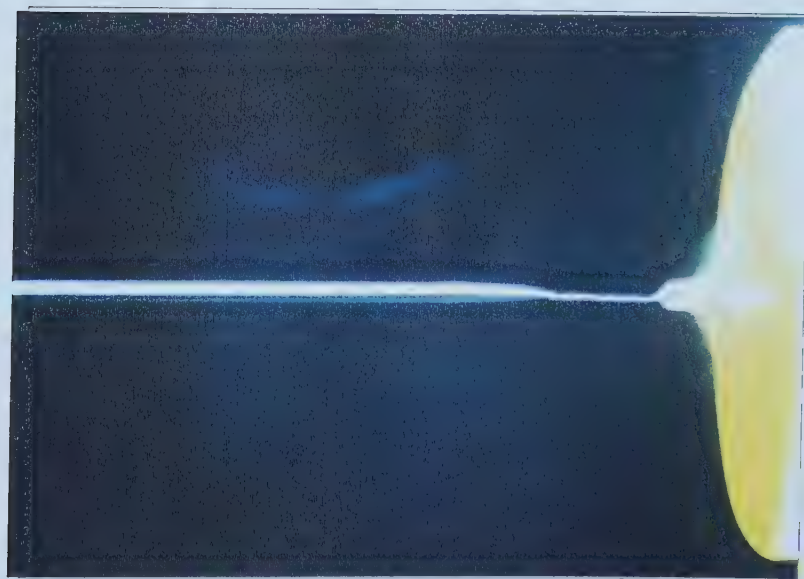


(g) $t = 45$ ms

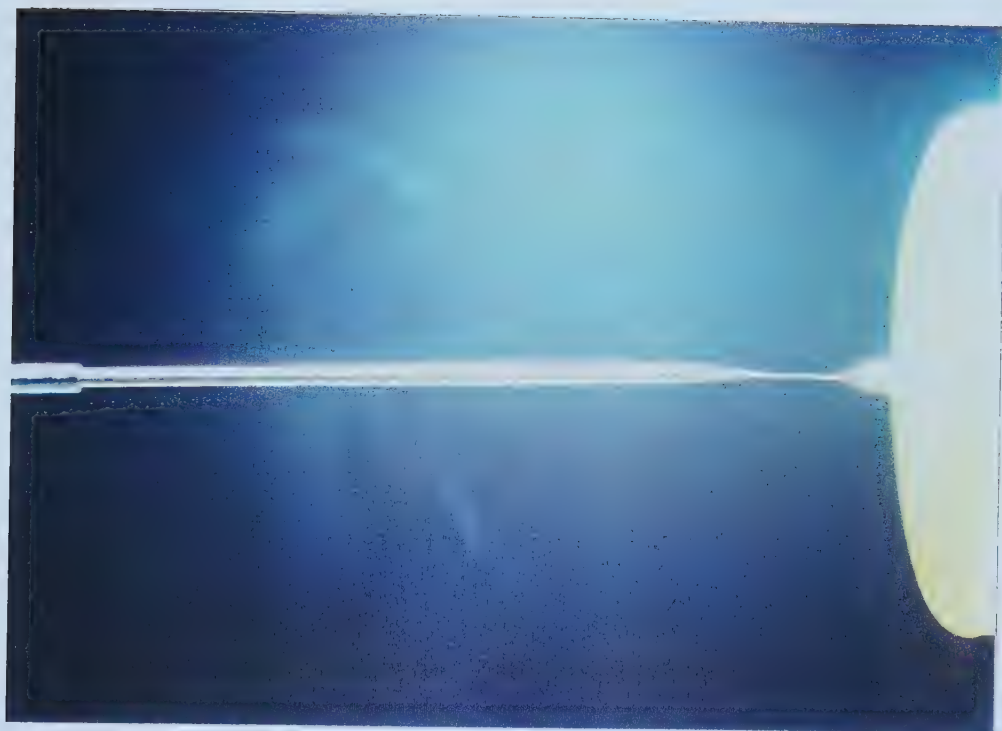


(h) $t = 60$ ms

Figure 3.10: Evolution of the Vortex Structure Emerging from the Small Bubble (cont.)

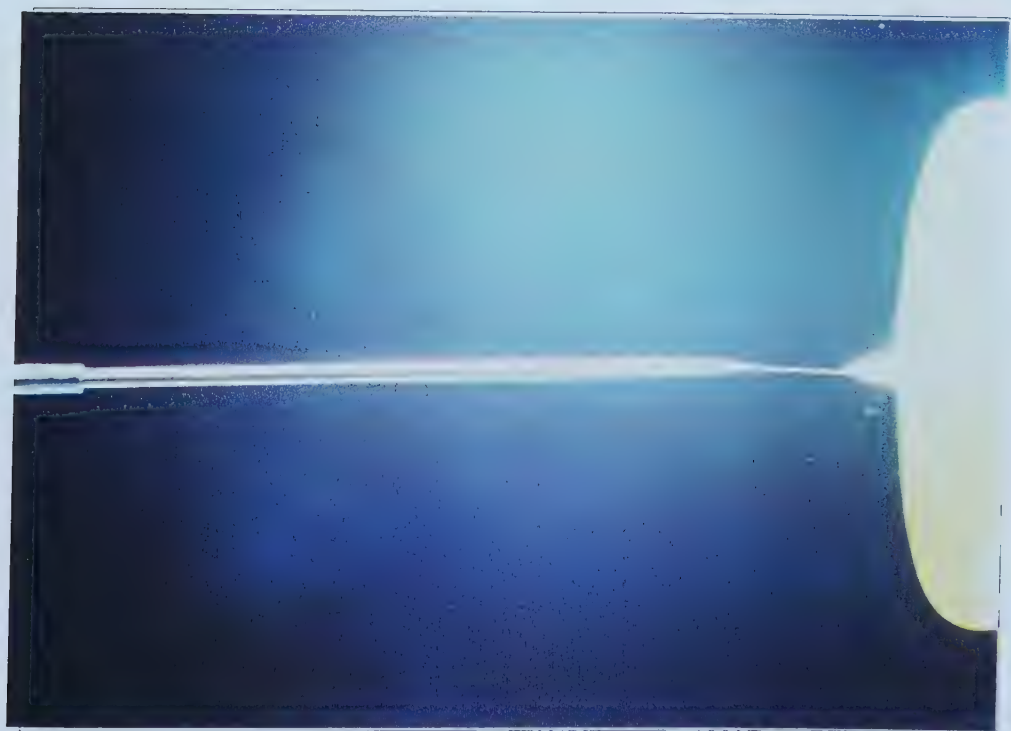


(i) $t = 80$ ms



(j) $t = 120$ ms

Figure 3.10: Evolution of the Vortex Structure Emerging from the Small Bubble (cont.)



(k) $t = 150$ ms



(l) $t = 150$ ms

Figure 3.10: Evolution of the Vortex Structure Emerging from the Small Bubble (cont.)

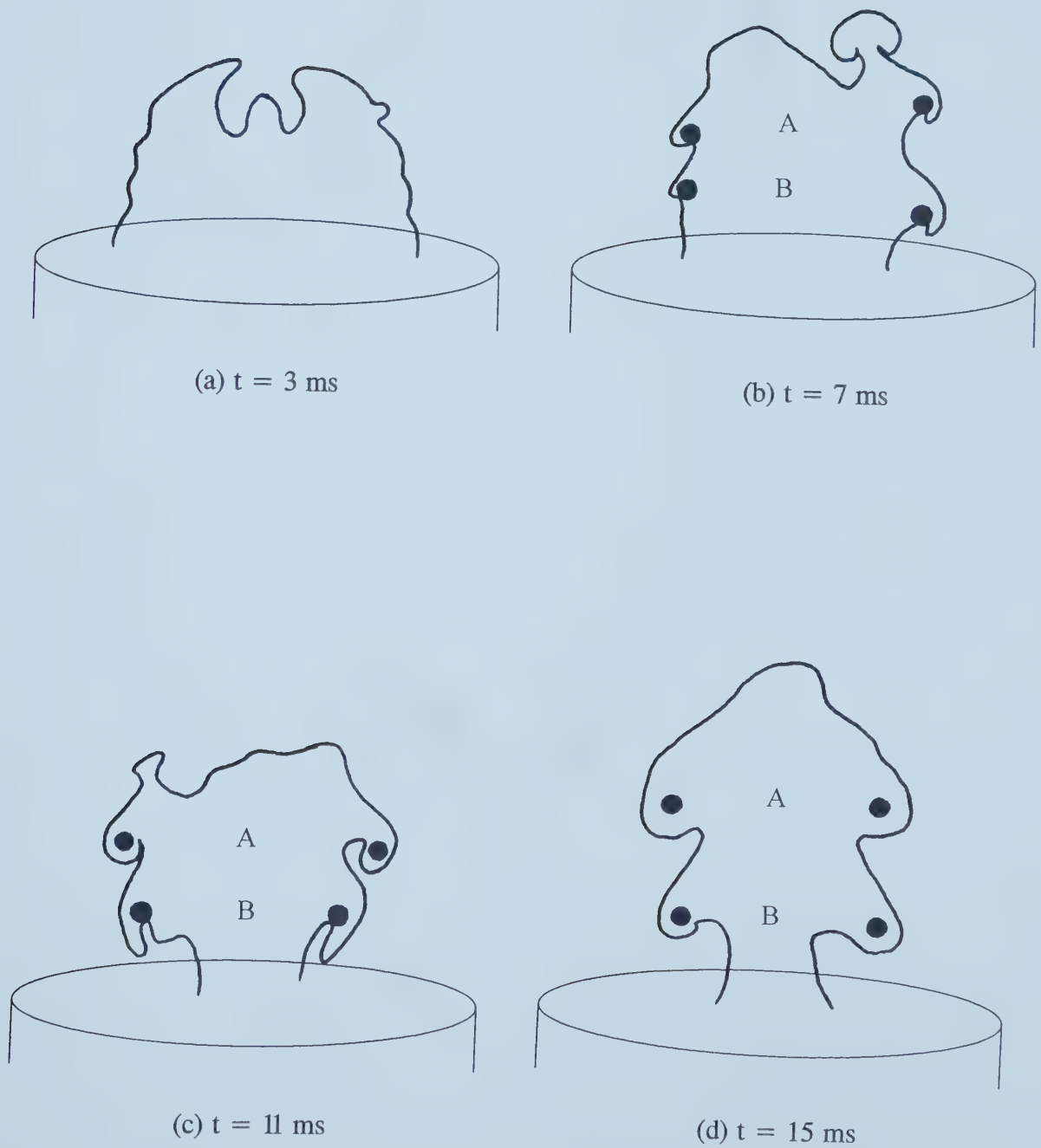


Figure 3.11: Vortex Evolution Model (early development)

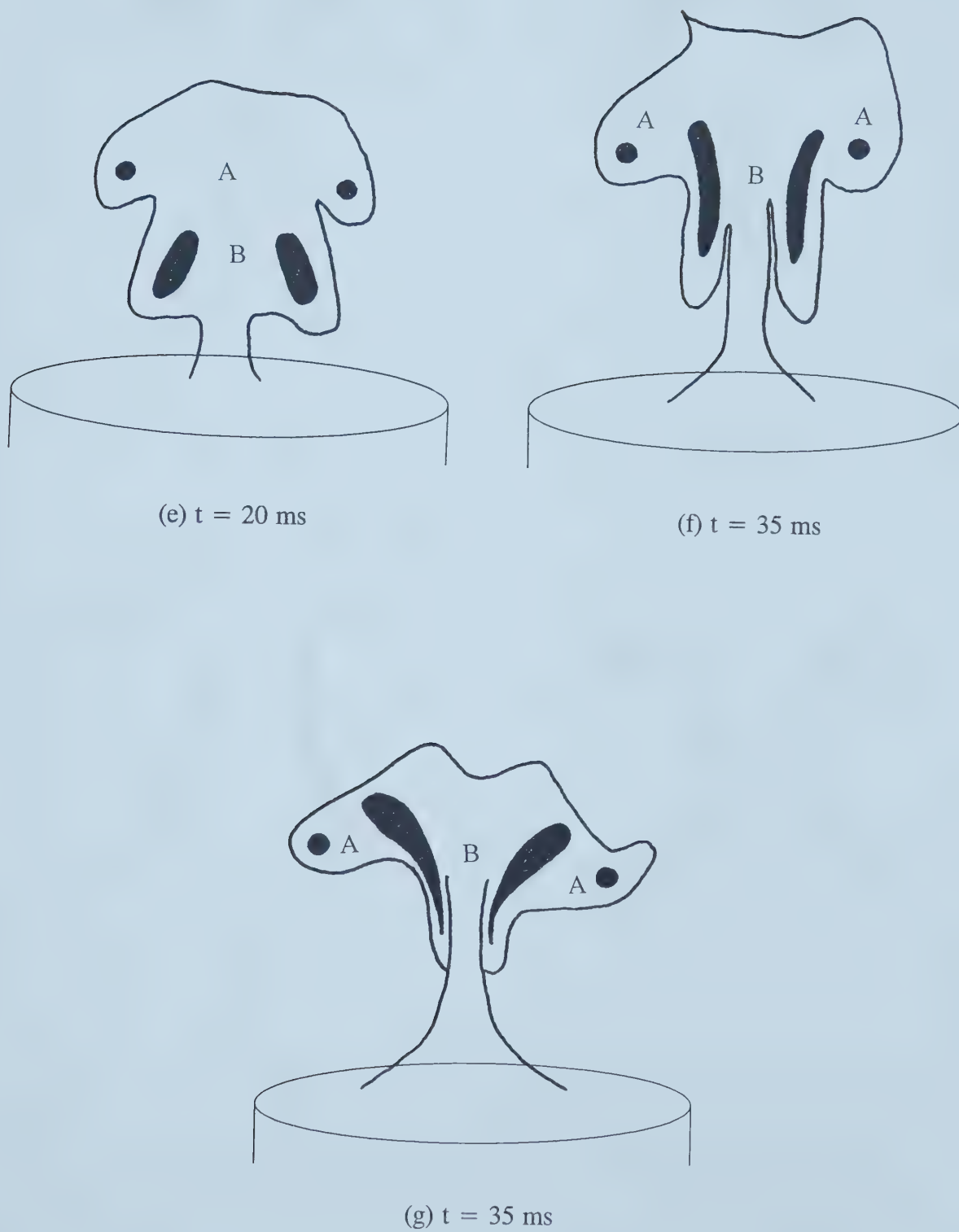


Figure 3.11: Vortex Evolution Model (early development, cont.)

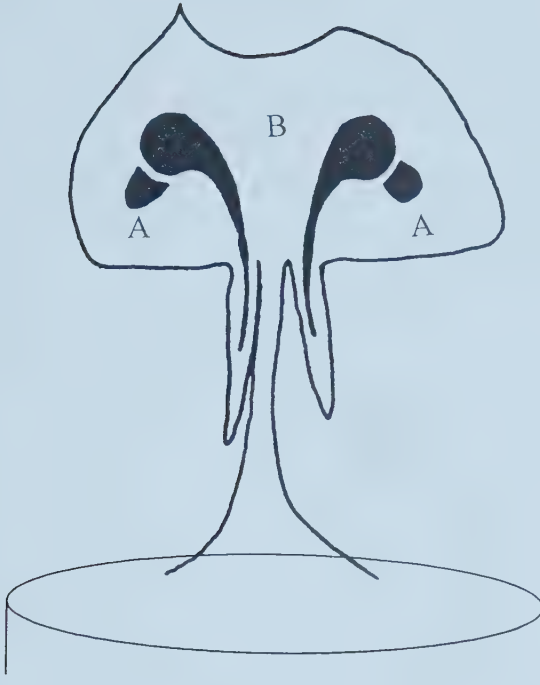
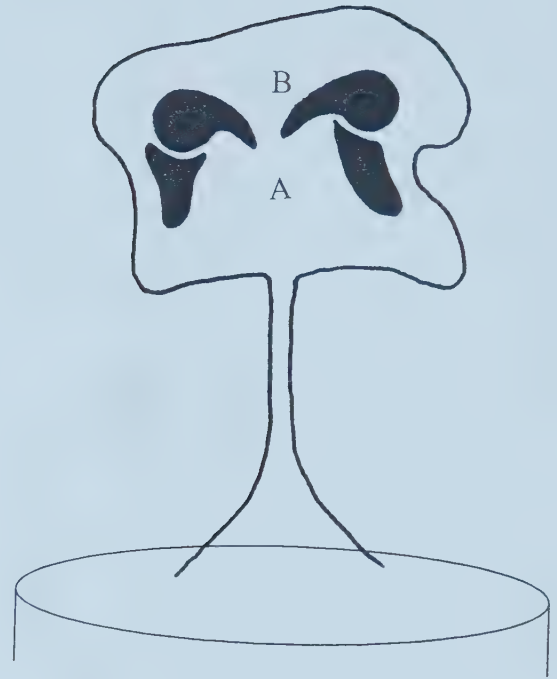
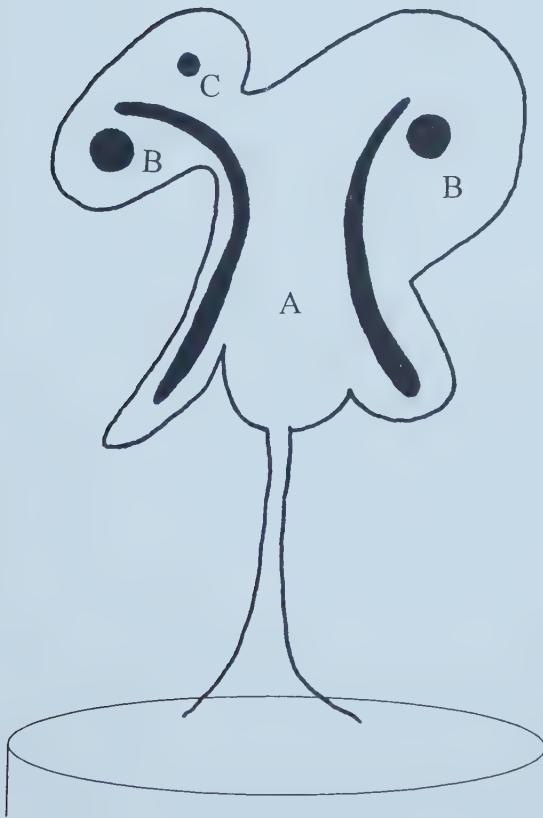
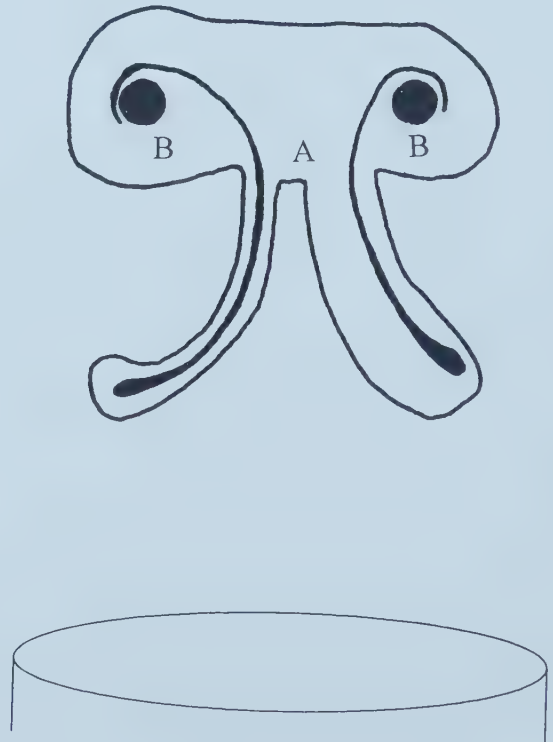
(a) $t = 45$ ms(b) $t = 60$ ms(c) $t = 80$ ms(d) $t = 100$ ms

Figure 3.12: Possible Lobe Generation Model (case 1, vortex A forms lobes)

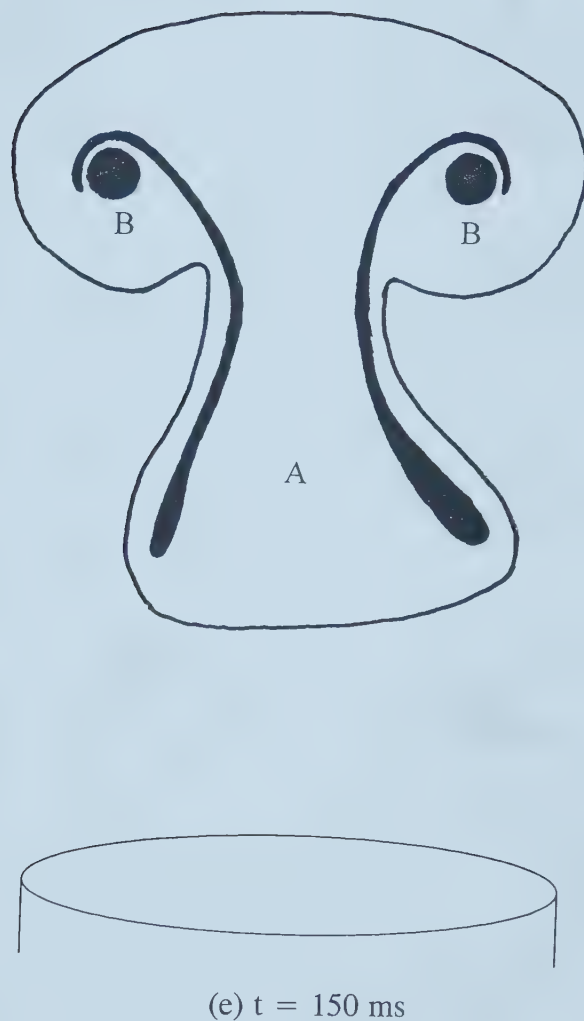


Figure 3.12: Possible Lobe Generation Model (case 1, vortex A forms lobes, cont.)

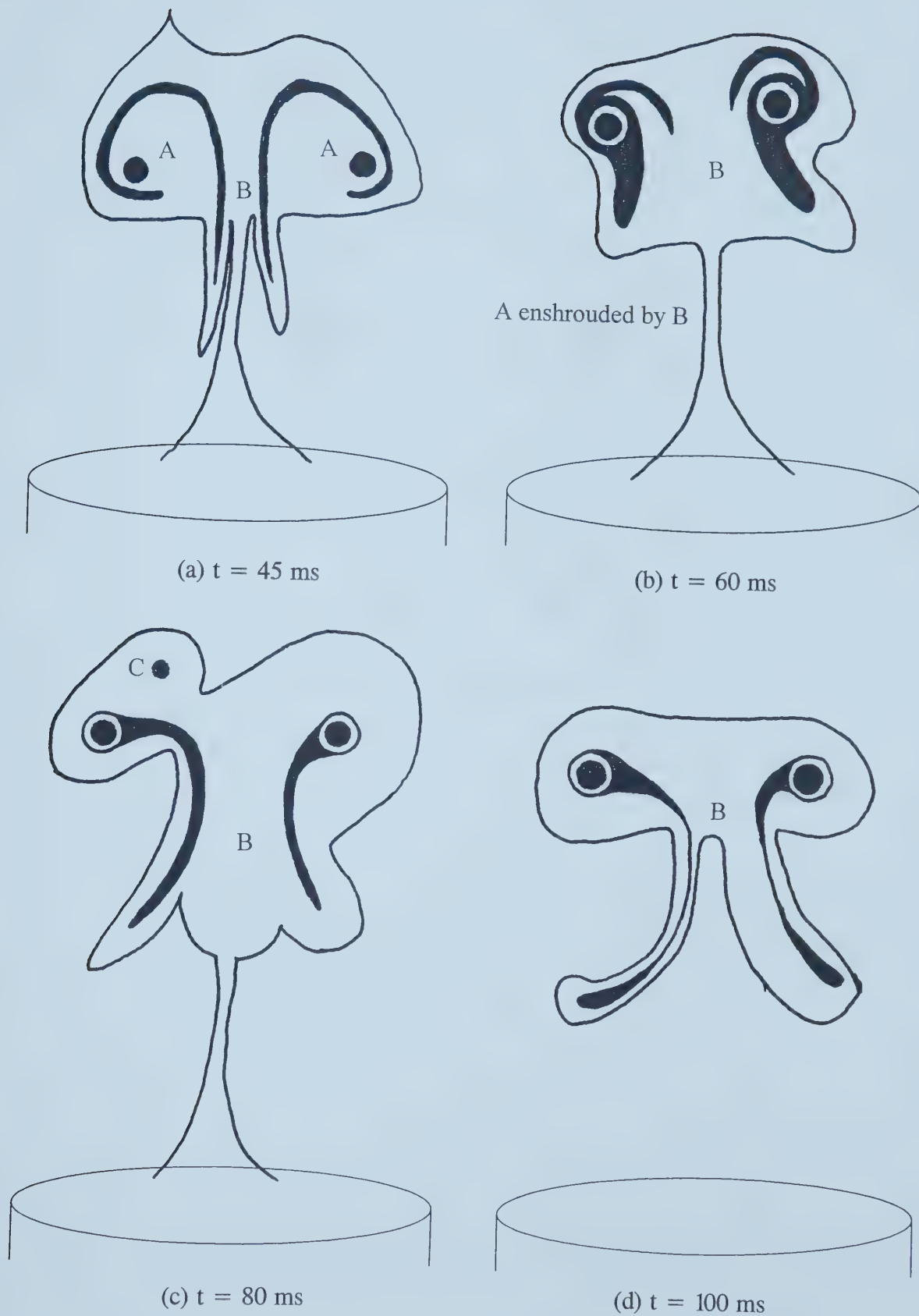
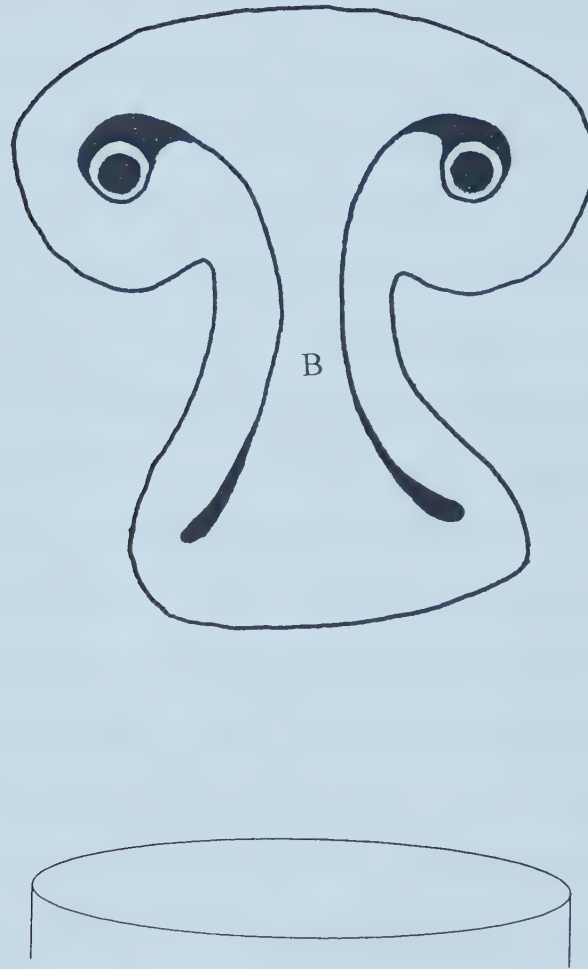


Figure 3.13: Possible Lobe Generation Model (case 2, vortex B forms lobes)



(e) $t = 150 \text{ ms}$

Figure 3.13: Possible Lobe Generation Model (case 2, vortex B forms lobes, cont.)

Figures 3.9(b) and 3.10(b) show aerosol formations at 7 ms. During the interval between 3 and 7 ms, much of the vorticity has organized itself into two approximately axisymmetric rings convecting upward. In Figure 3.10(b), a void like the one observed at 3 ms is still visible at the top of the cloud. At the top of the aerosol in Figure 3.9(b), a complex arrangement of vorticity remains. There is no attempt to model the complex top vortices at this time in the development, but at later times it appears to become more organized, and will then be briefly discussed. For this stage of development, the profile is modelled in Figure 3.11(b). The vortex core cross-sections are placed in their estimated locations. The leading ring is labelled A, and the other; B.

Figure 3.9(c) is taken at 11 ms. At this point in time, the structure begins to convect away from the liquid surface, and contract at the bottom, leaving behind a narrow wake, or stem, of aerosol which is visually similar to that photographed by Peck and Sigurdson (4). Following their notation for drop-generated vortex rings, we will sometimes use terms which are similar to those for a flower, of which the shape of the aerosol is reminiscent. The model of this photograph is given in Figure 3.11(c).

At 15 ms, two well-defined vortex rings are visible. These are shown in Figures 3.9(d) and 3.10(c) for the large and small bubbles, respectively. There is still additional vorticity present in both photographs. In Figure 3.9(d) it reveals itself in a bulge at the leading edge of the aerosol cloud. In Figure 3.10(c) one possible interpretation is that a small *daughter* ring is attached to the left side of the top ring. This daughter ring, faintly visible, is

most likely part of the complex arrangement of vorticity seen at earlier times near the top of the aerosol cloud. The structure and fate of this particular vorticity will be discussed at the end of this section. The overall structure is idealized in Figure 3.11(d). The main difference between this and Figure 3.11(c) is that the primary vorticity of the two rings has now become better organized, and the excess vorticity also appears to have contracted itself. The result is a more symmetric structure than at 7 ms or 11 ms.

By approximately 20 ms, the rings have begun to leapfrog². Figures 3.9(e), 3.10(d) and 3.10(e) show the vortices early in the leapfrogging process. In Figure 3.9(e) (from the large bubble), the trailing ring is becoming significantly sheared, whereas in Figure 3.10(d) (from the small bubble), it is still quite circular in cross-section. It is hypothesized that the lower ring of Figure 3.10(d), at a later time, will become more sheared, at which time it would look more like Figure 3.10(e). The early leapfrogging process is modelled in Figure 3.11(e). The bottom vortex is sheared from its initial circular shape, while the top vortex cross section remains more intact.

²Leapfrogging is an interaction which takes place between two vortex rings or vortex pairs whose paths are collinear, both travelling in the same direction, and one leading the other. The leapfrog is the action of the trailing pair or ring passing through the leading one, thus exchanging positions. To illustrate, consider two such vortex pairs consisting of point vortices. The velocity field induced by the trailing pair will cause the leading pair to separate, or become wider. The larger separation results in a decreased self-induced velocity of the leading pair, combined with the rearward component of the velocity field set up by the narrower trailing pair. In the same way, the vortices of the trailing pair will be convected together, and their velocity will increase. Since the shrinking trailing pair is moving more quickly than the leading expanding pair, the trailing pair passes through the leading pair, and becomes the new leading pair. In a similar manner, one vortex ring may pass through another vortex ring.

We will define *mid-leapfrogging* as the point at which the two rings are lying in approximately the same horizontal plane, one inside the other, as modelled in Figure 3.11(g). It is suggested that this is the vortex structure found within the characteristic shape of the aerosol shown in Figures 3.9(g) and 3.10(f). In these photographs, a small amount of fluid from vortex B is still trailing the cloud, visible as faint wisps of aerosol. This structure usually occurs at about 30 - 35 ms. At this time in the development, the locations of the vorticity cannot be visualized but are inferred from earlier time photographs and the expected trajectories of the vortices, from knowledge of the Biot-Savart Law of vortex-induced velocities. Figure 3.9(f) shows a similar structure with a significant portion of the lower vortex still trailing and the leading vortex (vortex A) still easily identified on the perimeter of the structure. It is possible that in some cases, the bottom ring is not entirely entrained by the top one, and that the portions left behind may form some of the lobes visible at later times. However, it is known that this is not the primary mechanism of lobe formation since several photos (such as Figures 3.9(f) and 3.10(f)) show this trailing aerosol almost completely entrained. Also, the clouds photographed in Figures 3.9(g) and 3.10(f) contain a dark region within the white aerosol, indicating that a significant mass of clear air has been entrained at some point. This air had to be entrained during the leapfrog process, and was either contained in the middle of the lower ring, or was drawn in through the gap between the two rings as they approached each other.

During and after the leapfrog, the precise location of the vorticity is difficult to determine. It is not known how much the cross-sections of the vortices have become distorted through shearing and what three-dimensional perturbations are beginning to appear on the rings. Figures 3.9(h) and 3.10(g) contain photographs of the structures at 45 ms. The dark region of entrained aerosol-free air is much larger now than during leapfrogging, and the cloud is now vertically thicker and becoming square in the side view. This thickening of the cloud would suggest that the vortex rings are gaining vertical separation from each other after the leapfrog. Two possibilities for the structure of the vorticity in these photos are represented in Figures 3.12(a) and 3.13(a). Figure 3.12(a) suggests that at this time, vortex B is not sufficiently sheared to destroy the topology of the leapfrogging rings. Figure 3.13(a) shows considerable shearing of vortex B such that the rings are no longer leapfrogging, but that B is beginning to enshroud A. Extrapolated outcomes of these possible scenarios will be discussed in paragraphs following.

By 60 ms, lobes, or *petals*, are beginning to form beneath the cloud, as shown in Figures 3.9(i) and 3.10(h). We will now suspend our discussion of the vortex evolution in order to consider the possible origins of these lobes. The composition and formation of the lobes is described by one of the four following possibilities:

1. The lobes are primarily made up of portions of the initially leading vortex ring (A) which convect out of the cloud and are no longer bound by the *trapped orbits* of the velocity field induced by the vortex ring

consisting of B and the remaining part of A. Consequently, they are left behind as the main ring convects away. This consequence would follow from Figure 3.12(a).

2. The lobes are primarily made up of portions of the initially trailing vortex ring (B) which escape the trapped region. This consequence would follow from Figure 3.13(a).
3. The two rings become combined, or *merge*, and portions of either ring are convected beyond the trapped region to form the lobes.
4. The lobes consist only of irrotational, aerosol-marked fluid.

Before discussing these alternatives, it should be noted that there is possibly a significant difference between the mechanism of vorticity deformation during early- and mid-leapfrogging, and that during lobe generation. Before lobe generation, it is thought that vorticity deformation was primarily through shearing in the plane of the images (ie. parallel to the page), or normal to the vortex lines³. However, during lobe generation, it is expected that if the lobes contain vorticity the convection of the vorticity may also consist of considerable tilting and stretching of vortex lines. This is because at later times the shed aerosol sometimes resembles hairpin vortices as were

³A *vortex line* is defined as a curve everywhere tangential to the vorticity (analogous to a streamline in a velocity field). A vortex ring with a finite cross-sectional dimension, as we have, may be represented by a bundle of closed circular vortex lines. The surface enclosing this bundle of vortex lines would be a toroid, and is referred to as a *vortex tube*. The distortion of the cross-section of this toroid is what we describe as shearing, and does not necessarily imply that the vortex lines are changing shape. The deformation of individual vortex lines is described as *tilting* and *stretching*.

previously observed by Peck and Sigurdson in the case of the impacting drop (4), and by Sigurdson (6) in the case of the bomb-generated cloud. Therefore in Figures 3.12 and 3.13, we are not necessarily viewing the vorticity cross-section, as a significant portion of it is likely in the streamwise direction.

Alternative 1 is modelled in the sequence shown in Figure 3.12. Under the assumption of limited cross-sectional shearing or merging of the vortices, an argument can be made by considering the Biot-Savart Law of Vortex-induced velocities. The displacements of the vortices between Figures 3.9(g) and 3.9(h) should be approximately equal in magnitude as the displacements between Figures 3.9(e) and 3.9(g) since the two time intervals are similar (10 ms and 15 ms). This would imply that at the time of lobe generation (60 ms); photographed in Figure 3.9(i), and modeled in Figure 3.12(b), the initially leading ring (A) could be in a position to form the lobes. However, some doubt is cast on the assumption of limited shearing as Figure 3.9(f) shows a severely sheared portion of aerosol trailing the main mass during leapfrogging. Despite this uncertainty, it will be shown in Section 3.4 that the two-dimensional computed results support this alternative.

Alternative 2 assumes that vortex B is significantly sheared, which the photographs seem to indicate, but A remains intact. It is then possible that the lobes are formed by vortex B, the initially trailing ring. This alternative sequence is modelled in Figure 3.13. The idea here is that perhaps just before or while the lobes are generated, ring A becomes enshrouded in the severely sheared vortex B. Since B is external to A, it is most likely to escape the

ring. The merging process may not be as simple as suggested in the figure.

If both rings become combined, alternative 3, portions of either ring may escape to form the lobes. It is possible that the lobes may be generated by a mechanism similar to that discovered for drop-formed vortex rings by Peck and Sigurdson (4) in which case there was initially only one vortex ring, although there is probably not enough time for the identical process to occur. Due to our limited ability to see the structure of the vortex cores during lobe generation, it is difficult to determine if it is this alternative or alternatives 1 and 2 at this point.

Alternative 4 suggests that the lobes do not contain vorticity, and are therefore generated by externally-induced velocities alone. Shariff and Leonard (5) caution that loops of dye in the wake of vortex rings have been mistakenly interpreted as hairpin vortices, but may simply be irrotational dye movements which can be accounted for by unsteadiness in the vortex ring core. Conversely, Peck and Sigurdson (4) have proven that the petals of the drop-formed vortex rings contain vorticity because they have observed the ends of petals separating into small vortex rings.

For reasons which will be explained later in this section, and in Section 3.5, it is determined that in at least some cases, the lobes are rotational, and it is suggested that this is generally the case, so that alternative 4 is improbable. The remaining alternatives are that the lobes consist of primarily vortex A, primarily vortex B, or a combination of the two. If the lobes are formed primarily of vortex A, then it is possible that portions of A could become

wrapped around vortex B by tilting and stretching, as illustrated in Figure 3.12. It is then probable that vortex B would also deform somewhat as well. If vortex B enshrouds A through shearing and/or tilting and stretching, and forms the lobes, the structure may be idealized by Figure 3.13. Here, the two vortices are shown separate at all times, but it is unlikely that this order would be maintained in such a delicate configuration. Merging of the vortices would likely occur. If the two vortices merge, and the lobes consist of both vortices (alternative 3), the structure may be represented by a hybrid of Figures 3.12 and 3.13 except that the vortex ring core would consist of A and B, with portions of either A or B extending from the core at different azimuthal positions.

Based on the information presented to this point, the composition and method of formation of the lobes is inconclusive. However, additional clues will be revealed from observation of lobe behaviour as we continue to discuss the vortex evolution, and some insight will also be provided when we discuss the computed results.

After the lobes are generated, the main ring convects away from the lobes, elongating them in the process. Photographs of the vortex rings after lobe generation are shown in Figures 3.9(j) through 3.9(l) for the large bubbles, and in Figures 3.10(i) through 3.10(l) for the small bubbles. For the large bubbles, the lobes appear to be similar to one another in size and shape, although the structure has only been visualized in one view, and therefore their three-dimensional structure cannot be fully known. The vortex ring also

becomes symmetrical and the cross-section of the vortex exhibits the spiral pattern characteristic of vortex rings, suggesting that it will now remain axisymmetric. However, in the small bubbles, asymmetry is common in the vortex ring and lobes. Perhaps for these distorted structures, a stable, symmetric configuration is formed at a later time.

Unfortunately, by the time the lobes are fully formed, the aerosol becomes very dilute, and it is therefore a challenge to visualize the structure. Furthermore, some of the photographs have been overexposed, further reducing the contrast between the aerosol and the background. In spite of these difficulties, some important information may still be gleaned. Some of the lobes of Figures 3.10(j) and 3.10(l) have tips which are significantly curled, and have convected radially away from the centreline of the main ring. Such gross distortions indicate the presence of vorticity in the tip of the lobe. The lobe tips in Figures 3.9(k) and 3.9(l) also appear to be curved to a lesser extent. These observations indicate that vorticity is present in the lobes. It still remains to be explained where it comes from, and what its structure is.

Finally, the structure of the excess vorticity is discussed. It has been mentioned that at early times, the structure of the excess vorticity is very disorganized and complicated. However, it appears that at later times (greater than 20 ms), there remains a much simpler structure, which may be seen in Figures 3.10(e) or 3.9(j). In each of these photographs, the structure looks like a small *daughter* vortex ring which is travelling upward and to the left, and appears to be joined to the top, left side of a main ring of vorticity. For

Figure 3.9(j) this is modelled as vortex C in figure 3.12(c). The other side of the ring is assumed to be connected to the main ring, and is not shown. It is expected that rings such as C may eventually convect out of the trapped orbits of the vortex ring and be left behind, allowing the ring to take on the symmetrical form photographed at later times.

3.3.2.2 Drop Entrainment by Vortex Rings

Figures 3.9(i) through 3.9(l), 3.10(k), and 3.10(l) show the entrainment of bubble film drops into the vortex ring. Day (2) was able to infer the existence of a vortex ring using these drops as a crude flow visualization medium.

3.3.2.3 Displacements, Velocities and Sizes

Figure 3.14 contains a plot of the leading edge displacement of the aerosol clouds for times up to 80 ms. All of the data on this graph was obtained on the same day, and therefore is expected to be under similar ambient conditions. From measurements of ambient temperature, pressure, and relative humidity the greatest variations of these properties within a day were 1.5 °C, 1.5 kPa, and 6%, respectively. The points plotted represent the mean leading edge displacement for each bubble size, at each time, and the bars represent the variation in displacement for the sample collected at each time. Each sample contains between 2 and 4 points. The mean points are connected by straight lines. The displacement of the large structure at 3 ms is greater than the displacement of the small structure, and generally remains equal to or greater

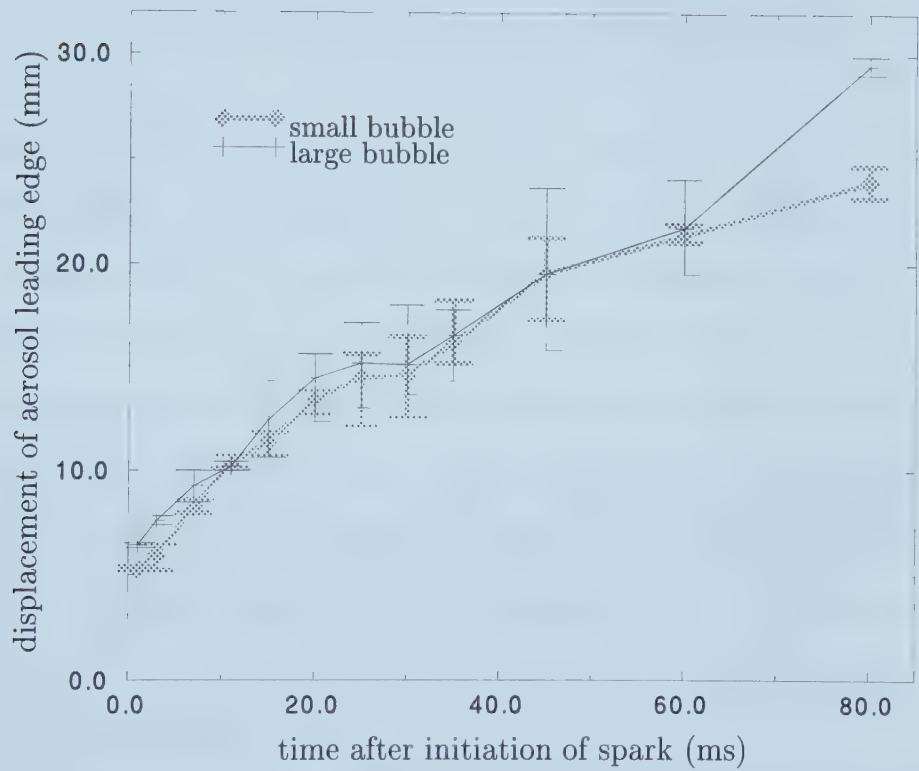


Figure 3.14: Vortex ring leading edge displacement.

Table 3.6: Vortex Ring Leading Edge Velocities Derived from Triple Exposure Photographs (large bubbles)

Bubble	t_1 (ms)	t_2 (ms)	t_3 (ms)	y_1 (mm)	y_2 (mm)	y_3 (mm)	\bar{U}_{a1} (m/s)	\bar{U}_{a2} (m/s)
i	3	33	63	7.2*	12.2	20.9	0.17*	0.29
ii	3	33	63	6.3	14.1*	21.4	0.26*	0.25*
iii	3	33	63	6.4	14.0	21.6	0.25	0.25
iv	70	100	130	20.0	24.5	28.9	0.15	0.15
v	70	100	130	21.2	25.7	31.1	0.15	0.18

than that of the small structure. Noting the variations of the displacements two remarkable observations may be made. First, despite the large variations, the shapes of the two graphs plotted by the mean displacements are very similar in shape and magnitude (with the exception of the point at 80 ms). Secondly, for each bubble size, the variations in the middle time range (15 ms to 60 ms for the large bubbles, and 25 ms to 45 ms for the small bubbles) are relatively large compared to those at early times, but exhibit small variations again at 80 ms. In other words, the displacement of the leading edge at 80 ms could be predicted with much greater accuracy than the displacement during the middle time range.

Tables 3.6 and 3.7 contain leading edge displacements and average velocities extracted from triple exposure photographs of the vortex structure, such as those shown in Figure 3.15. The asterisks represent measurements which had to be estimated based on the fraction of the structure that was easily visible. An example of such an estimation is the bottom exposure of Figure 3.15(a), which is tabulated as bubble *i* in Table 3.6. In both of the



(a) $t = 3, 33, \text{ and } 63 \text{ ms}$



(b) $t = 70, 100, \text{ and } 130 \text{ ms}$

Figure 3.15: Triple Exposure Photographs of the Vortex Structure (large bubble)

Table 3.7: Vortex Ring Leading Edge Velocities Derived from Triple Exposure Photographs (small bubbles)

Bubble	t_1 (ms)	t_2 (ms)	t_3 (ms)	y_1 (mm)	y_2 (mm)	y_3 (mm)	\bar{U}_{a1} (m/s)	\bar{U}_{a2} (m/s)
vi	3	33	63	6.5	14.8	25.8*	0.28	0.37*
vii	3	33	63	5.3	16.5	28.0*	0.37	0.38*
viii	3	33	63	6.4	15.2	24.1*	0.29	0.30*
ix	70	100	130	22.1	26.8	31.5	0.16	0.16

mentioned tables, the measured displacements, y_1 , y_2 , y_3 , are measured from images taken at the corresponding times, t_1 , t_2 , t_3 . The velocity $\bar{U}_{a1} = \frac{y_2 - y_1}{t_2 - t_1}$, and $\bar{U}_{a2} = \frac{y_3 - y_2}{t_3 - t_2}$. From a perusal of the last two columns of Tables 3.6 and 3.7, the velocities between 70 and 130 ms appear to be quite consistent between the two time intervals in this range, and between the two bubble sizes. However, between 3 and 63 ms, there exists more inconsistency in velocity measurements taken during the same time interval, and between the two intervals for a given bubble. Despite the variation, the small bubbles generally exhibit a higher velocity between 3 and 63 ms, than do the large bubbles. However, these generalizations will require additional data (ie. a larger sample size) for verification.

From photographs of the vortex rings at later times, the core locations of the vortex ring were estimated. For the large bubbles, it was found that at 150 ms, the core ring diameter varied between 16 and 18 mm, and between 100 and 130 ms, the ring diameter varied between 14 and 17 mm. In comparing the 8 different vortex rings falling in this range, a monotonic relationship did not exist between diameter and time. For the small bubbles, the range

of diameters also varied between 14 and 17 mm for the 100 to 130 ms time range; and a couple of rings at 150 ms were measured to be approximately 16 mm in ring diameter.

Based on the average velocity of the aerosol leading edge, \bar{U}_a , and the ring diameter D (between the cores), of the vortex rings, and a typical value for the kinematic viscosity of air at 20°C and 1 atmosphere, $\nu = 0.15 \text{ cm}^2/\text{s}$, the Reynolds number of the vortex ring may be calculated. The Reynolds number is given by:

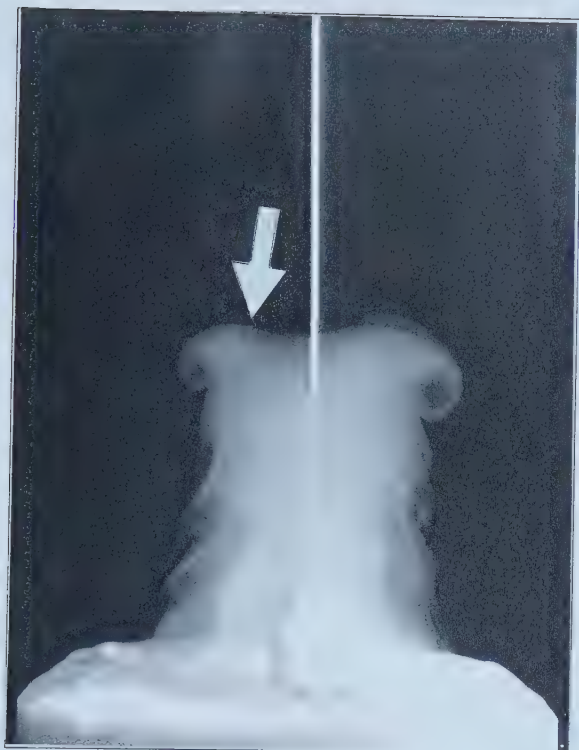
$$Re_D = \frac{\bar{U}_a D}{\nu} \quad (3.2)$$

At approximately 100 to 130 ms, the large and small vortex rings have similar velocities and sizes. If we take a representative $D = 16 \text{ mm}$, and $\bar{U}_a = 0.16 \text{ m/s}$, the resulting Reynolds number is 1.7×10^2 .

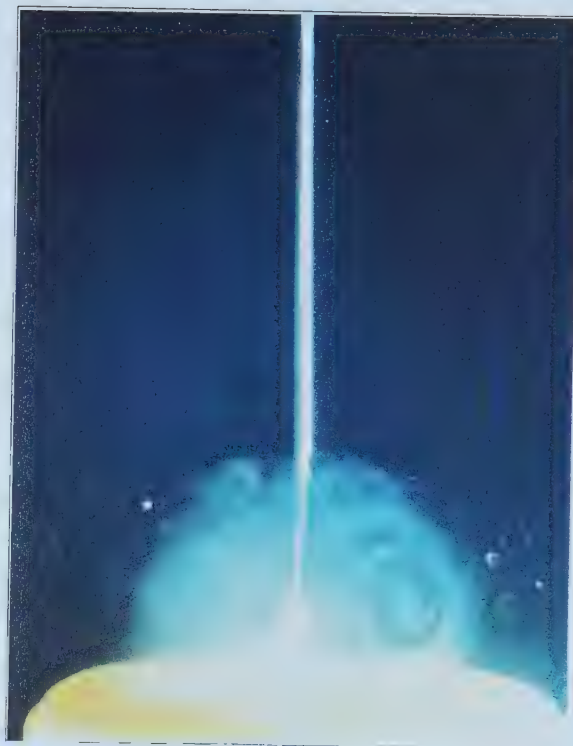
3.3.2.4 Vortex Rings with Smoke Tracer

Figure 3.16 contains samples of the preliminary data obtained with the original apparatus, using smoke to visualize the vortex ring. From the limited data obtained, it appears as though the evolution sequence of these vortex rings may be different than the evolution of the bubbles containing aerosol.

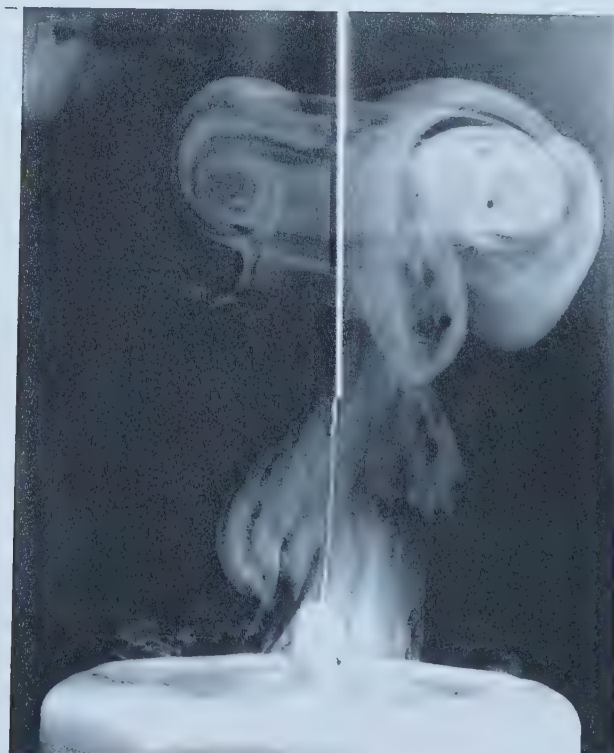
Figures 3.16(a) through 3.16(c) are three photographs which represent a possible sequence of structures in the vortex development. In Figure 3.16(a), the smoke resembles the structure created by the aerosol-filled bubbles of Figures 3.9(b) and 3.10(b). The similarities are the cylindrical shape, and



(a) initial shear layer



(b) resembles a vortex ring



(c) complex three-dimensional structure

Figure 3.16: Preliminary Photographic Data with Smoke Tracer



(d) vortex ring with *daughter* ring



(e) vortex ring with *daughter* ring



(f) vortex structure at $t = 30$ ms and $t = 60$ ms

Figure 3.16: Preliminary Photographic Data with Smoke Tracer (cont.)

the vortices visible on the sides of the cloud. In addition, a void of smoke is again present near the top of the structure. The top vortex is larger than the following ones, and a small eddy is seen near the left vortex (shown by the arrow), which appears to be of the opposite sign, or direction of rotation to the left vortex (when considering only the cross-section). This eddy may be the left side of a downward-moving vortex ring concentric to the outer ring. Such an internal ring could generate the smoke void by entraining clear air from above. This may also be the cause of the aerosol void visible in Figures 3.9(a), 3.10(a), and 3.10(b) although there are no eddies visible to reveal its location. Since the eddy in Figure 3.16(a) is only on one side of the structure, it may rather be part of a small, upward-moving vortex ring which is attached to the larger ring in a similar manner to the model of Figure 3.12(c).

Figure 3.16(b) contains a structure which was never observed in the evolution of the aerosol-filled vortex rings, and suggests significant differences in the evolution sequences of the two experiments. Here it appears that one large vortex ring has formed without any large-scale leapfrogging. It would be impossible for a leapfrog to have occurred with the vortex ring still located at the liquid surface.

Figure 3.16(c) has a three-dimensional structure reminiscent of the late-time structures formed by the small bubbles in Figures 3.10(j) through 3.10(l). The bubble size of the smoke structure is not available for comparison.

Figures 3.16(d) and 3.16(e) have more symmetrical vortex rings with a

smooth spiral cross-section, again testifying to the absence of a leapfrog. Also note the rapid rate at which the structure forms - these two photographs are taken at approximately 27 ms. Several of the smoke rings photographed are seen travelling in the wake of a clearly visible daughter vortex ring, which is completely detached from the main ring. In the aerosol photographs, daughter rings are usually attached to a larger vortex ring, and are not as easily visualized due to the translucence of the aerosol which tracks them.

Figure 3.16(f) is a double exposure at 30 ms and 60 ms after the spark. Since the vortex cores are easily identified here, their vertical displacement was measured during the 30 ms time interval between the exposures, and it was determined that the cores are travelling with a velocity of 0.35 m/s. This is approximately in agreement with small aerosol bubble velocities measured between 33 and 63 ms, as shown in Table 3.7.

Unfortunately, since the photographs of the smoke-tracer vortex rings were taken with the preliminary apparatus, most of them do not have bubble size information associated. However, Figures 3.16(d) and 3.16(e) contain images of the originating bubbles, which are of different sizes, Figure 3.16(e) being larger than the small aerosol bubble but smaller than the large aerosol bubble. The structures in these photographs are topologically similar, and therefore it is unlikely that the structural differences between the smoke- and aerosol-marked vortex rings are a result of bubble size. Known experimental parameters which may cause the different evolution sequences are altered surface tension caused by surface active smoke in the bubble, and buoyancy

in the vortex ring if the temperature of the smoke is greater than that of the ambient air.

3.3.3 Passive Bursting

Some experiments were conducted in which large bubbles were allowed to burst passively, while being recorded on VHS format video. This allowed an image of the ring to be obtained at approximately 33.3 ms intervals with the first image of the ring recorded at an unknown time between 0 and 33.3 ms after the bubble had begun to burst. A modified bubble solution was used (375 mL distilled water, 0.4 mL SunlightTM, 2.0 mL glycerine, and 300 mg fluorescein) in order to reduce the time required to burst, and thereby improve aerosol visibility. Despite this improvement, only one out of the five tested bubbles burst sufficiently quickly to produce a useful sequence of video frames.

The resolution of the video camera is far inferior to that of the photographs, and it is therefore difficult to visualize structure in the aerosol for some of the 6 frames recorded. However, it is concluded that a vortex ring is eventually formed by 100 ms as the cross sections of the cores are visible as intense regions convecting upward. In addition, on the frame recorded between 67 and 100 ms, at least 2 lobes are seen emerging from the ring, the bases of which appear to remain approximately stationary as the ring is traced convecting away for another 100 ms. To the extent that we are able to visualize the phenomenon on video, there is no evidence to suggest

any difference between the structure of the vortex generated by the passively bursting bubble, and that of the spark-burst bubbles. Since the resolution of the video is poor, this does not mean that the structures of passive and spark-burst bubbles are the same at all levels of detail.

3.4 The Computational Model

To aid in understanding the vortex kinematics which occur during the creation of the vortex ring, as described in Section 3.3.2.1, two two-dimensional point vortex models have been generated. These models are derived from a code modelling a two-dimensional transversely-forced jet, which was generously provided to us by Dr. W.T. Ashurst at Sandia National Laboratories, in Livermore, California. The vortex core models and numerical methods from this code have been retained, while the positions of the vortices have been changed to reflect the possible initial vorticity conditions of the current experiment. The output of the models is used to form a movie on the computer monitor. A detailed description of the equations and numerical methods used, is given in Appendix A.

For clarity in the meaning of the variables, dimensions of centimeters (cm) and seconds (s) are given to variables of length and time, respectively. However, because this is a two-dimensional model, and because the magnitudes of the variables do not necessarily reflect the experiment, these dimensions have no direct relation to those of the experiment. The equations have not been non-dimensionalized. Since the strength of the vorticity created by the

experiment is not known, the strength of the vortices in the model have been arbitrarily determined based on some parameters remaining from the original jet code. It is expected that the qualitative structure is unaffected by the magnitudes of these parameters, only the time-scale will be affected. Since the structure is what we are interested in for now, this is of no consequence.

The models each consist of 60 point vortices arranged uniformly along the perimeter of a semi-circle of radius $R_c = 0.5cm$, centred on the origin. The semicircle exists in the two quadrants where x is positive, and the positive x -axis points in the upward direction (thus, the orientation of the model is the same as the experiment). The vortices on the right side rotate in the clockwise direction, and are referred to as of negative sign, and the vortices on the left rotate counterclockwise and are positive. Image vortices of equal strength to the *real* vortices were created in the two lower quadrants. To simulate the aerosol in the physical bubble, particles lacking inertia were initially placed within the semicircle, and were allowed to convect at the local velocity induced by the vortices. A schematic diagram of the initial conditions is shown in Figure 3.17.

The difference between the two models is that in the first model, the vortices all have the same circulation, whereas in the second model, the top two (left and right) vortices have this circulation, but adjacent vortices have a circulation which is decreasing linearly along the perimeter of the semicircle, and ultimately reaching a circulation of zero at the base ($x = 0$, $y = +/- 0.5$). The image vortices also exhibit this decay in the second model. The

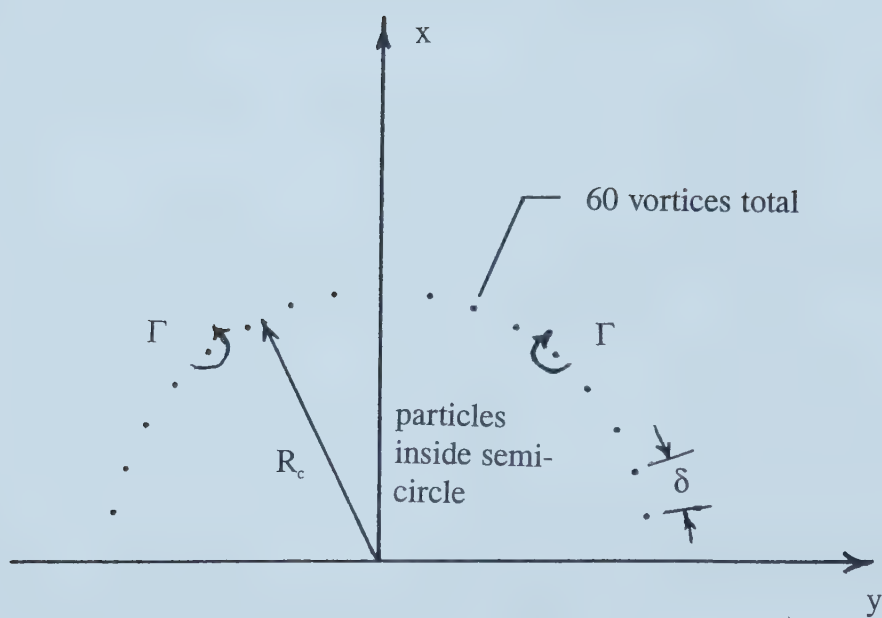


Figure 3.17: Initial Conditions of the Computational Model

purpose for forming these two models is to test two possible initial vorticity conditions. The uniform circulation model is the simplest; however, since the film rim velocity and bubble pressure would be the highest at earlier times when the rim was still at higher latitudes on the bubble, it is speculated that more vorticity may also be generated at the higher latitudes.

The magnitude of the vortex circulations, for the uniform model, or the maximum circulation, for the varying model, is given by:

$$\Gamma = \frac{R_c}{120} cm^2/s. \quad (3.3)$$

The arc length separating the vortices is defined by the number of them since they are equally spaced, and its magnitude is given as:

$$\delta = \frac{\pi}{60} R_c = \frac{\pi}{120} cm. \quad (3.4)$$

The time step, dt , at which new vortex and particle locations are calculated, is equal in magnitude to the initial vortex spacing, δ .

$$dt = \frac{\pi}{120} s \quad (3.5)$$

For each movie frame generated, the time is incremented by dt . Therefore, frame 1 is at a time of $\frac{\pi}{120}s$, frame 2 is at a time of $\frac{\pi}{60}s$, and so on.

3.5 Computed Results and Discussion

Figures 3.19 and 3.20 contain graphical output of the two computational models respectively, showing the locations of the point vortices, and particles. Figure 3.18 contains a legend identifying the vortices and particles in Figures 3.19 and 3.20. When released from their initial positions, the vortices eventually arrange themselves into groups approximately symmetrical about the x-axis, and thus form vortex pairs. These groups have been identified in the figures by ellipses superimposed over the identifiable groups of vortices. The pairs that these groups form have been labelled A and B.

3.5.1 Evolution of the Uniform Circulation Model

At frame 1 (Figure 3.19(a)), the vortices, shown in light grey, have just begun to move from their initial positions. The vortex sheet is still in an approximately semi-circular shape, and still contains the darker particles which are also beginning to move. The Sandia program has a clever method of telling the direction and speed of motion of the vortices and particles. They can be interpreted by the shape of the line segments which mark them. Each of these segments has a constant width (which the program aligns normal to the direction of motion), but the length (parallel to the direction of motion) is proportional to the velocity. Thus, a peak is formed by vortices at the top which have a high upward velocity. The shape of the printed vortices suggests that the motion is vertical. The fact that the motion is in the posi-

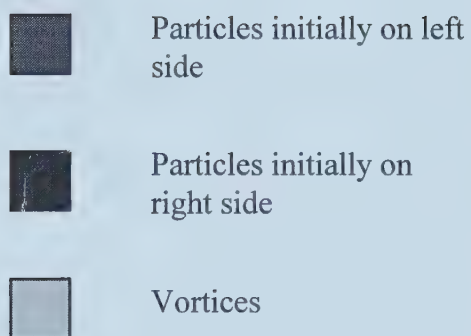
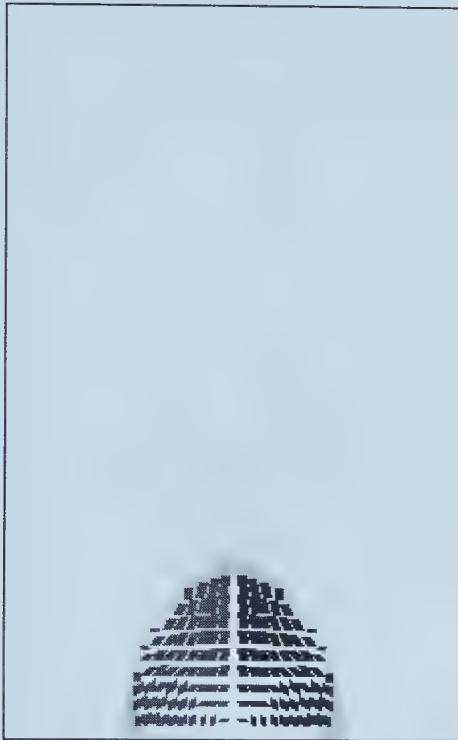
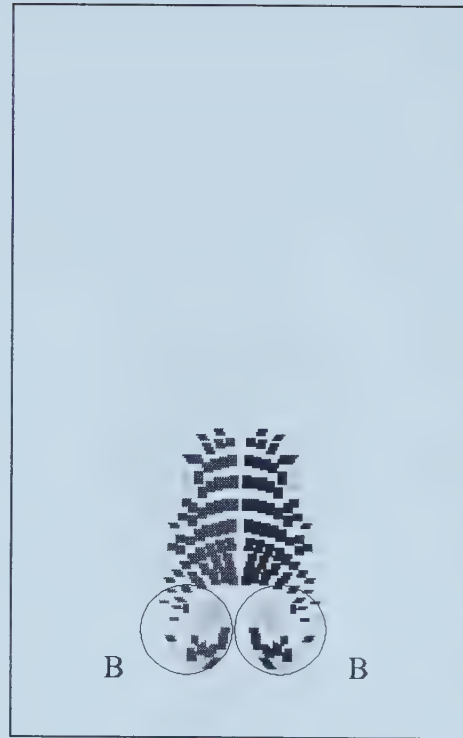


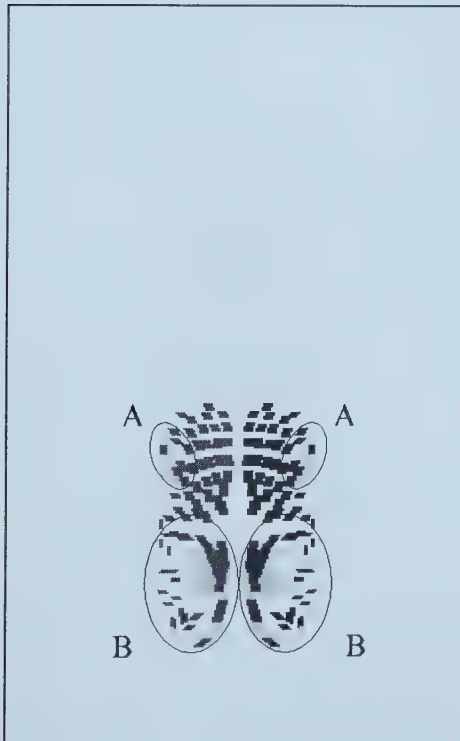
Figure 3.18: Legend for Figures 3.19 and 3.20



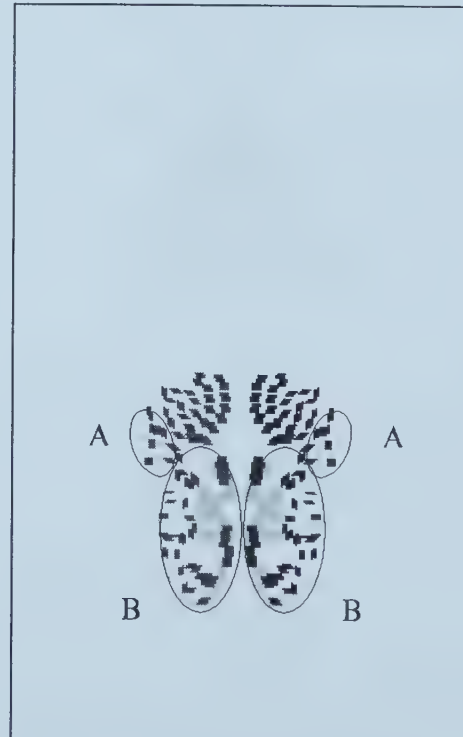
(a) frame 1, $t = 0.026s$



(b) frame 50, $t = 1.31s$



(c) frame 70, $t = 1.83s$



(d) frame 92, $t = 2.41s$

Figure 3.19: Computed Results with Point Vortices of Uniform Circulation

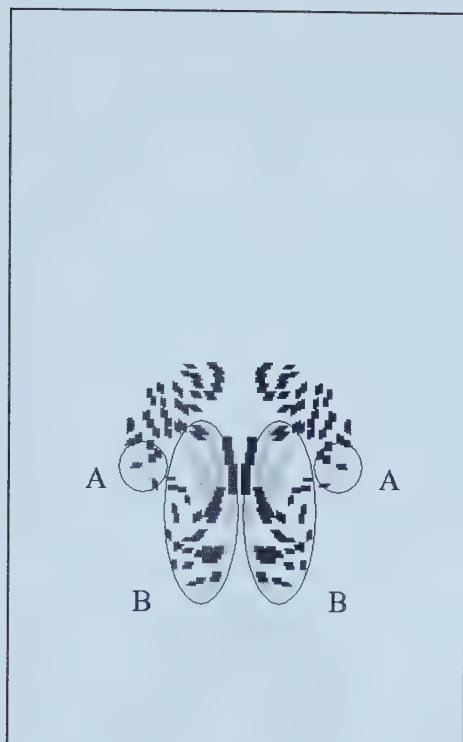
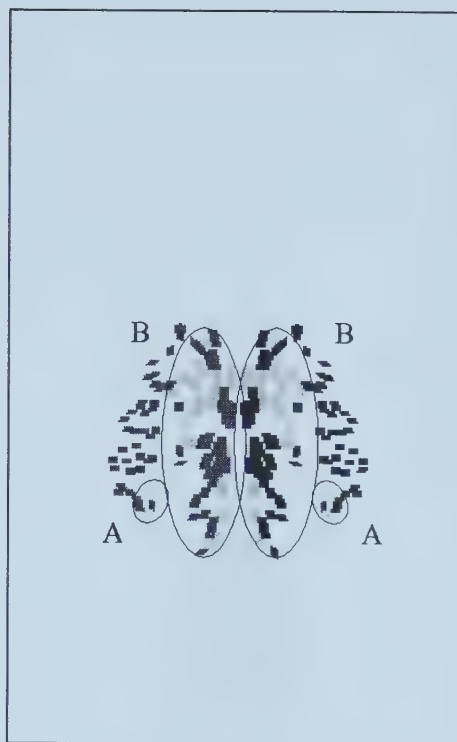
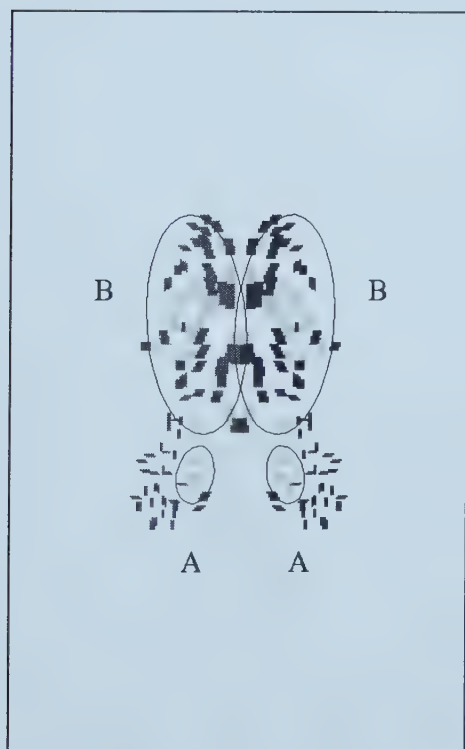
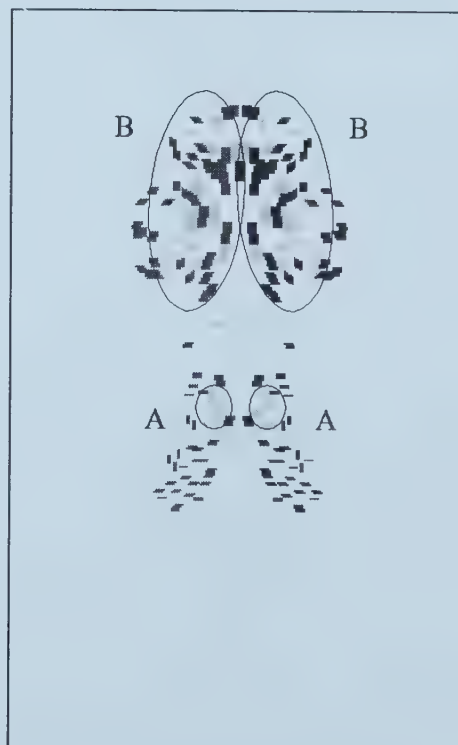
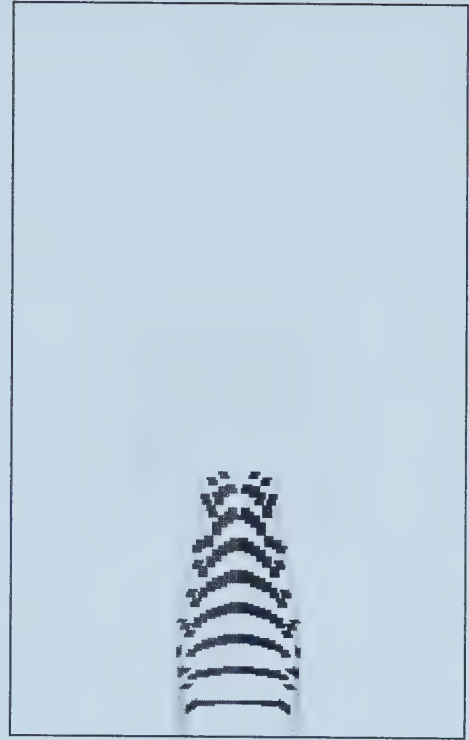
(e) frame 106, $t = 2.78s$ (f) frame 140, $t = 3.67s$ (g) frame 195, $t = 5.11s$ (h) frame 250, $t = 6.54s$

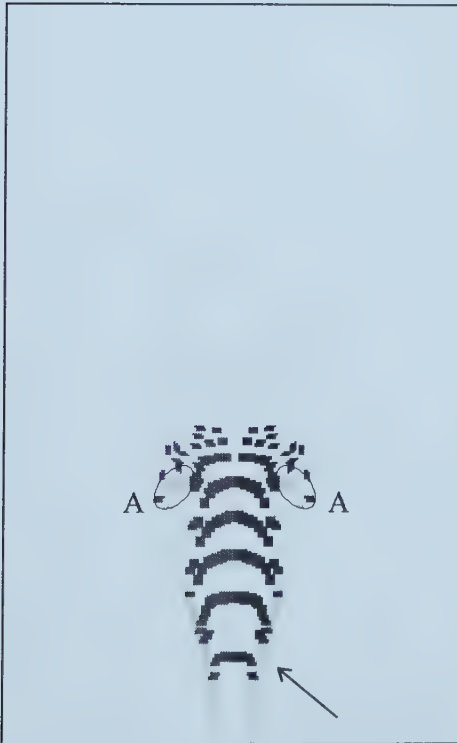
Figure 3.19: Computed Results with Point Vortices of Uniform Circulation (cont.)



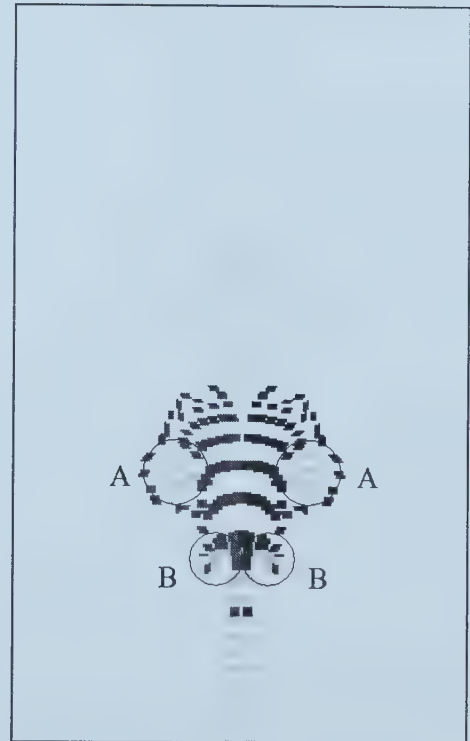
(a) frame 1, $t = 0.026s$



(b) frame 40, $t = 1.05s$

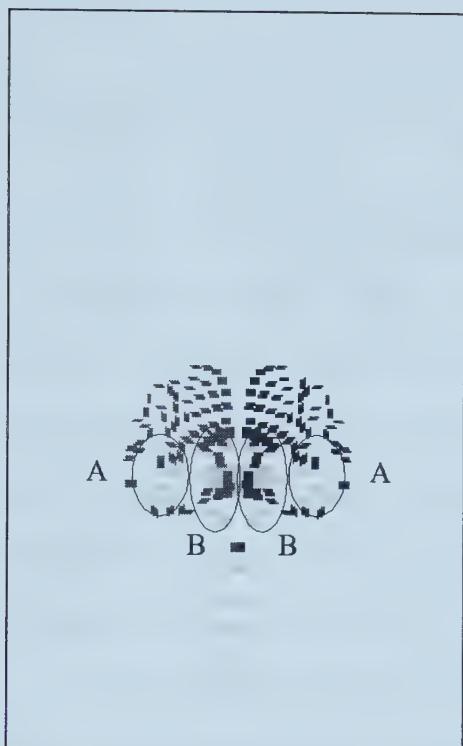


(c) frame 80, $t = 2.09s$

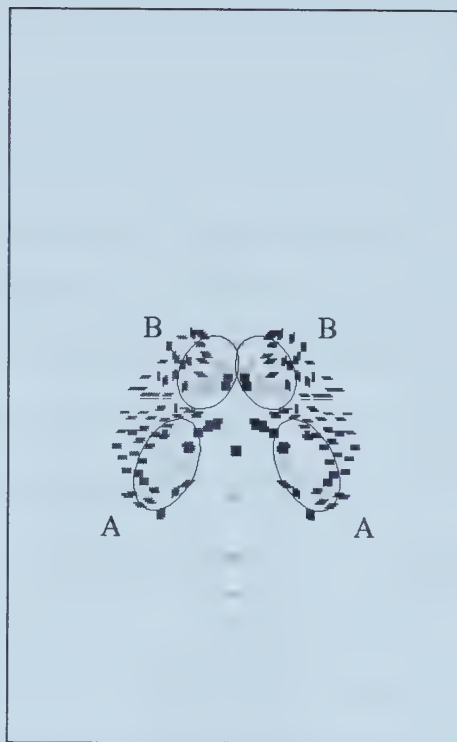


(d) frame 118, $t = 3.09s$

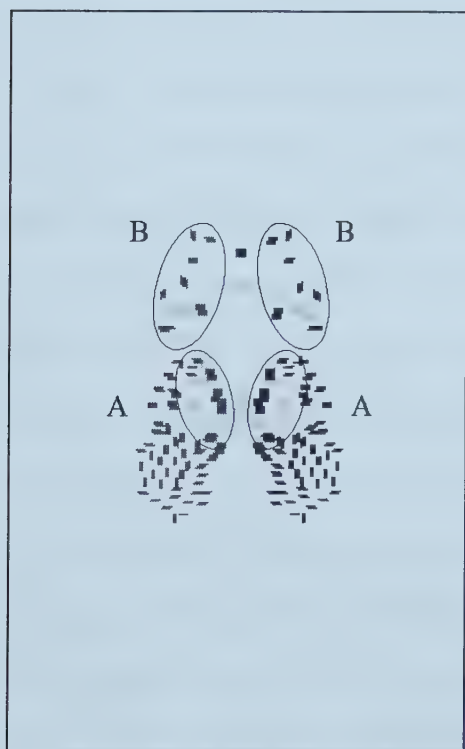
Figure 3.20: Computed Results with Point Vortices of Varying Circulation



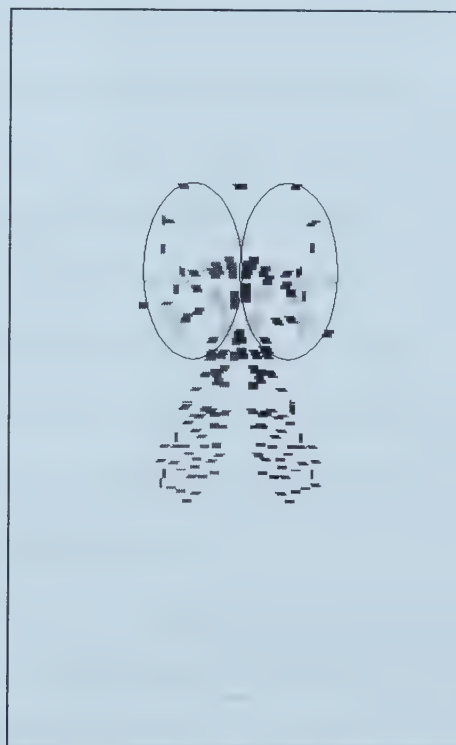
(e) frame 156, $t = 4.08\text{s}$



(f) frame 200, $t = 5.24\text{s}$



(g) frame 290, $t = 7.59\text{s}$



(h) frame 345, $t = 9.03\text{s}$

Figure 3.20: Computed Results with Point Vortices of Varing Circulation (cont.)

tive direction is determined by watching the movie on the computer screen, or considering the signs of the vortices and applying the Biot Savart Law. Likewise, the vortices and particles near the base are moving horizontally towards the centre. The two particles centred on the bottom row are very slowly moving upward (the width, as it has been defined, is now longer than the length). On this bottom row, the vertical velocities induced by the real and image vortices nearly cancel.

By frame 50 (Figure 3.19(b)), several vortices have formed a vortex pair at the base of the structure (labelled B in parallel to the labelling of the vortices in Figure 3.11), and the entire mass has begun to ascend. The rapid roll-up of the lower vortices in comparison to the top ones, is partially attributed to the inward (horizontal) component of the velocity field set up by the images, and partly due to the close proximity of vortices of opposite sign at the top, causing rapid vertical straining, thus inhibiting roll-up of these vortices. At this point, the particles and vortices at the top are also beginning to move outward, forming a cavity or void resembling that seen in the early vortex development photographs. In Section 3.3.2.1 it was surmised that this void was somehow produced by a complex distribution of vorticity existent at the top of the cloud. In the calculation, there is no such vorticity.

Figure 3.19(c) shows the model at frame 70. The upper vortices have finally rolled up into small clusters which may be identified as a vortex pair. The entire model now resembles the physical structure photographed at 15 ms, shown in Figures 3.9(d) and 3.10(c).

Vortex pairs A and B are beginning to leapfrog in frame 92, as shown in Figure 3.19(d). As in the experiment, this is resulting in shearing of the vortices of pair B.

Figure 3.19(e) is at frame 106 and depicts the vortices nearing the mid-leapfrog configuration. The outline of this figure bears a striking resemblance to the leapfrogging structure photographed in Figure 3.9(f). The significance of this resemblance will be discussed later.

In Figure 3.19(f), the model at frame 140 is shown. The vortex pairs are now late in the leapfrogging process as pair B is now leading, having almost completely passed through A. Again, the outline of the particle *cloud* is reminiscent of photographs taken at 45 ms (Figures 3.9(h) and 3.10(g)). It was at this stage in the physical experiment that the locations and shapes of the vortices could no longer be inferred directly through visualization of the structure. In this computed figure, we now see a possibility for the structure of the vortices that would form the cross-sectional shape of the clouds photographed at 45 ms.

Figures 3.19(g) and 3.19(h) show lobes being shed. In Section 3.3.2.1, the origin and content of these lobes were discussed, and the result of the discussion was inconclusive except to suggest that the lobes contained vorticity. In the current computational model, it is seen that the lobes contain vorticity, and that this vorticity is the vortex pair A.

3.5.2 Evolution of the Varying Circulation Model

At frame 1, shown in Figure 3.20(a), the vortex sheets are again forming an approximate semi-circle. As with the uniform circulation model, the top vortices are rapidly moving upward; however, the vortices near the base ($x = 0$) are exhibiting much less motion than in the previous model (compare with Figure 3.19(a)). This is due to the weaker image vortices near the base.

In frame 40, Figure 3.20(b) shows the vortex sheets to now be linear and vertical, not yet forming any discrete vortex pairs. Here the void at the top of the structure may be seen again. Again, the strength of the vortices and images near the base has not been sufficient to begin formation of a larger vortex.

By frame 80, Figure 3.20(c) shows a vortex pair beginning to roll up near the top. Approximately mid-way down the vortex sheets, is a point of inflection (indicated by the arrow) in the line that the sheet traces out. These instabilities are an indication that the once nearly linear sheets are now beginning to form a vortex pair. Also note that a wake of vorticity in the form of individual point vortex pairs is being created. The weaker lower pairs are simply not moving fast enough to keep up with the stronger pairs ahead of them.

Figure 3.20(d) shows that at frame 118, a group of vortices has combined to form the second vortex pair, B. At this point, the two pairs are beginning to leapfrog. The occurrence of leapfrogging is delayed in comparison to the uniform circulation model, and the shearing of vortex B in this case is much

less significant (compare with Figure 3.19(d)).

At frame 156, the vortex pairs are in mid-leapfrog, as shown in Figure 3.20(e). Here the relative position of A and B are similar to their positions in the uniform circulation calculation; however, here the shearing of B is not nearly as great.

By frame 200, Figure 3.20(f) shows lobes beginning to form. As before, vorticity is being shed with the particles, and again this vorticity is pair A.

At frame 290, it is seen in Figure 3.20(g) that vortex A has carried with it most of the particles into the lobes, and by frame 345, has returned to the leading pair, B, carrying with it some of the lobe particles, and leaving no vorticity in the lobes. The greater strength of vortex A has caused it to travel more quickly than B.

3.5.3 Discussion of Computed Results

As previously stated, the results of the computational models were studied in the hope of gaining additional information about what the initial vorticity conditions may be in the experiment, just after the bubble has burst, and to help understand how the lobes are generated - in particular, which vortices, if any, do they contain?

Since we are using a point vortex model to simulate a complicated three-dimensional phenomenon, caution must be exercised in applying the computed results to our understanding of the physics of the experiment. The two dimensional model is capable of representing straining in the plane of

the generated image, which we have often described as shearing; however, it cannot model the three-dimensional kinematics of tilting and stretching of vortex lines. In addition, the point vortices used in the model are an idealization, and the curvature and core geometry of the physical vortices, which were not modelled, are critical in determining the convection velocity of the vortex rings. Therefore, any quantitative results extracted from the models would not be directly applicable to the experiment, and therefore we shall only consider qualitative results. In addition, the qualitative results will only be used to suggest possibilities for the physics of the real phenomenon, and verification will be left to future experiments or better computational models.

It has been suggested in Section 3.3.2.1 that if the lobes contain vorticity, that in at least some cases, deformation of the vorticity would be primarily through tilting and stretching. This cannot be simulated by the model. It was also suggested that during leapfrogging, the primary mechanism of vorticity deformation is through shearing, which can be modelled to some extent, with the exception of the *stretching* that occurs as the vortex ring diameter is reduced. Therefore it is suggested that the model has some validity in predicting the relative locations of the vortices just prior to lobe generation. Since in both models, it is vortex A which is in the position to do so, and eventually does form the lobes, this supports the idea that A forms the lobes in the experiment. However, the complexity of the physical vortex geometries and interactions is not well known, and therefore the assumption

of limited tilting and stretching at early times may not be valid.

By comparing the shapes of the code-generated figures to the aerosol clouds photographed in Figures 3.9 and 3.10, it is possible to gain an indication of which model better represents the experiment. In other words, which set of initial conditions best represents the physical vorticity just after the bubble bursts. It was pointed out that some of the uniform circulation figures bear a striking resemblance to the cross-sectional shape of the aerosol clouds photographed, whereas the similarity was less obvious for the variable circulation model. This would suggest that the initial physical conditions may be better represented by a hemispherical vortex sheet of approximately uniform strength. The most obvious deviation between the uniform model and the photographs is the existence of large vortices formed at the base in frame 50, without any such roll-up near the top. However, with weaker image vortices, this effect would be reduced - and should be because the Teflon cylinder surface is only 25 mm in diameter, and not infinite.

3.6 Conclusions

Single and multiple exposure photographs were used to study the structure and motion of the retracting bubble film, and the ejected vortex structure from large (~ 9.5 mm radius of curvature) and small (~ 8.4 mm radius of curvature) bubbles.

A model of the vortex structure created by a bursting bubble has been proposed. The vorticity created by the bursting bubble initially organizes

itself into two vortex rings with collinear axes, and whose self-induced velocities are upward. The rings then leapfrog and form a structure consisting of a vortex ring which sheds some aerosol-marked fluid beneath it, referred to as petals or lobes. In at least some of the photographs, these trailing fluid structures visually resemble vortex hairpin loops. It is concluded that the lobes sometimes contain rotational fluid. The ring structure velocities at later times were similar for both bubbles, varying between 0.15 m/s and 0.18 m/s for time intervals between 70 ms and 130 ms. In some cases, the diameters between the vortex cores could be estimated. Between 100 and 130 ms, the diameter was found to vary between 14 and 17 mm for both bubble sizes. At 150 ms, the variation was between 16 and 18 mm for the large bubbles, and a couple of small bubbles were measured to be 16 mm. An approximate vortex ring Reynolds number during the interval of 100 ms to 130 ms is similar for both bubble sizes, and was calculated to be approximately 170.

Preliminary experiments were reported in which smoke was used as a flow visualization medium, and the results suggested that the evolution of the structure formed may be different than that formed by the current apparatus. In addition, the evolution of the structure emerging from a passively bursting bubble was studied with the present apparatus, and it was concluded that the spark used to burst the bubble in the remainder of the experiments did not significantly affect the topology of the structure.

The bursting of the bubble film creates the initial vorticity conditions for the development of the vortex structure, and therefore it too was photo-

graphically studied. The majority of the bubble film, at locations removed from the base pool, was found to be spherical in shape, and remained so during bursting. It was determined that the retraction velocity of the film rim is not constant, but exhibits a higher average velocity during the first $150\ \mu\text{s}$ than it does during the remainder of its motion. The average velocity of the large bubble rim also appears slightly greater than that of the small bubble at both the early and late times. Early time average rim velocities were measured to be $13.1\ \text{m/s}$ for the large bubbles and $10.9\ \text{m/s}$ for the small bubbles, whereas for the latter part of the retraction, these velocities were reduced to approximately $5.6\ \text{m/s}$ for the large bubbles, and $4.9\ \text{m/s}$ for the small bubbles. It is thought that this deceleration is due to the thinning of the bubble film at higher latitudes.

A two-dimensional point vortex computational model was used to simulate the event, and from its results, some suggestions were made concerning a possible origin of the lobes shed behind the vortex ring, and the initial conditions of the vorticity. In the model, it was the initially leading vortex which formed the petals. It still remains to be experimentally shown with certainty how the lobes are formed, and from where exactly in the structure this fluid comes. However, we would speculate that it is from the initially leading vortex. From observing the model's evolution with two different initial vorticity conditions, it was surmised that a first approximation of the initial conditions may be a hemispherical vortex sheet of constant strength.

In the early stages of development of the physical phenomenon, a void

of aerosol was observed at the top of the aerosol cloud. It is suggested that this was caused by the complex arrangement of vorticity at the top of the cloud, but the computed results also revealed that a similar motion of tracer particles could be achieved without such vorticity. Questions about the actual structure of the complex vorticity and the cause of the void still remain unresolved.

Bibliography

- [1] F. E. C. Culick. Comments on a ruptured soap film. *J. Appl. Phys.*, 31(6):1128–1129, 1960.
- [2] J. A. Day. Production of droplets and salt nuclei by the bursting of air-bubble films. 90:72–78, 1964.
- [3] Winnie R. McEntee and Karol J. Mysels. The bursting of soap films. 1. an experimental study. *J. Phys. Chem*, 73(9):3018–3028, September 1969.
- [4] Bill Peck and Lorenz Sigurdson. The three-dimensional vortex structure of an impacting water drop. *Phys. Fluids*, 6(2):564–576, February 1994.
- [5] Karim Shariff and Anthony Leonard. Vortex rings. *Annu. Rev. Fluid Mech.*, 24:235–279, 1992.
- [6] Lorenz Sigurdson. Atom bomb/water drop. In Gallery of Fluid Motion, Helen Reed, editor. *Phys. Fluids A*, 3:2034, September 1987.

CHAPTER 4

CONCLUSIONS AND RECOMMENDATIONS FOR FUTURE WORK

4.1 Conclusions

An apparatus has been developed which enables the study of vortex rings generated by bursting bubbles. In the development of this apparatus, several significant devices and experimental methods have been designed. A mechanism of bubble positioning and generation has been devised, in which the bubble is centred on a liquid surface placed atop a Teflon cylinder. It is based on our discovery that a bubble will centre on a convex liquid surface. A procedure was developed for measuring the gauge pressure inside the bubble, in order that the surface tension may be calculated. Finally, a system was developed to generate an aerosol flow visualization medium, and transport it into the bubble.

Single and multiple exposure photographs were used to study the struc-

ture and motion of the retracting bubble film, and the ejected vortex structure. A vortex model of the structure was suggested, and some of its dimensions and kinematic parameters were reported. At a specific point in its evolution, the vortex structure bears a striking resemblance to the vortex rings produced by water drops impacting the surface of a pool of water, and also to the mushroom cloud created by an above ground atomic bomb explosion. Properties of the bubbles, and the kinematics of the retracting film were also studied. A two-dimensional computational model was used to simulate the bubble-generated vortex structure, and was used to supplement the model derived from experimental results. A study of a passively bursting bubble suggested that the spark used to burst the remainder of the bubbles did not have a major effect on the structure of the vorticity created by the bubble. Comparison with preliminary experiments suggested that the use of smoke as a flow visualization medium may alter the evolution sequence of the vorticity.

4.2 Recommendations for Future Work

As mentioned, the smoke tracer vortex structures appear to undergo a different metamorphosis than the structures which use aerosol as a tracer. There are also some clues as to how the experimental parameters may be different between the two cases, thus causing these noted differences. For example, the smoke may act as a surfactant to the bubble film, altering rim retraction speed; and the smoke in the vortex ring may be at an elevated temperature

and therefore buoyant. Therefore, a rigorous study of smoke-filled bursting bubbles, along with further study of the aerosol-filled bubbles, may explain how the development sequences are related to experimental parameters. We now have three examples of topologically similar vortex structures created by dissimilar initial conditions - the bomb, the drop, and the bubble. The recommended study could explain how two dissimilar vortex structures may be generated from topologically similar initial conditions (smoke- and aerosol-filled bubbles) and make a contribution to the knowledge of the generation of coherent structure in turbulence.

Through the use of axial photographs of drop-generated vortex rings, Peck and Sigurdson (1) were able to partly understand the instability which resulted in petal formation, and show that the angles separating the petals were equal. For the bursting bubble-formed vortex rings, the method of petal generation is still not well understood, and their azimuthal positions are not known, since only side photographs have been taken. Therefore it is recommended that an attempt is made to obtain axial photographs of the vortex structure to address these two uncertainties.

Finally, it is recommended that a modification be made to the test chamber to improve the quality of the photographic data. At late times (> 100 ms) the aerosol becomes dilute and difficult to photograph without the use of intense lighting and high-speed film. When these are used, the background of the photograph becomes brightly illuminated as in Figures 3.9(l), 3.10(j), 3.10(k), and 3.10(l), again resulting in very poor contrast between the aerosol

and the background. It is expected that this illumination is caused by either actual illumination of the background and/or glare from the camera lens. It may therefore be beneficial to modify the back of the test chamber to reduce light reflected to the camera, and to shade the camera lens from the direct blast of the strobe so that clear late-time photos may be obtained.

Bibliography

- [1] Bill Peck and Lorenz Sigurdson. The three-dimensional vortex structure of an impacting water drop. *Phys. Fluids*, 6(2):564–576, February 1994.

APPENDIX A

DR. ASHURST'S CODE

The computational models were derived from a FORTRAN code written by Dr. W.T. Ashurst of Sandia National Laboratories in Livermore, California. In its original state, the code modelled a transversely-forced two-dimensional jet. An additional piece of software was used to create a movie from the computed results.

The vortex core model supplied with the original code was used in the current models. Also, the numerical scheme for vortex advancement was unchanged, and the solution for each time step was recorded in ascii files using the subroutine provided. Dr. Ashurst's code modelled particles in the flow as having inertia and subject to aerodynamic drag. In the present code, the particles are without inertia, and are simply convected at the local velocity induced by the vortices. This is the manner in which the vortices are convected in the original and modified models. The vortex dynamics of Dr. Ashurst's code are described in (1).

Section A.2 describes the vortex core model and shows how the Biot Savart Law is applied to calculate the velocity field induced by the vortices. The numerical scheme used to advance vortices and particles in space, is discussed in Section A.3.

A.1 The Initial Geometric Conditions

The initial geometries of the vortex models are given in Section 3.4.

A.2 Vortex Core Model and Induced Velocity

The vortices are modelled as point vortices with a modification made to disallow infinite velocity at the location of the vortex. In the general case, the velocity induced at any point, by a distribution of vorticity, is given by the Biot Savart Law:

$$\mathbf{U}_v(\mathbf{x}) = -\frac{1}{4\Pi} \int_V \frac{(\mathbf{x} - \mathbf{x}') \times \omega(\mathbf{x}')}{|\mathbf{x} - \mathbf{x}'|^3} dV(\mathbf{x}'), \quad (\text{A.1})$$

where \mathbf{U}_v is the induced velocity vector at position \mathbf{x} , V is the volume over which the integral is evaluated, \mathbf{x}' is a dummy variable of integration, which represents a position in V . Finally, $\omega(\mathbf{x}')$ is the vorticity vector at the location \mathbf{x}' . For a two-dimensional point vortex, Equation A.1 is reduced to:

$$U_v = \frac{\Gamma}{2\Pi r}. \quad (\text{A.2})$$

Here, Γ is the circulation of the point vortex, and r is the radial distance from the vortex. U_v is now a scalar, reporting the velocity magnitude. The streamlines created by an isolated point vortex are concentric circles with the vortex at their centres. The vortex is defined as of positive sign if the flow is counter-clockwise, and negative if clockwise.

In the current model, Equation A.2 is modified as follows:

$$U_v = \frac{\Gamma}{2\pi r'} \quad (\text{A.3})$$

where $r' = \sqrt{r^2 + \sigma^2}$, and $\sigma = 1.5\delta$ (δ is given in Equation 3.4). Therefore there can never be a singularity in this equation. In the current models, the velocities are calculated at the locations of each vortex and particle by summing the contributions of all (other) vortices according to Equation A.3.

A.3 The Numerical Scheme

The instantaneous velocities of the vortices and particles are given explicitly by Equation A.3, and therefore do not need to be determined numerically. However, these velocities must be numerically integrated using a finite difference scheme to determine the vortex and particle locations at subsequent time steps.

The new location vector, \mathbf{x}_{i+1} , of the vortices is calculated using the equation:

$$\mathbf{x}_{i+1} = \mathbf{x}_i + \frac{dt}{2}(3\mathbf{u}_i - \mathbf{u}_{i-1}) \quad (\text{A.4})$$

where the subscript i specifies the current time step, the magnitude of the vector \mathbf{u} is given in Equation A.3 (U_v), and time step dt is given in Equation 3.5. For the particles, the new position is given by

$$\mathbf{x}_{i+1} = \mathbf{x}_i + dt\mathbf{u}_i. \quad (\text{A.5})$$

At each time step, the displacements of the particles and vortices are calculated by summing the vortex-induced velocities at the location of each particle or vortex, using Equation A.3, then determining the new location according to Equation A.4 or A.5.

Bibliography

- [1] W. T. Ashurst and Eckart Meiburg. Three-dimensional shear layers via vortex dynamics. *J. Fluid Mech.*, 189:87–116, 1988.

APPENDIX B

CANADIAN CONGRESS OF APPLIED MECHANICS

Lorenz W. Sigurdson, James H. Buchholz, and Bill J. Peck. “The vortex rings created by bursting air bubbles and impacting water drops”. In *Canadian Congress of Applied Mechanics*, pp. 542-543, 1995.

The Vortex Rings Created by Bursting Air Bubbles and Impacting Water Drops

L.W. Sigurdson, J.H. Buchholz, B.J. Peck

Department of Mechanical Engineering, University of Alberta, Edmonton, AB, T6G 2G8

1. INTRODUCTION

An air bubble will rise in a liquid and will burst as it penetrates the free surface. This is geometrically the "flip" experiment of the water drop falling through air and impacting a similar free surface, which we know can form a complex vortex ring structure^[1]. It follows that a similar vortex ring may appear in the air when the air bubble bursts, and this is in fact so. Whatever models are suggested for vorticity generation at an air-water interface must account for this observation. In this situation the acting pressure gradients at the interface would be expected to be in a similar direction to the water drop case although the gradient of the density is acting in an opposite one. The bursting bubble experiment is therefore a natural extension of the previous experiment and is expected will provide important clues to the vorticity generation mechanism in both.

The first mention of vortex rings resulting from breaking bubbles was by Rogers in 1858^[2]. He found that piercing a spherical smoke-filled bubble with a slender wire produced a "beautifully distinct ring." In 1917 Swinton and Beale^[3] discovered that smoke rings could be formed by creating a spark beneath the surface of some resin oil. More recent researchers have been interested because the bursting-bubbles play an important role in the production of sea-salt nuclei at the sea surface (Kientzler et al., 1954^[4], Day 1964^[5]). Although Rogers had a sketch, and Day photographed some of the water droplets being carried upward by the ring, *no one in the published literature has ever photographed the structure of the vortex ring.*

Our objective was to obtain, for the first time, detailed photographic data of the vortex ring generated in the air by the bursting bubble. We decided to use a stationary bubble resting on an air-water interface for ease of reproducibility. Although this is a simpler case than that of a rising bubble penetrating the interface and bursting, it will allow us to observe the relevant vorticity production processes, the subsequent evolution of the vortical structure, and the velocity of the primary vortex ring.

The anticipated significance is multi-levelled. The vortex ring that occurs during bubble bursting is important to the modelling of heat and mass transfer which occurs in many industrial processes, for example, boiling and transport

of contaminants during distillation. The resulting drops convecting through the air can trap air on impact with the liquid. Oceanographers and meteorologists are interested because of the salt particles that are injected into the atmosphere, which even appear at cloud levels. The deeper levels of significance and longer term objective is to gain better understanding of vorticity generation and learn more about three-dimensional vortex structures and turbulence by comparing this case to the impacting drop and others.

2. EXPERIMENT

The methodology involved is very similar to the impacting drop work^[1] but required some new apparatus design. There are five components to success: producing a bubble in a repeatable way, positioning the bubble such that a camera can be focused on it, breaking the bubble on command, selecting the media for flow-visualization and selecting the best sequence of exposures to record the data on still or movie film.

A break-through was made concerning the positioning of the bubble. We discovered that a bubble would always migrate to the center of a thin pool of liquid resting on top of a small flat-topped Teflon cylinder. The thin pool would have a slightly curved meniscus and surface tension effects would draw the bubble to its peak, the center of the vertically aligned cylinder. This is very important to this experiment as it allows prelocation of whatever device is used to break the bubble film. Bubble breakage has been successfully done using two electrodes on either side of the film so that a spark can be created between them. This allows us to initiate the bursting process at will and subsequently trigger a strobe to take photographs at single times after a certain delay, or at any number of preset times to produce a multiple exposure. The electronics and photographic equipment to perform this are similar to those used for the impacting drop work^[1].

The current medium for visualization of the air currents associated with the vortex ring is smoke placed within the bubble. This has been sufficient to help in preliminary design of the experiment, but other techniques will be investigated for future experiments. Concern over the effects of the smoke on the surface tension of the bubble film and buoyancy of the air will be evaluated.

Sequences of photographs were taken during the film retraction phase to see how the spark-induced hole grows outward until the bubble film is pulled into the fluid. At the same time we were able to observe where the vorticity first appears to aid in understanding its generation mechanism. Preliminary photographs (a sample shown in Figure 1) show that the initial roll-up of the vorticity into a vortex ring involves many smaller discrete vortex rings, indicative of the Kelvin-Helmholtz instability of a free shear layer. Another sequence of photos shows how the vorticity forms the often three-dimensional vortex ring structure (an example shown in Figure 2). A line vortex model was developed as was done for the water drop^[1]. The velocity of the vortex ring was measured from the multiply-strobed photographs.

3. CONCLUSION

The first known photographs of the structure of the vortex ring created when a bubble bursts have been taken. The ring has some structure similar to that created by an impacting water drop.

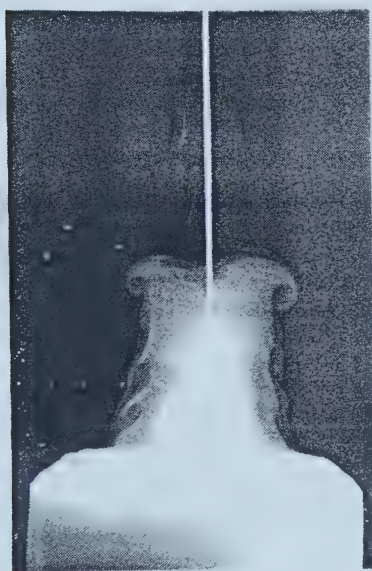


Figure 1. Early stages of vortex ring development (vertical white line is spark electrode, base cylinder diameter = 2.54 cm).

4. REFERENCES

- [1] Peck, B.J. & Sigurdson, L.W. "The Three-Dimensional Structure of an Impacting Water Drop", *Physics of Fluids*, 6(2), pt. 1, 564-576 (1994).
- [2] Rogers, W.B., "On the Formulation of Rotating Rings by Air and Liquids under Certain Conditions of Discharge", *Am. J. of Sci.*, 26, pp. 246-258, (1858).
- [3] Swinton, A.A.C. & Beale, E., "The Bursting of Bubbles", *Nature*, 98, p. 469, (1917).
- [4] Kientzler, C.F., Arons, A.B., Blanchard, D.C. & Woodcock, A.H., "Photographic Investigation of the Projection of Droplets by Bubbles Bursting at a Water Surface", *Tellus*, 6, No. 1, pp. 1-7, (1954).
- [5] Day, J.A., "Production of Droplets and Salt Nuclei by the Bursting of Air-Bubble Films", *Qtlly. J. Roy. Met. Soc.*, 90, pp. 72-78, (1964).

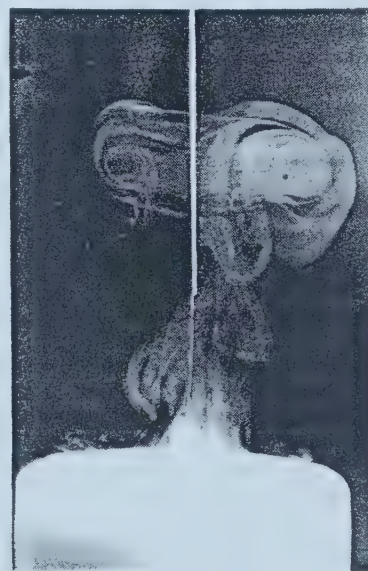


Figure 2. Fully developed vortex ring structure.

APPENDIX C

INTERNATIONAL SYMPOSIUM ON FLOW VISUALIZATION

James Buchholz, Lorenz Sigurdson, and Bill Peck. An apparatus to study vortex rings emerging from bursting bubbles. In J. Crowder, editor, *Proceedings of the Seventh International Symposium on Flow Visualization*, pages 146-151, New York, 1995, Begell House Inc.

An Apparatus to Study Vortex Rings Emerging from Bursting Bubbles

J.H.J. Buchholz, L.W. Sigurdson, B.J. Peck

Department of Mechanical Engineering, University of Alberta

1. INTRODUCTION

Previous experiments have been reported involving the production of vortex rings, below an air/water interface, by a falling water drop penetrating a free water surface^[1]. Likewise, it has been discovered that there is an inverse experiment yielding comparable results; an air bubble rising in water will penetrate the surface, burst, and eject a gaseous vortex ring into the air. It is this phenomenon that is currently of interest. However, because of complexities caused by the random path of a rising bubble, a somewhat modified experiment has been undertaken. This experiment involves the study of a gaseous vortex ring emerging from a stationary bubble, floating on a liquid surface. The apparatus and procedures used in the conduct of this experiment, and some preliminary photographic results, are discussed in the following sections.

The existence of vortex rings emerging from bursting bubbles has been acknowledged by several researchers since Rogers first published hand sketches of the vortex rings in 1858^[2]. In 1917, Campbell Swinton and Beale witnessed vortex rings emerging from bursting bubbles which were produced by a spark generated within a container of resin oil^[3]. Since then, such vortex rings have not been actively studied, but have been observed by researchers concerned with the production of jets and drops by bursting bubbles (Stuhlman, 1932^[4], Day, 1964^[5], and MacIntyre, 1972^[6]). Despite the past research on bursting bubbles, *the structure of the vortex ring emerging from a bursting bubble has apparently never been photographically studied in the published literature.*

The significance of studying these vortex rings may be perceived on three levels. The most immediate benefit is an increased understanding of the flow patterns and mechanisms of mass transfer present during bubble bursting. For example, bursting bubbles are the predominant source of particulate transfer from sea to air^[6]. On a broader perspective, it is expected that this study will produce insight on the means of vorticity generation at an air water interface. Ultimately, the investigation of the simple vortex structure emerging from a bursting bubble will aid in understanding large scale turbulent systems in general.

2. EXPERIMENTAL APPARATUS

In order to obtain the necessary photographs, four steps are required. First, a bubble must be produced. Second, the bubble is positioned in the focus of a stationary 35mm camera. Third, the bubble is broken, and finally, a series of exposures are recorded. Currently, two types of exposures have been obtained; single exposures of the vortex structure at a prescribed time after bursting, and multiple exposures of the vortex ring which have been used to determine its

approximate translational velocity. The bubble was often photographed prior to bursting in order to accurately record its size.

A syringe is used to form a bubble on the surface of a pool of soap solution. This solution is held by surface tension to the top face of a vertical Teflon cylinder, 25.4mm in diameter. Two electrodes are vertically positioned; one above and one below the bubble film to produce a spark across the film, and thus initiate bursting. To minimize distortion of the vortex ring by motion of the ambient air, a plywood box was built to enclose the experiment.

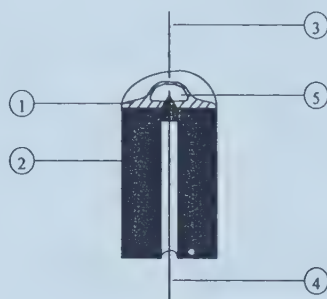


Figure 1. Apparatus for producing and bursting bubbles. (1) bubble solution, (2) Teflon cylinder, (3) & (4) electrodes, (5) bubble.

Figure 1 contains a cutaway diagram of the Teflon cylinder and attached components. The electrodes are made from 25 gauge hypodermic tubing with 30 gauge constantan thermocouple wire pressed into the end of each tube to form a sharp tip. The top electrode is painted black to minimize reflected light. Bubble solution was made from 75mL distilled water, 25mL glycerin, and 6 drops Sunlight™ hand dishwashing detergent, or equivalent proportions. The ratio of glycerin to water was derived from a "recipe" given by Boys^[7]. Cigarette smoke was used as a flow visualization medium inside the bubble.

Photographs were taken with a Nikon 35mm camera using 400ASA Kodak Ektachrome film, and were illuminated with a General Radio Type 1540 Strobolume. A 55mm Micro Nikkor lens was mounted on a bellows extension in order to obtain the required magnification. The experiment was performed with the room lights turned off, and the camera shutter held open. At predetermined times after the spark, the strobe was illuminated and still images were recorded on film. Figure 2 shows the positioning of the camera, strobe, and related apparatus relative to the Teflon cylinder.

Figure 3 is a schematic diagram of the electronics necessary for bursting the bubble, and for timing and producing strobe flashes. The active components are the spark generator, delay generator, burst timer, function generator, and strobe. The bubble is burst by the spark generator, which sends a signal to the delay generator. The delay generator then produces an adjustable time delay before sending an output signal to the burst timer. The burst timer is simply a gate

which allows a signal to be transmitted for a preset amount of time. The function generator used is a Dynascan 3030 Sweep/Function Generator. Its purpose is to produce a square wave signal at a programmed frequency which triggers the strobe once per cycle during the time in which the burst timer is active. In addition, a Hewlett Packard 5314A Universal Counter is used to accurately determine the delay produced by the delay generator, the frequency of the function generator, and the active time of the burst timer.

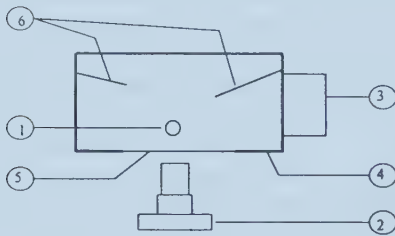


Figure 2. Plan view of apparatus. (1) Teflon cylinder, (2) camera, (3) strobe, (4) enclosure, (5) window, (6) light deflectors.

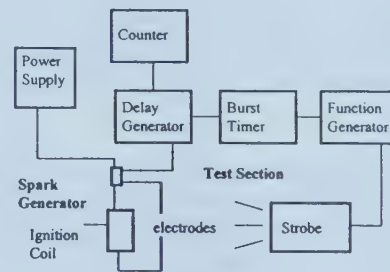


Figure 3. Spark generator and timing electronics. Note: the counter may be connected to the delay generator (shown), the burst timer, or the function generator.

3. RESULTS AND DISCUSSION

Currently the most significant result has been the development of the apparatus and procedures necessary to produce quality photographic data. In addition, preliminary quantitative measurements have been made of the sizes, velocities, and Reynolds numbers of emerging vortex rings.

A) Functioning of the Apparatus

Perhaps the most important discovery made, relating to experimental method, is the method with which the bubble is positioned on the liquid surface. The solution described in the previous section was applied to the top of the Teflon cylinder, using an eyedropper, such that a slightly convex meniscus was formed. When a bubble was formed on this surface, it was found to consistently migrate to the center of the surface.

In addition to positioning the bubble, producing a bubble presented a significant challenge. Initially, a stationary vertical orifice was positioned just below the liquid surface ($\sim 1\text{mm}$). However, the orifice appeared to draw in liquid, and thus often produced a foam instead of the desired single bubble. This is possibly the result of surfactants deposited by the smoke, into the orifice and/or solution. An orifice was then mounted on a movable arm, above the liquid surface in an effort to enable purging of the entrained liquid prior to producing a bubble. Unfortunately this yielded similar results, and the current method of producing bubbles

using a syringe was developed. The syringe contains a hypodermic tip approximately 20cm long which is inserted through a hole in the experimental enclosure, and submerged into the bubble solution. Some skill is then required to form a single bubble on the liquid surface without producing additional bubbles or foam.

B) Other Design Considerations

These efforts applied to designing apparatus and conducting experiments have been primarily aimed at determining the viability and potential of studying this phenomenon. In the future, increased control of the experiment will be required in order to obtain accurate and consistent quantitative results from the photographic data.

One area of investigation is the composition and use of electrodes to initiate bubble bursting. McEntee and Mysels^[8] have suggested that the composition of the electrodes affect the characteristics of a bursting film. They proposed that initiation of the hole in the film can be unsymmetrical due to "sputtering of the metal or oxide" from the electrodes. Gold was recommended as it minimized these effects. In addition, they suggested that the spark may cause transverse waves propagating through the film. Therefore, in the present case we have considered an alternate method of triggering the strobe, which was used by Mysels and Stikeleather^[9]. This involves a laser beam reflected from the surface of the film into a photodiode. Upon passive bursting, the laser beam would be broken, and timing may be initiated.

The use of smoke as a flow visualization medium will most likely be undesirable in future experiments. Because the smoke is at an elevated temperature with respect to the ambient air, buoyant effects may influence the development and propagation of the vortex ring. Furthermore, deposits from the smoke presumably act as surfactants, further decreasing control in the experiment. At this point, an alternate medium has not been selected, although fluorescein mist has been considered.

C) Preliminary Analysis of the Photographic Data

Figures 4 and 5 are double exposure photographs. The former is a vortex ring 26.5ms after the spark occurs, and the bubble it originated from. The latter are two exposures of the same vortex ring at 30ms and 60ms after the spark. Using the cylinder diameter (25.4mm) as a scale, and the time difference between the two exposures of Figure 5, the calculated average translational velocity of the vortex cores (V_{ring}) is approximately 0.35m/s. The Reynolds number (Re) is approximately 230, where

$$Re = \frac{V_{ring} D_{ring}}{\nu}$$

In this equation, D_{ring} = distance between the vortex cores = 10mm, and ν = kinematic viscosity.

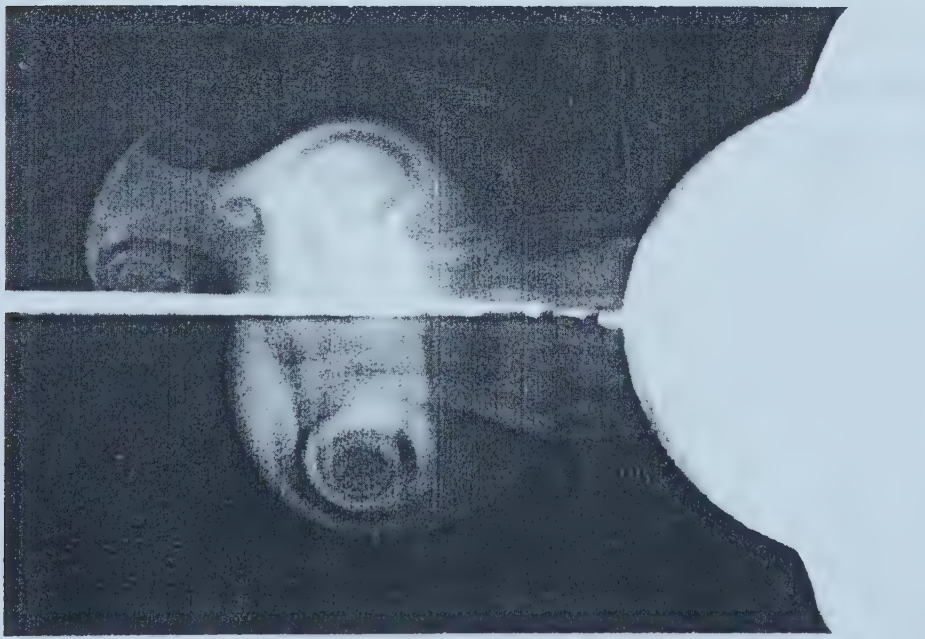


Figure 4. Vortex ring 26.5ms after spark discharge, and the bubble from which it originated.

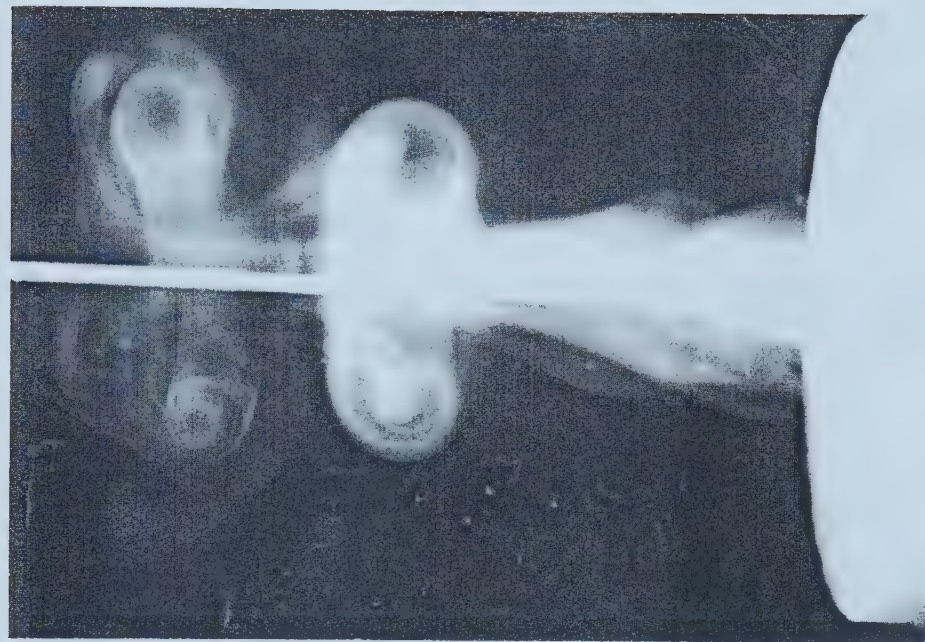


Figure 5. Double exposure of a vortex ring at 30ms and 60ms after spark discharge.

4. CONCLUSIONS

An experimental procedure and apparatus have been developed to enable the photographic study of vortex rings emerging from bursting bubbles. Two highlights of this development are the method by which the bubble was positioned -- using a Teflon cylinder -- and the technique of producing a bubble using a syringe. Approximate calculated values of bubble velocity and Reynolds number have been obtained from preliminary photographic data. Other design considerations were discussed for future modification of the apparatus.

5. ACKNOWLEDGMENTS

The authors thank Mr. B. Faulkner for his help with construction of the apparatus. The first author is also appreciative of the Faculty of Engineering of the University of Alberta for support through a Dean's Research Award. This work was supported by the Natural Sciences and Engineering Research Council of Canada, Grant No. OGP0041747.

- ¹ Peck, B.J. & Sigurdson, L.W. "The three-dimensional vortex structure of an impacting water drop," *Physics of Fluids*, **6**(2), pt. 1, pp. 564-576, (1994).
- ² Rogers, W.B., "On the formation of rotating rings by air and Liquids under certain conditions of discharge," *Am. J. of Sci.*, **26**, pp. 246-258, (1858).
- ³ Campbell Swinton, A.A. & Beale, E., "The bursting of bubbles," *Nature*, **98**, p. 469, (1917).
- ⁴ Stuhlman, Jr., O., "The mechanics of effervescence," *Physics (J. Appl. Physics)*, **2**(6), pp. 457-466, (1932).
- ⁵ Day, J.A., "Production of droplets and salt nuclei by the bursting of air-bubble films," *Quart. J. Roy. Meteorol. Soc.*, **90**, pp. 72-78, (1964).
- ⁶ MacIntyre, F., "Flow patterns in breaking bubbles," *J. Geophys. Res.*, **77**(27), pp. 5211-5228, (1972).
- ⁷ Boys, C.V., *Soap Bubbles*, 1890. Reprinted by Doubleday & Company Inc., 1959, and by Dover Publishing Co., New York, 1959.
- ⁸ McEntee, W.R. & Mysels, K.J., "The bursting of soap films, I, an experimental study," *J. Phys. Chem.*, **73**(9), pp. 3018-3028, (1969).
- ⁹ Mysels, K.J. & Stikeleather, J.A., "The bursting of soap films, 3, spontaneous and induced bursting," *J. Colloid Interface Sci.*, **35**(1), pp. 159-162, (1971).

APPENDIX D

DIVISION OF FLUID DYNAMICS MEETING OF THE AMERICAN PHYSICAL SOCIETY (1995)

L.W. Sigurdson and J.H.J Buchholz, The vortex structure of impacting water drops and bursting air bubbles, Bull. Am. Phys. Soc., 40(12), p.1920, 1995.

Abstract Submitted
for the DFD95 Meeting of
The American Physical Society

The Vortex Structure of Impacting Water Drops and Bursting Air Bubbles LORENZ W. SIGURDSON, JAMES H.J. BUCHHOLZ, Dept. of Mechanical Engineering, University of Alberta, Edmonton, AB, Canada — A water drop resting on a surface of a pool of water (a boule) and then breaking through is topologically and kinematically similar to the bursting of an air bubble resting on the surface of a pool of water. It follows that a vortex ring occurs in the latter case as is known to occur in the former. Photographs have proven this (Buchholz, Sigurdson and Peck, Phys. Fluids Vol. 7 No. 9, Sept 1995). Experiments using flow visualization have been done in both cases, although the drops initially have non-zero momentum. The drop's primary vortex ring (Peck and Sigurdson, Phys. Fluids Vol. 6 No. 2, Pt. 1, Feb 1994) appears to contain mainly vorticity of sign consistent with a vortex ring travelling downward. The bursting air bubble primary ring similarly has vorticity of sign consistent with a vortex ring travelling upward. It is *different* from the drop vortex ring in that the primary ring also often displays significant amounts of vorticity of opposite sign to this. The wakes of the rings can contain hairpin loops. The bubble vorticity initially undergoes a Kelvin-Helmholtz type instability before rolling up to form the primary ring, and sometimes a smaller ring appears ahead of the primary ring.

This work was supported by NSERC Grant No. OGP004174.

APPENDIX E

PHYSICS OF FLUIDS: GALLERY OF FLUID MOTION

James Buchholz, Lorenz Sigurdson, and Bill Peck. Bursting soap bubble. In Helen Reed, editor, *Gallery of Fluid Motion*, *Phys. Fluids*, 7(9):s3, September 1995.



FIG. 1.

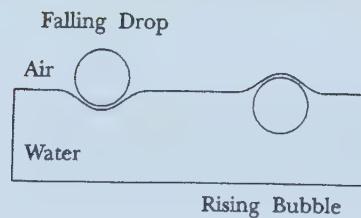


FIG. 2.

BURSTING SOAP BUBBLE

Submitted by James Buchholz, Lorenz Sigurdson, and Bill Peck
(University of Alberta)

This vortex ring was generated by a smoke filled bursting soap bubble resting on a free surface. This is similar to the simpler case of a rising bubble penetrating a free surface, the "flip" experiment of a falling water drop impacting a free surface [Peck and Sigurdson, *Phys. Fluids A* 3, 2032 (1991)]. Comparing these two rings may help understand the vorticity generation mechanism at an air-water interface. This is a triple exposure, first by the spark used to break the bubble, once by a strobe very shortly after the bubble has been pierced by the spark, and once at a later time showing the resulting vortex ring (base width of bubble=1.54 cm).

The authors thank Mr. Bernie Faulkner for this technical assistance and the Natural Sciences and Engineering Research Council of Canada for their support (Grant No. OGP41747).

University of Alberta Library



0 1620 0781 5812

B45241